Doklady Physics, Vol. 50, No. 1, 2005, pp. 1–2. Translated from Doklady Akademii Nauk, Vol. 400, No. 1, 2005, pp. 35–36.

PHYSICS

On Interactions of Quasiparticles in Photosensitive Crystals

B. U. Barshchevskiĭ and R. V. Ryabova

Presented by Academician S.T. Belyaev June 30, 2004

Received June 30, 2004

In photosensitive crystals, quasiparticles, i.e., excitons and phonons, are excited states of a solid, and their existence in vacuum seems to be impossible.

Quasiparticles are produced as a result of photochemical reactions, thermal deformations, and interactions of electrons and holes with defect lattice sites at the crystal surface. Furthermore, in halide crystals an exciton can annihilate with a subsequent transformation into a halogen ion. Thus, an exciton is an elementary electrical excitation in semiconductors and dielectrics that can propagate over the crystal. It is produced as a result of the appearance of an electron–hole pair moving across the crystal. The exciton energy is lower than that of the forbidden-zone width. Interactions of an exciton and a phonon result in a variation of the energy (frequency) of the photon being formed. This variation is equal to the difference (or the sum) of the energies of the exciton and the phonon, which is observed in luminescence or absorption spectra of crystals under study. In the luminescence spectra of silver halides, phonon repetitions of certain lines were observed. For example, in AgBr, phonons are produced [1] with a frequency

$$\nu_0 = \left(\frac{\varepsilon_0}{\varepsilon_\infty}\right)^{1/2}\nu_e,$$

where ε_0 is the static dielectric constant of the crystal, ε_∞ is the dynamic permittivity of the crystal in the luminescence observation region, $\nu_e = \dfrac{h}{\mu\beta^2}$ ($\mu = 260$ cm^{-1}, μ is the exciton reduced mass, β is the distance between the components in an electron–hole pair, and the energy is $0.323\ \vartheta\beta$, see [1]).

The following lines (whose frequencies are expressed in cm^{-1}) exhibit phonon repetitions, which were observed experimentally [2]: 21404 – 21142 = 262; 20513 – 20251 = 260; 20773 – 20513 = 260; and 20062 – 19802 = 260.

Optical phonons are produced in a crystal elementary cell in the course of motion of opposite-sign ions excited by the alternating electric field of a light wave. It is remarkable that, for different lines, the energy of phonons being formed are only slightly distinguished from each other.

If the excitation energy exceeds the forbidden-zone width, then it is assumed that the electron and hole diverge in the crystal lattice for a distance at which their interaction is absent.

In AgCl crystals, phonon repetitions of spectral lines, which differed by phonon frequency, were also observed [3]:

$$\nu_0 = \left(\frac{\varepsilon_0}{\varepsilon_\infty}\right)^{1/2}\nu_e = \left(\frac{12.3}{5.1}\right)^{1/2}\nu_e = 232\ \text{cm}^{-1}.$$

At a temperature of $T = 4.2$ K, the probability that quasiparticle annihilations accompanied by an energy transfer in the form of luminescence will occur is higher than at higher temperatures. Therefore, after subtracting the phonon energy, some of the spectral lines are repeated, which can be seen from the experimental results of [2, 3] (line frequencies are expressed in units of cm^{-1}):

24131 – 23901 = 230;
24067 – 23832 = 235;
23832 – 23364 = 2 × 234;
23832 – 23602 = 230;
23753 – 23529 = 224;
22810 – 22341 = 2 × 234;
22331 – 22099 = 232;
22222 – 21988 = 234.

These data also do not exclude a possibility of obtaining other results [4, 5] in the case of a variation of the experimental conditions. For example, a small number of the lines observed in certain series of the experiments can be explained by the relatively weak intensity of these lines, which prevents their observation. We may assume that the variation of experimental conditions also will make it possible to distinguish other lines with their phonon repetitions in addition to those given above.

Special attention should be given to the fact that the ratio of phonon frequencies in AgBr and AgCl is 260/232 = 1.12, which almost coincides with the ratio

Russian Research Centre Kurchatov Institute, pl. Kurchatova 1, Moscow, 123182 Russia

1028-3358/05/5001-0001$26.00

of the forbidden-zone energy widths for the above-indicated crystals, as well as with the ratios of their high-frequency permittivities squared, Rydberg constants for excitons, and other physical parameters of alkali–halide crystals of the KBr and KCl types [6].

It is natural to assume that the ratio of 1.12 obtained for the indicated quantities can also be observed in halides of other metals, e.g., in crystals of the $PbBr_2$ and $PbCl_2$ types. We can also assume that this ratio for the frequencies of optical phonons for AgBr and AgCl is a consequence of the same ratio for the following quantities [6]:

$$\frac{E_{g_2}}{E_{g_1}} = \frac{R_2^1}{R_1^1} = \frac{\varepsilon_1^2}{\varepsilon_2^2} = \frac{\nu_{01}}{\nu_{02}} = \frac{(r_{me}^+ + r_{\mathrm{Br}}^-)^2}{(r_{me}^+ + r_{\mathrm{Cl}^-})^2} = 1.1,$$

where $\nu_{1,2}$ are phonon frequencies in AgBr and AgCl. We did not take into account here the presence of phonons corresponding to elastic oscillations in the crystal lattice for which the frequency is lower than that of optical phonons. The optical-phonon frequency is almost two orders of magnitude lower than that of photons producing the exciton absorption lines or crystal luminescence lines.

As a result of the interaction of excitons and phonons, the frequency of exciton emission lines can increase or decrease by the value of the phonon frequency both one time of many times. The phonon frequency is determined by the same features of the emission and absorption of light in crystals, i.e., by oscillations of lattice ions, which depend on the temperature and size of ions forming the crystal lattice [6].

REFERENCES

1. R. Knox, *Theory of Excitons* (New York, 1963; Mir, Moscow, 1966).
2. E. B. Kozyreva and P. V. Meĭklyar, Opt. Spektrosk. **23**, 427 (1967).
3. B. U. Barshchevskiĭ, V. N. Batog, and G. M. Safronov, Dokl. Akad. Nauk SSSR **208**, 627 (1973) [Sov. Phys. Dokl. **18**, 406 (1973)].
4. R. V. Ryabova, B. U. Barshchevskiĭ, A. A. Kondrashova, *et al.*, Dokl. Akad. Nauk SSSR **315**, 409 (1990).
5. B. U. Barshchevskiĭ and R. V. Ryabova, Zh. Nauchn. Prikl. Fotogr. Kinematogr. **45**, 44 (1998).
6. B. U. Barshchevskiĭ, Usp. Fiz. Nauk **171**, 415 (2001) [Phys. Usp. **44**, 397 (2001)].

Translated by G. Merzon

Doklady Physics, Vol. 50, No. 1, 2005, pp. 12–17. Translated from Doklady Akademii Nauk, Vol. 400, No. 2, 2005, pp. 186–191.

PHYSICS

Femtosecond Dynamics of Excitations and Electron–Electron Interactions in Single-Wall Carbon Nanotubes

V. A. Nadtochenko*, A. S. Lobach, F. E. Gostev, O. M. Sarkisov, D. O. Shcherbinin, S. A. Kovalenko, and N. P. Érnsting

Presented by Academician S.M. Aldoshin July 21, 2004

Received July 21, 2004

INTRODUCTION

Presently, there are reliable theoretical and experimental proofs in favor of the fact that unusual electron and electron-transport properties of single-wall carbon nanotubes (SWNT) are associated with the effects of electron–electron interactions in these one-dimensional quantum systems [1, 2]. Femtosecond spectroscopy is a unique and efficient method for the study of the electron dynamics and electron–electron interactions in nanosize systems. This method makes it possible to thoroughly analyze the evolution of elementary excitations (excitons, electron–hole (*e–h*) pairs, plasmons, etc. [3]). Recently, publications have appeared [4–9] in which femtosecond-spectroscopy methods were employed in studies of excitation dynamics in SWNT. In these studies, for probing excited SWNT, spectrally narrow probe pulses were used. On the other hand, the investigation of the dynamics of excited states in a wide spectral range allows us to simultaneously obtain experimental data on different excited states, which yields more detailed information on electron–electron interactions and nonlinear optical properties of SWNT. In the present study, the femtosecond dynamics of SWNT is investigated in water-micellar suspensions. A distinctive feature of our experiments compared to previous ones [4–9] is the use of probe pulses of the broadband femtosecond white continuum as well as the excitation of a sample by light pulses containing photons of completely different energies of 2, 2.5, and 4 eV.

EXPERIMENTAL PROCEDURE

SWNT manufactured by Carbon Nanotechnologies, Inc. were used, which had been obtained by the method of carbon oxide catalytic decomposition on iron at a high pressure of 30–50 atm and at a temperature of 900–1100°C. The suspension of SWNT in a 1-wt % water-micellar solution of sodium dodecylsulfate was prepared by the following method. A nanotube sample (2.5 mg) was poured over by 20 ml of a 1-wt % water-micellar solution of sodium dodecylsulfate and then dispergated by ultrasound at a UZDN-1 setup (35 kHz, 500 W) for a time of 2 h. Further, the solution was centrifuged for 5 h at an acceleration of 8000*g*, and the centrifugate was decanted. The sediment was filtered through a 2-μm track membrane and weighted. The nanotube concentration in the centrifugate, which was determined by the weight difference of initial nanotubes and the sediment, was 22 μg/ml at pH = 6.

We used two femtosecond laser devices, namely:

(1) a ring dye laser with mode synchronization and the wavelength λ = 616 nm. The pulse duration and the energy upon amplification were 50 fs and 1 mJ, respectively. A white-supercontinuum pulse (λ = 390–1000 nm) was obtained by the nonlinear optical transformation of a femtosecond pulse (λ = 616 nm) in water (this part of the work was fulfilled at the Institute of Chemical Physics, Russian Academy of Sciences, Moscow);

(2) a Clark MX 100 femtosecond laser with a subsequent nonlinear optical transformation of light into a 50-fs pulse with a wavelength of 485 nm in a CaF_2 crystal (Humboldt University, Berlin).

Plane-polarized pulses were aligned with a magic angle. The experiments were performed in a 1-mm and 0.5-mm flow-type cell at room temperature in aerobic conditions. Spectra were registered with the help of two diode assemblies after the spectral decomposition of a white-continuum pulse in the optical spectrometer was performed. Details concerning the experimental setup and the method of processing the data obtained were presented elsewhere [10].

RESULTS AND THEIR DISCUSSION

Figure 1 presents differential spectra $\Delta D(\varepsilon, t)$ after the excitation of SWNT by femtosecond pulses. The

Institute of Problems in Chemical Physics, Russian Academy of Sciences, Chernogolovka, Moscow oblast, 142432 Russia

** e-mail: van53@rambler.ru; nadto@icp.ac.ru*

1028-3358/05/5001-0012$26.00

differential spectra are the difference between the absorption spectra $D^*(\varepsilon, t)$ and $D(\varepsilon)$ of an excited and unexcited sample, respectively, i.e., $\Delta D(\varepsilon, t) = D^*(\varepsilon, t) - D(\varepsilon)$. In the $\Delta D(\varepsilon, t)$ spectra presented in Fig. 1, bleaching peaks corresponding to $\Delta D(\varepsilon, t) < 0$ are found when the SWNT excitation has a lesser absorption compared to an unexcited nanotube, as well as absorption peaks when $\Delta D(\varepsilon, t) > 0$. In addition, at short delay times, a broad bleaching band was discovered in the form of a pedestal for peaks in the $\Delta D(\varepsilon, t)$ spectrum. For short delay times, the bleaching dominates in the $\Delta D(\varepsilon, t)$ spectrum.

The SWNT absorption spectra in different spectral regions were thoroughly investigated previously in a number of studies (see, e.g., [11, 12]). It was assumed in these studies that separate peaks in the $D(\varepsilon)$ nanotube absorption spectra in water-micellar suspensions could be attributed to transitions in individual nanotubes with a certain diameter and a chiral angle (angle of twisting the graphen plane into a tube). Based on the data of [11, 12], we can assume that, in a sample under investigation, peaks in the absorption spectrum (Fig. 2) in the photon-energy region higher than 2 eV correspond to metallic tubes, whereas absorption peaks within the range of 1.45–2.1 eV correspond to transitions of the E_{22} type for tubes with semiconductor properties, and absorption peaks in the region lower than 1.45 eV correspond to transitions of the E_{11} type for semiconductor nanotubes [6]. Furthermore, in the SWNT absorption spectrum, a broad plasma peak with a maximum at about 4.8 eV is observed. Nanotubes of different chirality and of various diameters also are present in the sample under investigation, and, as follows from Raman-scattering data, the values of the diameters lie within the range 0.7–1.1 nm. In analogy with conclusions of [11, 12], we can assume that the bleaching peaks observed in the $\Delta D(\varepsilon, t)$ spectrum correspond to individual nanotubes. The peaks observed in the $D(\varepsilon)$ absorption spectrum and in the $\Delta D(\varepsilon, t)$ differential spectra are associated with the Van Hove singularity for the single-electron state density of SWNT [1].

The important result obtained in our experiments using broadband-light probe pulses was the discovery of spectral shifts and broadening of the excited spectrum of SWNT compared to unexcited ones (Fig. 2). We now discuss the reasons for peak shifts in the $\Delta D(\varepsilon, t)$ spectra with respect to the $D(\varepsilon)$ spectra.

The spectrum of excited SWNT is determined by two components, namely, by optical transitions of quasiparticles, i.e., excitons, electron–hole pairs, and plasmons, as well as by optical transitions of the residual unexcited electron system that can be considered as a Fermi liquid. The formation of a substantial concentration of nonequilibrium excited states (quasiparticles) in SWNT, which occurs under the action of femtosecond pulses, can result in a noticeable perturbation of the electron Fermi liquid by virtue of correlation effects of the electron–electron interaction. This perturbation manifests itself as a shift or broadening of bands of the absorption spectrum $D^*(\varepsilon, t)$ [3]. As a result, peaks must be observed in the differential spectrum $\Delta D(\varepsilon, t) = D^*(\varepsilon, t) - D(\varepsilon)$. The contribution of the absorption of quasiparticles into the $\Delta D(\varepsilon, t)$ spectra will be analyzed by us in future publications.

Figure 2 clarifies the problem concerning shifts and broadening of the $D(\varepsilon)$ spectrum after exciting a sample at time delays shorter than 1 ps. For the photon-energy region lower than 1.8 eV (the region of semiconductor SWNT), bleaching peaks in the $\Delta D(\varepsilon, t)$ spectrum are shifted by 26–46 meV towards the higher energy region with respect to peaks in the $D(\varepsilon)$ spectrum. In this case, the shape of the absorption spectrum of an unexcited sample in the form of the second derivative $\frac{d^2D(\varepsilon)}{d\varepsilon^2}$ in the region lower than 1.8 eV qualitatively repeats the shape of the differential spectra $\Delta D(\varepsilon, t)$ at time delays shorter than 1 ps. However, the $\Delta D(\varepsilon, t)$ spectra are shifted towards the high-energy region with respect to $\frac{d^2D(\varepsilon)}{d\varepsilon^2}$. At short delay times, in the region higher than 2 eV (the region of metallic SWNT), the differential spectrum $\Delta D(\varepsilon, t)$ repeats with a rather high accuracy the shape of the $\frac{d^2D(\varepsilon)}{d\varepsilon^2}$ spectrum. For the interval higher than 2 eV, the shift of the bleaching peaks in the $\Delta D(\varepsilon, t)$ spectrum with respect to the peaks in the $D(\varepsilon)$ absorption spectra is insignificant. The similarity of the shapes for the $\Delta D(\varepsilon, t)$ spectrum and for that of an unexcited sample in the form of $\frac{d^2D(\varepsilon)}{d\varepsilon^2}$ indicates the broadening of the absorption peaks in the excited-sample spectrum $D^*(\varepsilon, t)$. If the Gauss absorption band is broadened under the conservation of the transition oscillator strength, then the differential spectrum $\Delta D(\varepsilon, t)$ is equal (with an accuracy to a numerical factor) to the second derivative of the absorption band [13]. An analogous effect of similarity for the shapes of both the second derivative of the absorption spectrum and the differential spectrum was observed previously in C_{60} films [13]. For C_{60}, the cause of the broadening was considered to be the appearance of random local electric fields $\Delta\mathbf{E}_i$ in the case of optical excitation of charge carriers. The experimental results concerning photoelectron emission [14] also testify to the broadening of Van Hove peaks. In our study, this effect is revealed by the absorption femtosecond-spectroscopy method. An additional qualitative proof of the appearance of peaks in the $\Delta D(\varepsilon, t)$ spectrum due to shifts and broadening is the fact that their positions slightly depend on the excitation-photon energy when it varies from 2 to 4 eV. The initial energy and momentum distributions of quasiparticles significantly depends on the excitation-photon

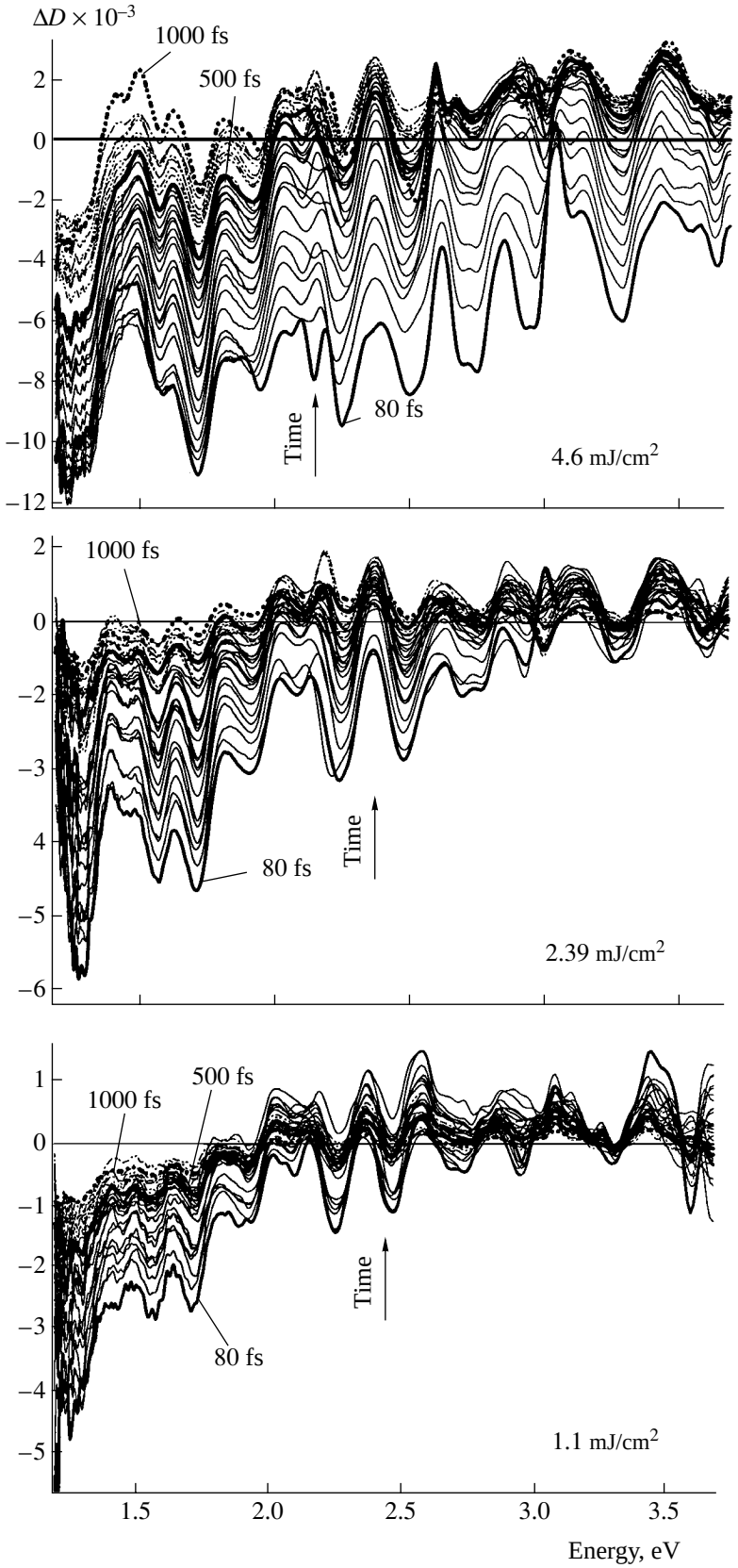

Fig. 1. Differential spectra of single-wall carbon nanotubes after excitation by a 2.5-eV photon pulse. The spectra shown correspond to the time windows of 80–500 and 500–1000 fs with the intervals of 20 and 50 fs, respectively. In the figure, the excitation-energy density is also indicated.

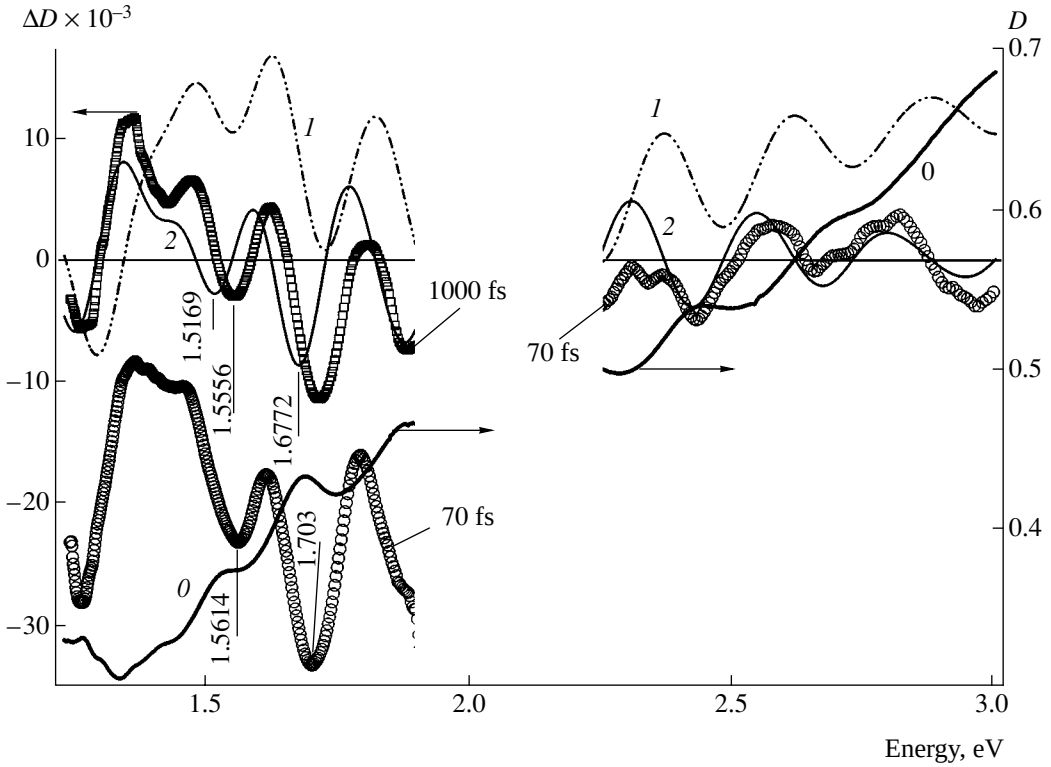

Fig. 2. Comparison of differential absorption spectra $\Delta D(\varepsilon, t)$ for different delay times of probe pulses with the absorption spectrum $D(\varepsilon)$ (line 0) and absorption spectrum in the form of the first derivative $\frac{dD(\varepsilon)}{d\varepsilon}$ (line *1*) and the second derivative $\frac{d^2D(\varepsilon)}{d\varepsilon^2}$ (line *2*). The energy of an exciting photon is 4 eV.

energy. Therefore, we can expect differences in the spectra of optical transitions of quasiparticles. However, a weak dependence of the differential spectrum $\Delta D(\varepsilon, t)$ on the initial distribution of quasiparticles is revealed. This implies that the number of excitations rather than their distribution plays the more essential role. This conclusion is consistent with the above suggestion concerning the predominate contribution of optical transitions of Fermi-liquid electrons perturbed by electron–electron interactions.

The excitation of SWNT by photons of energies 2, 2.5, and 4 eV occurs far from the interzone-transition edge. This results in the creation of primary quasiparticles such as electron–hole pairs with a nonzero kinetic energy. The electrons and holes pass through several relaxation stages as a result of scattering due to the Coulomb interaction with each other and scattering by phonons. The electron–electron scattering and electron–hole scattering result in the establishment of a quasi-equilibrium over states inside zones and is considered as an intra-zone relaxation. The relaxation between the zones is associated with electron–phonon interactions. The time scale of electron–phonon scattering usually lies in the picosecond region [15]. In our experiments, we observed relaxation processes on a time scale considerably shorter than 1 ps and on the scale of tens of picoseconds. Here, we analyze only the rapid component of the bleaching relaxation kinetics on a time scale down to 1 ps. Figure 3 illustrates this kinetics for different wavelengths of a probe pulse. The bleaching relaxation curve $\Delta D(\varepsilon, t)$ is approximated by an exponential law $y_0 + A\exp\left(-\frac{t}{\tau}\right)$. A dependence of the relaxation-rate constants $\frac{1}{\tau(\varepsilon)}$ on the probe-pulse light energy ε is observed (Fig. 4). A broadband probe pulse has allowed us to find that the dependence $\frac{1}{\tau(\varepsilon)}$ exhibits peaks against the background of the monotonic rise of the relaxation constant $\frac{1}{\tau(\varepsilon)}$ with an increase in the probe-pulse photon energy. The position of the peaks in the dependence $\frac{1}{\tau(\varepsilon)}$ repeats that of the peaks in the $\Delta D(\varepsilon, t)$ spectrum (Fig. 4). Peaks in the bleaching spectrum $\Delta D(\varepsilon, t)$ are close to the absorption at subzone edges and are associated with Van Hove singularities in the SWNT state density. Thus, the minima in the depen-

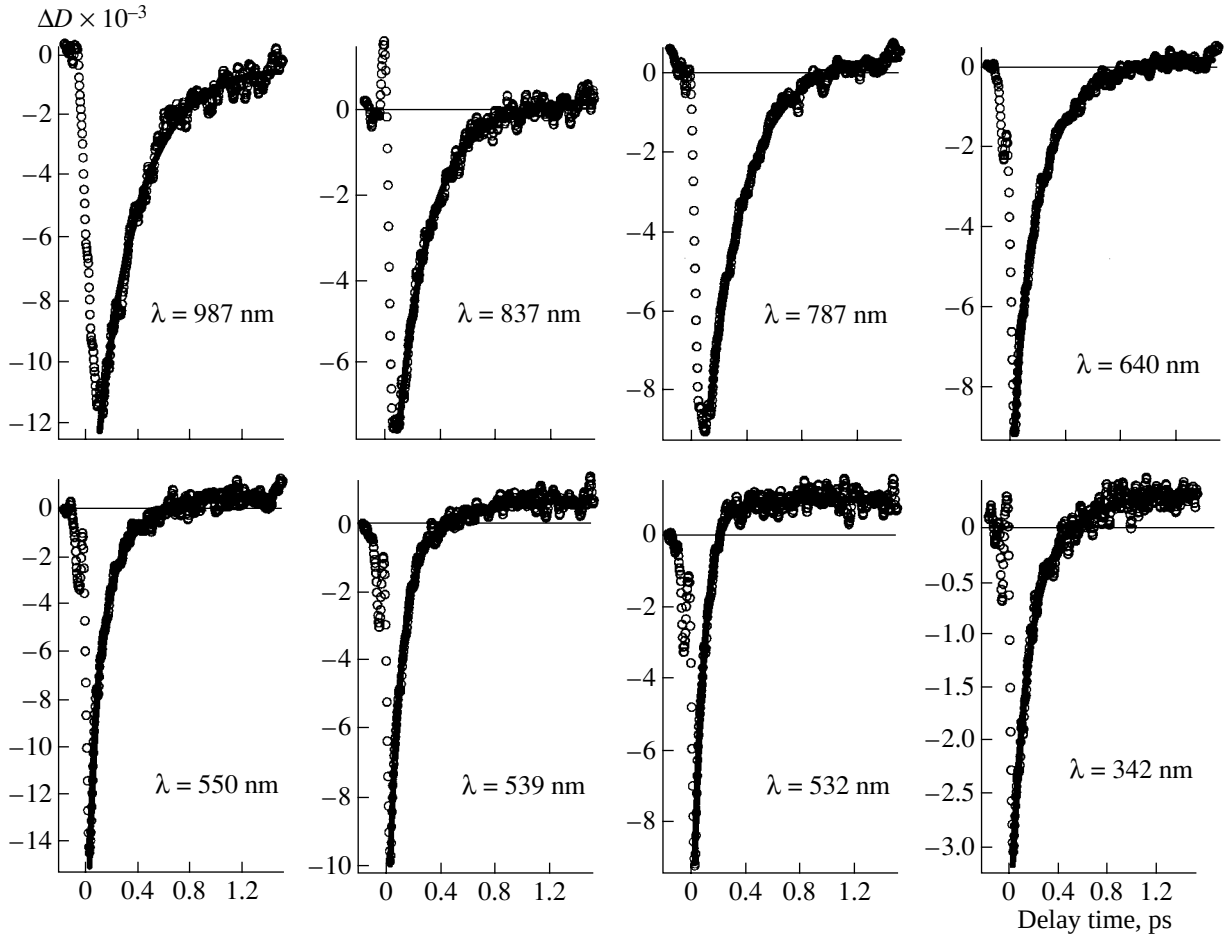

Fig. 3. Relaxation kinetics for different wavelengths of a probe light pulse.

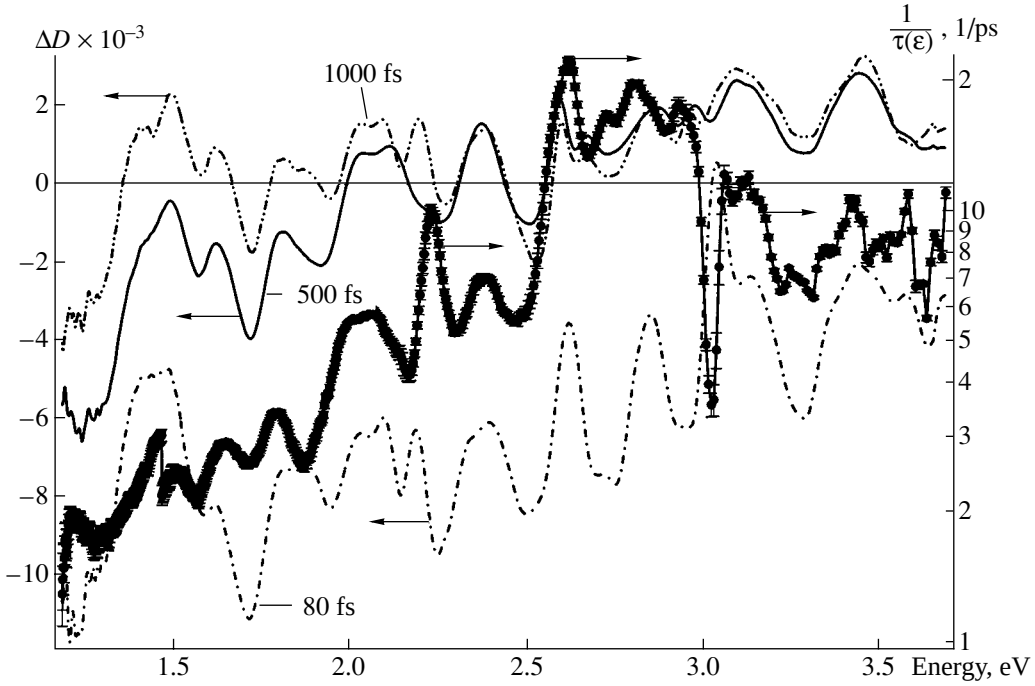

Fig. 4. Differential absorption spectra $\Delta D(\varepsilon, t)$ and constants of the bleaching relaxation rate $\frac{1}{\tau(\varepsilon)}$. The excitation energy density is 4.6 mJ/cm^2. The exciting photon energy is 2.5 eV.

dence $\frac{1}{\tau(\varepsilon)}$ correspond to subzone edges. The dependence $\frac{1}{\tau(\varepsilon)}$ should be associated with two effects, namely, a trivial nonuniform broadening due to the existence of various SWNT in a sample (different nanotubes are characterized by different constants) and a nontrivial behavior of cross sections of electron–electron and electron–hole scattering processes as a function of the energy and angular momentum **k** [1, 3]. In the scattering processes, electron–hole pairs must be generated that take the energy and angular momentum of relaxing charge carriers. The probability of this process depends not only on the final state of relaxing carriers but also on the number of possible electron–hole pairs capable of accommodating the corresponding energy and angular-momentum variations (Pauli principle). Previously, only photoemission-spectroscopy experiments served as experimental evidence of the dispersion effect for the relaxation constants of charge carriers in SWNT [1, 14]. The observed dependence $\frac{1}{\tau(\varepsilon)}$ shown in Fig. 4 now demonstrates the manifestation of this effect in the femtosecond absorption-spectroscopy experiments. In these experiments, peaks in the $\frac{1}{\tau(\varepsilon)}$ dependence are expressed much more clearly than in photoemission-spectroscopy experiments.

ACKNOWLEDGMENTS

The authors are grateful to A.V. Bazhenov, V.D. Kulakovskiĭ, and Yu.E. Lozovik for very fruitful discussions of the results of the study.

The work was supported by the Russian Foundation for Basic Research, project nos. 02-03-32428, 03-03-32727, 03-03-32668; by the Program "Fundamental Problems of Physics and Chemistry of Nanometric-Scale Systems and Materials" of the Presidium of the Russian Academy of Sciences, project nos. RAN 1/OKh-04, RAN 2/P-04; as well as by the mutual agreement between Russia and Germany on scientific cooperation between the Institute of Chemical Physics, Russian Academy of Sciences (Moscow) and Humboldt University (Berlin).

REFERENCES

1. T. Hertel, R. Fasel, and G. Moos, Appl. Phys. A: Mater. Sci. Process. **75**, 449 (2002).
2. C. L. Kane and E. J. Mele, Phys. Rev. Lett. **90**, 207401 (2003).
3. I. E. Perakis and T. V. Shahbazyan, Surface Sci. Repts. **40**, 1 (2000).
4. J.-S. Lauret, C. Voisin, G. Cassabois, *et al.*, Phys. Rev. Lett. **90**, 057404 (2003).
5. O. J. Korovyanko, C.-X. Sheng, Z. V. Vardeny, *et al.*, Phys. Rev. Lett. **92**, 17403 (2004).
6. Y.-Z. Ma, J. Stenger, J. Zimmerman, *et al.*, J. Chem. Phys. **120**, 3368 (2004).
7. J. Kono, G. N. Ostojic, S. Zaric, *et al.*, Appl. Phys. A: Mater. Sci. Process. **78**, 1093 (2004).
8. G. N. Ostojic, S. Zaric, J. Kono, *et al.*, Phys. Rev. Lett. **92**, 117402 (2004).
9. H. Hippler, A.-N. Unterreiner, J.-P. Yang, *et al.*, Phys. Chem. Chem. Phys. **6**, 2387 (2004).
10. E. N. Ushakov, V. A. Nadtochenko, V. A. Gromov, *et al.*, Chem. Phys. **298**, 251 (2004).
11. S. M. Bachilo, M. S. Strano, C. Kittrell, *et al.*, Science **298**, 2361 (2002).
12. M. J. O' Connell, S. M. Bachilo, C. B. Huffman, *et al.*, Science **297**, 593 (2002).
13. V. M. Farztdinov, A. I. Dobryakov, V. S. Letokhov, *et al.*, Phys. Rev. B **56**, 4176 (1997).
14. T. Hertel and G. Moos, Chem. Phys. Lett. **320**, 359 (2000).
15. T. Hertel and G. Moos, Phys. Rev. Lett. **84**, 5002 (2000).

Translated by G. Merzon

Doklady Physics, Vol. 50, No. 1, 2005, pp. 18–24. Translated from Doklady Akademii Nauk, Vol. 400, No. 3, 2005, pp. 323–329.

PHYSICS

Consideration of Pair Correlations in the Probabilities of Multiparticle Figures

A. I. Gusev and A. A. Rempel'

Presented by Academician G.P. Shveĭkin July 20, 2004

Received August 2, 2004

Simultaneous inclusion of the long- and short-range orders in ordering systems is an unsolved problem of the statistical theory of atomic ordering. There are two groups of methods for solving the ordering problem. Cluster methods include the most-developed cluster-variation method [1], where interactions between particles within a cluster, i.e., the short-range order, and multiparticle correlations are exactly taken into account, but the interaction of the cluster with the environment is disregarded. For this reason, the cluster-variation method is poorly applicable to systems where the long-range order is formed stepwise as the first-kind transition. The other group of methods belongs to the mean-field approximation, among which the method of static concentration waves [2] is the most developed and applicable to the structural order–disorder phase transitions in systems with substitution. However, the theoretical determination of equilibrium superstructures by this method has not yet been realized for real systems. To describe the structural order–disorder phase transitions in systems with atomic substitution, the order parameter functional method is sufficiently efficient [3–5]. This method exactly takes into account the lattice symmetry and interaction between particles within a cluster. The ordered phases arising due to ordering in strongly nonstoichiometric compounds $MX_y\square_{1-y}$ (M is Ti, Zr, Hf, V, or Nb, Ta; X is C or N; and $\square$ is a vacancy) and A_yB_{1-y} solid solutions were theoretically determined for the first time using the order parameter functional method [4–6]. However, near the order–disorder transition temperature T_{trans}, the ordered-phase boundaries on the calculated phase diagrams are shifted toward the AB (or $MX_{0.5}\square_{0.5}$) compound, which contradicts the experimental data. This demerit is attributed to the fact that the available variant of the order parameter functional method takes into account only the long-range order and the corresponding correlations. However, in ordered phases, in addition to long-range correlations, there are short-range correlations, which do not disappear at the order–disorder transition temperature but remain in the disordered phase, gradually decreasing with an increase in temperature.

Thus, the problem of the simultaneous inclusion of the short- and long-range orders in the thermodynamic potential of an ordering system has not yet been solved. The first step in the solution is the representation of the probabilities of multiparticle figures in terms of correlations or the short-range order parameters. However, even this partial problem has not yet been solved in the general form. At present, such problems are solved primarily by computer simulation, i.e., in numerical form (see, e.g., [7]).

For the analytical inclusion of correlations in the probabilities of multiparticle figures, conditional probability was used [8, 9]. In the simplest variant of this approach, the probabilities of two-particle figures are treated as known values specified with the inclusion of pair correlations. If the probability of occupying an arbitrarily chosen initial site is equal to the statistical value, the probability of occupying the neighboring site by an atom of a certain type can be found using the known probability of the two-particle figure. Sequentially continuing this procedure along the chain of sites forming the multiparticle figure, the conditional probabilities of occupying all sites can be determined and the probability of the multiparticle figure can be found using the pair correlation. However, the change of independent single-particle probabilities to conditional probabilities is incorrect, because indefiniteness arises in the choice of the initial site of the figure, the probability, corresponding to this site, and movement direction on the figure sites.

To analytically calculate the probabilities of multiparticle figures, Sidorenko *et al.* [10, 11] proposed using correlation moments (correlations) ε. In the general case, the probability $P_i^{(s)}$ of the ith configuration of the cluster figure s including $R^{(s)}$ lattice sites occupied by $R^{(s)} - p$ atoms A and p atoms B in the two-component

Institute of Solid State Chemistry, Ural Division, Russian Academy of Sciences, ul. Pervomaĭskaya 91, Yekaterinburg, 620219 Russia

e-mail: gusev@ihim.uran.ru, rempel@ihim.uran.ru

1028-3358/05/5001-0018$26.00

crystal A_yB_{1-y} can be calculated by averaging over the entire crystal

$$P_i^{(s)} = \left\langle \prod_{j=1}^{R^{(s)}} \sigma_j(\beta) \right\rangle, \quad (1)$$

where $\sigma_j(\beta) = 1$ or 0 is the occupation number of the jth site by an atom of type β. Each configuration of the figure s can have one or several equivalent configurations; i.e., it has multiplicity $\lambda_i^{(s)}$. The multiplicity $\lambda_i^{(s)}$ equal to the index of the point symmetry group $G_i^{(s)}$ of the figure s with the ith configuration with respect to the point group $G_0^{(s)}$ of the figure s, all sites of which are occupied by atoms of one type; i.e., $\lambda_i^{(s)} = \dfrac{n(G_0^{(s)})}{n(G_i^{(s)})}$, where $n(G)$ is the order of the group G [12]. According to [13, 14], the correlation moment ε_s of the order s is calculated as

$$\varepsilon_s = \left\langle \prod_{j=1}^{R^{(s)}} [\sigma_j(\beta) - \langle \sigma_j(\beta) \rangle] \right\rangle. \quad (2)$$

In view of Eq. (2), the probability $P_i^{(s)}$ for the solid solution A_yB_{1-y} is represented as [10, 11]

$$P_i^{(s)} = \langle \sigma_j(A) \rangle^{R^{(s)}-p} \langle \sigma_j(B) \rangle^p + \sum_{q=2-r}^{q=n-r} \langle \sigma_j(A) \rangle^{R^{(s)}-p-q} \langle \sigma_j(B) \rangle^{p-r} \sum_{n \in s} a_{q,r}^{(n)} \varepsilon_{n,q,r}. \quad (3)$$

Here, $a_{q,r}^{(n)}$ is the number of equivalent nth subfigures in the figure s, which has the ith configuration; the nth subfigure contains n sites and q sites are occupied by atoms A and r sites are occupied by atoms B ($q + r = n$); p is the number of sites of the figure s that are occupied by atoms B; and $\varepsilon_{n,q,r}$ is the correlation of the order n. Since a pair of two neighboring sites is the minimum subfigure, the summation in Eq. (3) is performed from $q = 2 - r$ to $q = n - r$, where $r = 0$, 1, or 2. If the crystal is characterized only by the pair correlations $\varepsilon_{2,q,r} \equiv \varepsilon$ between atoms located in nearest neighboring sites, Eq. (3) takes the form

$$P_i^{(s)} = \langle \sigma_j(A) \rangle^{R^{(s)}-p} \langle \sigma_j(B) \rangle^p + \sum_{q=2-r}^{q=0} \langle \sigma_j(A) \rangle^{R^{(s)}-p-q} \langle \sigma_j(B) \rangle^{p-r} a_{q,r}^{(2)} \varepsilon. \quad (4)$$

In the absence of long-range order, the means of the occupation numbers are equal to the concentrations of components; i.e., $\langle \sigma_j(A) \rangle = y$ and $\langle \sigma_j(B) \rangle = 1 - y$ for the disordered solution A_yB_{1-y}. Therefore,

$$P_i^{(s)} = y^{(R^{(s)}-p)}(1-y)^p + \sum_{q=2, r=0}^{q=0, r=2} y^{(R^{(s)}-p-q)}(1-y)^{(p-r)} a_{q,r}^{(2)} \varepsilon. \quad (5)$$

From the definitions of the probability $P_i^{(s)}$ and multiplicity $\lambda_i^{(s)}$, the probability normalization condition is

$$\sum_{i \in s} \lambda_i^{(s)} P_i^{(s)} = 1. \quad (6)$$

If $l_i^{(s)}$ is the fraction of sites occupied by atoms A in the ith configuration of the figure s, the normalization condition for the composition of the solid solution A_yB_{1-y} is written as

$$\sum_{i \in s} l_i^{(s)} \lambda_i^{(s)} P_i^{(s)} = y. \quad (7)$$

In the general case, the cluster figure can include sites of several coordination spheres. If $n_{i(AA)_k}^{(s)}$, $n_{i(AB)_k}^{(s)}$, and $n_{i(BB)_k}^{(s)}$ are the relative numbers of the A–A, A–B, and B–B pairs, respectively, among all pairs of the kth coordination sphere of the ith configuration of the figure s, the normalization condition for the cluster probabilities to the probability of a certain pair bond in the kth sphere is written as

$$\sum_{i \in s} n_{i(AA)_k}^{(s)} \lambda_i^{(s)} P_i^{(s)} = \lambda_0^{(b_k)} P_0^{(b_k)},$$

$$\sum_{i \in s} n_{i(AB)_k}^{(s)} \lambda_i^{(s)} P_i^{(s)} = \lambda_1^{(b_k)} P_1^{(b_k)}, \quad (8)$$

$$\sum_{i \in s} n_{i(BB)_k}^{(s)} \lambda_i^{(s)} P_i^{(s)} = \lambda_2^{(b_k)} P_2^{(b_k)}.$$

The multiplicities of the A–A, A–B, and B–B pairs are equal to $\lambda_0^{(b_k)} = 1$, $\lambda_1^{(b_k)} = 2$, and $\lambda_2^{(b_k)} = 1$, respectively, for any k.

The cluster probabilities written with allowance for correlations must obviously satisfy normalization conditions (6)–(8). In addition, the probabilities $P_i^{(s)}$ cannot be negative. It is easy to verify that Eq. (5) satisfies all normalization conditions. To verify the satisfaction

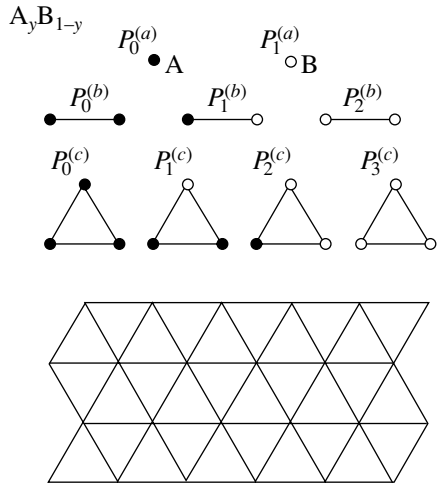

Fig. 1. Nonequivalent configurations and probabilities P of the figures a (site), b (pair bond), and c (triangular cluster) of the sequence $\{s\}$ used for describing the disordered solution A_yB_{1-y}, whose atoms (closed circle) A and (open circle) B are located in the sites of the regular triangular lattice.

of the condition that the probabilities are nonnegative, we first find the interval of variation in correlation as a function of the solid-solution content.

We consider the solid solution A_yB_{1-y} ($P_0^{(a)} = y$ and $P_1^{(a)} = 1 - y$) whose atoms are distributed over the sites of an arbitrary lattice with the pair correlation ε ($\varepsilon_{AA} = \varepsilon_{BB} \equiv \varepsilon$ and $\varepsilon_{AB} \equiv -\varepsilon$) in the first coordination sphere. In this case, the probabilities of nonequivalent A–A, A–B, and B–B pairs are equal to

$$P_0^{(b)} = y^2 + \varepsilon \geq 0, \quad P_1^{(b)} = y(1-y) - \varepsilon \geq 0, \quad P_2^{(b)} = (1-y)^2 + \varepsilon \geq 0, \tag{9}$$

respectively. According to Eqs. (9), the mathematically allowable region of variation in the pair correlation is

$$y(1-y) \geq \varepsilon \geq \begin{cases} -(1-y)^2, & \text{for} \quad y \geq 0.5, \\ -y^2, & \text{for} \quad y \leq 0.5. \end{cases} \tag{10}$$

Note that region (10) is the widest region of allowable values of the pair correlation ε. It coincides with the physically allowable regions of variation in ε for solid solutions A_yB_{1-y} with the square and bcc lattices. However, in many cases, the geometry of a particular lattice imposes restrictions on the mathematically allowable region of variation in ε and contracts it. In particular, for the solid solution A_yB_{1-y} with the regular triangular lattice, the physically allowable region of variation in ε has the form

$$y(1-y) \geq \varepsilon \geq \begin{cases} -(1-y)^2, & \text{for} \quad y \geq \dfrac{2}{3}, \\ -1/3 + y(1-y), & \text{for} \quad \dfrac{1}{3} \leq y \leq \dfrac{2}{3}, \\ -y^2, & \text{for} \quad y \leq \dfrac{1}{3}. \end{cases} \tag{11}$$

Let the atoms of the solid solution A_yB_{1-y} be located in the sites of the regular triangular lattice. To describe the triangular lattice, we use an equilateral-triangle cluster ($R^{(s)} = 3$), which has four nonequivalent configurations (Fig. 1): $P_0^{(c)}$ (three atoms A), $P_1^{(c)}$ (two atoms A and atom B), and $P_2^{(c)}$ (one atom A and two atoms B), and $P_3^{(c)}$ (three atoms B) with the multiplicities $\lambda_0^{(c)} = 1$, $\lambda_1^{(c)} = 3$, $\lambda_2^{(c)} = 3$, and $\lambda_3^{(c)} = 1$, respectively. The overlapping figures of the triangular clusters are bonds A–A, A–B, and B–B with the probabilities $P_i^{(b)}$, and the overlapping figures of the bonds are sites that are occupied by atoms A or B with the probability $P_i^{(a)}$. The triangular cluster and overlapping figures form the sequence $\{s\}$ of the figures that uniquely describe the lattice under consideration.

According to Eq. (5),

$$P_0^{(c)} = y^3 + 3y\varepsilon, \quad P_1^{(c)} = y^2(1-y) + (1-3y)\varepsilon, \quad P_2^{(c)} = y(1-y)^2 - (2-3y)\varepsilon, \quad P_3^{(c)} = (1-y)^3 + 3(1-y)\varepsilon. \tag{12}$$

Therefore, $P_i^{(c)} \geq 0$ only if the correlation ε varies in the interval

$$-\frac{y^2}{3} \leq \varepsilon \leq \frac{y(1-y)^2}{2-3y}, \quad \text{for} \quad 0 \leq y \leq \frac{1}{2}, \qquad -\frac{(1-y)^2}{3} \leq \varepsilon \leq \frac{y^2(1-y)}{3y-1}, \quad \text{for} \quad \frac{1}{2} \leq y \leq 1. \tag{13}$$

Interval (13) defines the region of the allowable values of the correlation ε for the disordered solution A_yB_{1-y} with the triangular lattice when formula (5) or (12) is used (Fig. 2). As seen in Fig. 2, this region is narrower than the mathematically allowable interval given by Eq. (10) and the physically allowable interval for the triangular lattice given by Eq. (11), and it cannot correctly include all allowable values of the pair correla-

tion ε. For this reason, for certain values of the correlation that lie in interval (11), some probabilities $P_i^{(c)}$ calculated by formula (5) or (12) are negative, which is forbidden. This means that the application of formulas (5) and (12) and more general formulas (3) and (4) proposed in [10, 11] yields a physically incorrect solution.

Thus, the use of conditional probability [8, 9] or decomposition in correlation moments [10, 11] for calculating the probabilities of multiparticle figures provides incorrect results, particularly for large correlation magnitudes. However, the problem can be solved by taking into account the maximum of the configurational entropy.

Indeed, in the high-temperature limit $T \longrightarrow \infty$ or low cluster energies $e_i^{(s)} \longrightarrow 0$, the free energy F of the solid solution is proportional to entropy with the negative sign; i.e., $F \sim -S$. Thus, the minimum of the free energy corresponds to the maximum of entropy. If only the pair correlation is specified and higher order correlations are equal to zero, then this is identical to the disordered distribution of pairs in the crystal for which the configurational entropy is maximal.

We again consider the solid solution A_yB_{1-y} whose atoms are distributed over the sites of the regular triangular lattice (Fig. 1) with the pair correlation ε in the first coordination sphere. The probabilities $P_i^{(b)}$ of pairs are described by formulas (9). Let us determine the probabilities $P_i^{(c)}$ of three-particle figures (triangular clusters). These probabilities must satisfy normalization conditions (6)–(8), which have the form

$$\begin{aligned} P_0^{(c)} + 3P_1^{(c)} + 3P_2^{(c)} + P_3^{(c)} &= 1, \\ P_0^{(c)} + 2P_1^{(c)} + P_2^{(c)} &= y, \\ P_0^{(c)} + P_1^{(c)} &= P_0^{(b)} = y^2 + \varepsilon. \end{aligned} \tag{14}$$

Following the cluster variation method [1, 5], we represent the configurational entropy S_c of a certain macroscopic state of the solid solution A_yB_{1-y} as

$$\begin{aligned} S_c(y, \varepsilon) &\equiv S_c(P_i^{(s)}) \\ &= -k_B N_A \sum_{s=a}^{c} y^{(s)} \sum_{i=s} \lambda_i^{(s)} P_i^{(s)} \ln P_i^{(s)}. \end{aligned} \tag{15}$$

For a chosen sequence of figures (site a, pair bond b, and triangular cluster c consisting of the nearest three sites) that describe the triangular lattice, the overestimate coefficients are equal to $y^{(a)} = 1$, $y^{(b)} = -3$, and

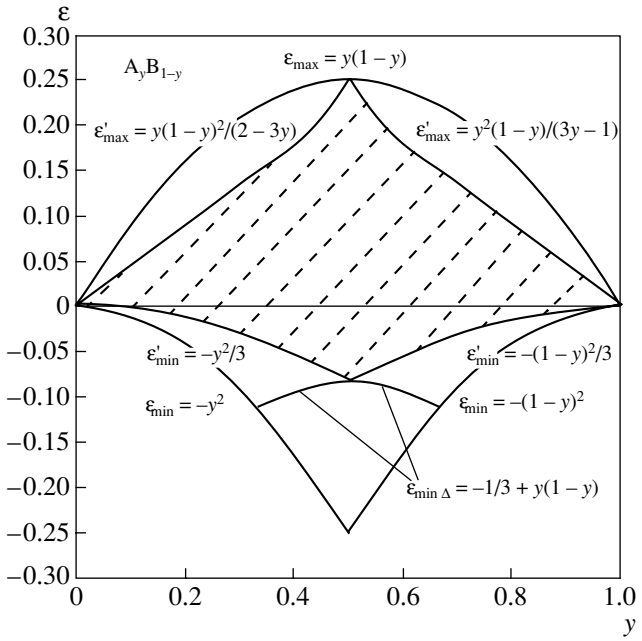

Fig. 2. Region of the mathematically allowable values of the pair correlation ε given by Eq. (10) in the disordered solution A_yB_{1-y} and the region of the allowable values of the correlation ε given by Eq. (11) for the triangular lattice. The shaded interval is given by Eq. (13) for ε' values, which follows from Eqs. (3)–(5) [10, 11] and (12), and $\varepsilon_{\min\Delta} = -\frac{1}{3} + y(1-y)$ is the minimum allowable pair correlation ε in the solid solution A_yB_{1-y} with the triangular lattice in the composition interval $\frac{1}{3} \le y \le \frac{2}{3}$.

$y^{(c)} = 2$ according to [5, 15]. Using these values and multiplicities $\lambda_i^{(s)}$, we write Eq. (15) as

$$\begin{aligned} S_c(y, \varepsilon) &= k_B[(P_0^{(a)} \ln P_0^{(a)} + P_1^{(a)} \ln P_1^{(a)}) \\ &- 3(P_0^{(b)} + 2P_1^{(b)} \ln P_1^{(b)} + P_2^{(b)} \ln P_2^{(b)}) \\ &+ 2(P_0^{(c)} \ln P_0^{(c)} + 3P_1^{(c)} \ln P_1^{(c)} + 3P_2^{(c)} \ln P_2^{(c)} + P_3^{(c)} \ln P_3^{(c)})]. \end{aligned} \tag{16}$$

Solving system of equations (14), we express the probabilities $P_1^{(c)}$, $P_2^{(c)}$, and $P_3^{(c)}$ in terms of y, ε, and the probability $P_0^{(c)}$ of the complete triangular cluster and substitute the expressions into Eq. (16). In the maximum of the configurational entropy,

$$\frac{\partial S_c(P_i^{(s)})}{\partial P_0^{(c)}} \equiv \frac{\partial S_c(y, \varepsilon, P_0^{(s)})}{\partial P_0^{(c)}} = 0. \tag{17}$$

Differentiating Eq. (16) and explicitly solving Eq. (17)

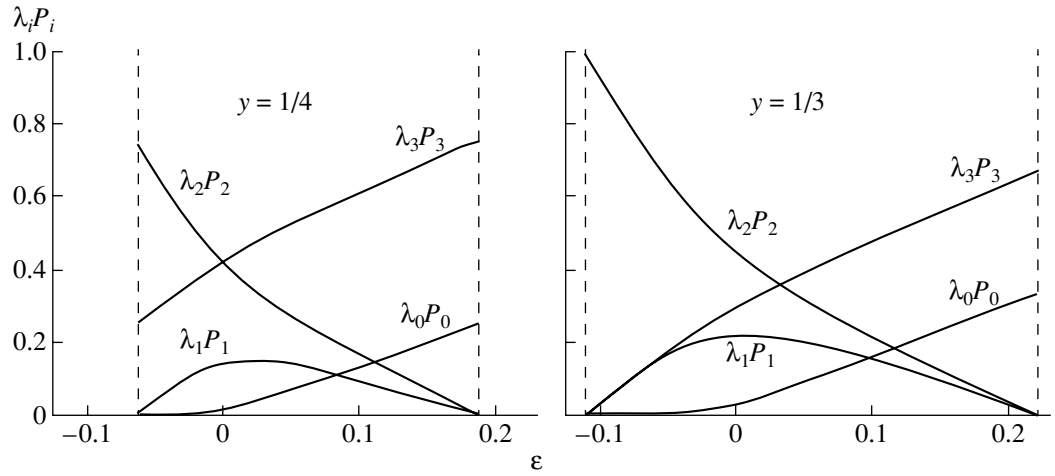

Fig. 3. Probabilities $\lambda_0^{(c)}P_0^{(c)}$, $\lambda_1^{(c)}P_1^{(c)}$, $\lambda_2^{(c)}P_2^{(c)}$, and $\lambda_3^{(c)}P_3^{(c)}$ of the triangular clusters vs. the correlation ε in the disordered solid solution A_yB_{1-y} $\left(y = \frac{1}{4} \text{ and } \frac{1}{3}\right)$ with the triangular lattice. The dashed lines are the boundary values of the correlation ε.

with respect to $P_0^{(c)}$, we obtain

$$P_0^{(c)} = y(y^2 + \varepsilon) + \varepsilon - [y(1-y) - \varepsilon]A,$$

$$P_1^{(c)} = y[y(1-y) - \varepsilon)] + [y(1-y) - \varepsilon]A,$$
$$P_2^{(c)} = (1-y)[y(1-y) - \varepsilon)] - [y(1-y) - \varepsilon]A, \quad (18)$$

$$P_3^{(c)} = (1-y)[(1-y)^2 + \varepsilon] + \varepsilon + [y(1-y) - \varepsilon]A,$$

where

$$A = \left\{\frac{\varepsilon(1-2y)}{2}\right.$$

$$\left. + \frac{1}{18}[81\varepsilon^2(1-2y)^2 + 12(y - y^2 + 2\varepsilon)^3]^{1/2}\right\}^{1/3} \quad (19)$$

$$+ \left\{\frac{\varepsilon(1-2y)}{2} - \frac{1}{18}[81\varepsilon^2(1-2y)^2 + 12(y - y^2 + 2\varepsilon)^3]^{1/2}\right\}^{1/3}.$$

The resulting solution is general for all y and ε values satisfying boundary conditions (11) (see Fig. 2). Actually, it is the solution for the case where the probability of any configuration of the triangular cluster is not equal to zero. Figure 3 shows the probabilities $\lambda_i^{(c)}P_i^{(c)}$ as functions of the correlation ε for $y = \frac{1}{4}$ and $\frac{1}{3}$. For a particular case where $\varepsilon = -(1-y)^2$ and $y > \frac{2}{3}$, B–B bonds are absent and the lattice is free of the configurations $P_2^{(c)}$ and $P_3^{(c)}$; i.e., $P_2^{(c)} = P_3^{(c)} = 0$. For this reason, only the configurations $P_0^{(c)}$ and $P_1^{(c)}$ are involved in the normalization conditions. Therefore, the solution has the form $P_0^{(c)} = 3y - 2$ and $P_1^{(c)} = 1 - y$. If $\varepsilon = -y^2$ and $y < \frac{1}{3}$; i.e., A–A bonds are absent, a similar solution has the form $P_0^{(c)} = 0$, $P_1^{(c)} = 0$, $P_2^{(c)} = y$, and $P_3^{(c)} = 1 - 3y$.

Maximalizing the configurational entropy, we obtain particular solutions for the solid solution A_yB_{1-y} with the square and fcc lattices. If $\varepsilon = -(1-y)^2$ and $y > 0.5$, B–B bonds are absent in these lattices and there are only three configurations of the basis cluster. For the square lattice, these are a square consisting of four atoms A ($\lambda_0^{(c)} = 1$), a square consisting of three atoms A and one atom B ($\lambda_1^{(c)} = 4$), and a square consisting of two nonadjacent atoms A and two nonadjacent atoms B ($\lambda_2^{(c)} = 2$); and $y^{(a)} = y^{(c)} = 1$ and $y^{(b)} = -2$. In the fcc lattice, these configurations are the complete octahedral cluster ($\lambda_0^{(c)} = 1$), an octahedron with one atom of the other type ($\lambda_1^{(c)} = 6$), and an octahedron with two atoms of the other type that are located diagonally to each other ($\lambda_2^{(c)} = 3$), and $y^{(a)} = 7$, $y^{(b)} = -6$, and $y^{(c)} = 1$.

The solution for the square lattice when $\varepsilon = -(1-y)^2$ and $y > 0.5$ has the form

$$P_0^{(c)} = -(1-y^2-\varepsilon) + [(1-y^2-\varepsilon)^2 + (y^2+\varepsilon)^2]^{1/2},$$

$$P_1^{(c)} = \frac{1}{2} - \frac{1}{2}[(1-y^2-\varepsilon)^2 + (y^2+\varepsilon)^2]^{1/2}, \quad (20)$$

$$P_2^{(c)} = -\frac{1}{2}(y^2+\varepsilon) + \frac{1}{2}[(1-y^2-\varepsilon)^2 + (y^2+\varepsilon)^2]^{1/2}.$$

The solution for the fcc lattice when $\varepsilon = -(1-y)^2$ and $y > 0.5$ has the form

$$P_0^{(c)} = \frac{1}{4}[6(y^2+\varepsilon) - 5] + \frac{3}{4}[6(y^2+\varepsilon)^2 - 8(y^2+\varepsilon) + 3]^{1/2},$$

$$P_1^{(c)} = \frac{1}{4} - \frac{1}{4}[6(y^2+\varepsilon)^2 - 8(y^2+\varepsilon) + 3]^{1/2}, \quad (21)$$

$$P_2^{(c)} = \frac{1}{4}[1-2(y^2+\varepsilon)] + \frac{1}{4}[6(y^2+\varepsilon)^2 - 8(y^2+\varepsilon) + 3]^{1/2}.$$

Similar solutions for the solid solution A_yB_{1-y} with the square and fcc lattices, when $\varepsilon = -y^2$ and $y < 0.5$ (in this case, A–A bonds are absent in these lattices) are obtained from Eqs. (20) and (21), respectively, by changing y^2 to $(1-y)^2$.

All the sites of the triangular cluster of the regular triangular lattice are located in the first coordination sphere with respect to each other. Hence, using solution (18), one cannot determine whether the presence of correlation in the first coordination sphere leads to the appearance of correlations in the second and subsequent coordination spheres. The square and octahedral clusters include sites located in the first and second coordination spheres with respect to each other. Using formula (8), probabilities (20) and (21), and known coefficients $n_{i(\mathrm{AB})_2}^{(c)}$, one can calculate the probabilities of pair bonds in the second coordination sphere and, correspondingly, the pair correlation in the second coordination sphere. For the square cluster in the square lattice, $n_{0(\mathrm{AB})_2}^{(c)} = n_{2(\mathrm{AB})_2}^{(c)} = 0$ and $n_{1(\mathrm{AB})_2}^{(c)} = \frac{1}{2}$. For the octahedral cluster in the fcc lattice, $n_{0(\mathrm{AB})_2}^{(c)} = n_{2(\mathrm{AB})_2}^{(c)} = 0$ and $n_{1(\mathrm{AB})_2}^{(c)} = \frac{1}{3}$. The above calculation shows that, for the square lattice, when $\varepsilon = -(1-y)^2$ and $y > 0.5$, the probability of the A–B bond in the second coordination sphere differs from the binomial law:

$$\lambda_1^{(b_2)} P_1^{(b_2)} = 2P_1^{(c)} = 1 - [(1-y^2-\varepsilon)^2 + (y^2+\varepsilon)^2]^{1/2}. \quad (22)$$

The correlation $\varepsilon_{\mathrm{AB}}$ in the jth coordination sphere is equal to $\varepsilon_{\mathrm{AB}_j} = P_{\mathrm{AB}}^{(j)} - P_{\mathrm{AB}}^{\mathrm{bin}}$. Since $\varepsilon_{\mathrm{AB}_j} = -\varepsilon_{\mathrm{AA}_j} \equiv -\varepsilon_j$ and $P_1^{(b_2)} \equiv P_{\mathrm{AB}}^{(2)}$ (22) for the square lattice when $\varepsilon = -(1-y)^2 < 0$ and $y > 0.5$, the correlation $\varepsilon_2 \equiv \varepsilon_{\mathrm{AA}_2}$ in the second coordination sphere is calculated as

$$\varepsilon_2 = y(1-y) - \frac{1}{2} + \frac{1}{2}[(1-y^2-\varepsilon)^2 + (y^2+\varepsilon)^2]^{1/2} > 0. \quad (23)$$

Similarly, for the fcc lattice when $\varepsilon = -(1-y)^2 < 0$ and $y > 0.5$, the probability $P_1^{(b_2)} \equiv P_{\mathrm{AB}}^{(2)}$ of the A–B pair and the pair correlation $\varepsilon_2 \equiv \varepsilon_{\mathrm{AA}_2}$ in the second coordination sphere have the form

$$\lambda_1^{(b_2)} P_1^{(b_2)} = 2P_1^{(c)} = \frac{1}{2} - \frac{1}{2}[6(y^2+\varepsilon)^2 - 8(y^2+\varepsilon) + 3]^{1/2}, \quad (24)$$

$$\varepsilon_2 = y(1-y) - \frac{1}{4} + \frac{1}{4}[6(y^2+\varepsilon)^2 - 8(y^2+\varepsilon) + 3]^{1/2} > 0. \quad (25)$$

Thus, the presence of pair correlation, i.e., short-range order, in the first coordination sphere of the square and fcc lattices gives rise to at least the appearance of the opposite correlation in the second coordination spheres of these lattices. This conclusion is consistent with the computer simulation of the short-range order [7] in the carbon fcc sublattices of the titanium carbide $TiC_y\square_{1-y}$. As was shown in [7], the existence of short-range order in the first coordination sphere of the fcc lattice is accompanied by the appearance of the short-range order with the opposite sign in the second, third, and fourth coordination spheres.

On a whole, the method proposed for determining the probabilities of the multiparticle figures with the inclusion of correlation is applicable to the analytical description of not only 2D lattices but also a particular case of 3D lattices. The development of the method will provide the solution of a more complex problem of the simultaneous inclusion of the short- and long-range orders in ordering systems.

ACKNOWLEDGMENTS

This work was supported by the Russian Foundation for Basic Research, project no. 03-03-32031.

REFERENCES

1. M. Kurata, R. Kikuchi, and T. Watari, J. Chem. Phys. **21** (3), 434 (1953).
2. A. G. Khachaturian, *Theory of Structural Transformations in Solids* (Nauka, Moscow, 1974; Wiley, New York, 1983).

3. A. I. Gusev and A. A. Rempel, Phys. Status Solidi B **131** (1), 43 (1985).
4. A. I. Gusev and A. A. Rempel, *Nonstoichiometry, Disorder, and Order in Solids* (Ural. Otd. Ross. Akad. Nauk, Yekaterinburg, 2001) [in Russian].
5. A. I. Gusev, A. A. Rempel, and A. J. Magerl, *Disorder and Order in Strongly Nonstoichiometric Compounds. Transition Metal Carbides, Nitrides and Oxides* (Springer, Berlin, 2001).
6. A. I. Gusev, Fiz. Tverd. Tela **32** (9), 2752 (1990) [Sov. Phys. Solid State **32**, 1595 (1990)].
7. A. V. Safonov, A. A. Rempel', and A. I. Gusev, Izv. Vyssh. Uchebn. Zaved., Fiz. **43** (11), 214 (2000).
8. A. Von Heilmann and W. Zinn, Z. Metallkd. **58** (2), 113 (1967).
9. O. Brummer, G. Drager, and I. Mistol, Ann. Phys. (New York) **28** (2), 135 (1972).
10. F. A. Sidorenko, Fiz. Tverd. Tela **23** (11), 3514 (1981) [Sov. Phys. Solid State **23**, 2046 (1981)].
11. F. A. Sidorenko, P. V. Geld, V. Ya. El'ner, and B. V. Ryzhenko, J. Phys. Chem. Solids **43** (3), 297 (1982).
12. A. I. Gusev, *Physical Chemistry of Nonstoichiometric Refractory Compounds* (Nauka, Moscow, 1991) [in Russian].
13. M. A. Krivoglaz, *Theory of X-ray and Thermal Neutron Scattering by Real Crystals* (Nauka, Moscow, 1967; Plenum Press, New York, 1969).
14. N. I. Andreev, *Correlation Theory of Statistically Optimal Systems* (Nauka, Moscow, 1966; W.B. Saunders Co., Philadelphia, 1969).
15. J. Hijmans and J. de Boer, Physica A **21** (6), 471 (1955).

Translated by R. Tyapaev

Doklady Physics, Vol. 50, No. 1, 2005, pp. 25–27. Translated from Doklady Akademii Nauk, Vol. 400, No. 3, 2005, pp. 330–332.

PHYSICS

Numerical Method for Solving Two-Dimensional Magnetohydrodynamic Equations with Allowance for the Hall Effect

A. V. Ivanovskiĭ and V. Sh. Shaĭdullin

Presented by Academician R.I. Il'kaev July 8, 2004

Received August 31, 2004

The magnetohydrodynamic equations are usually used for the simulation of plasma in the hydrodynamic approximation. This system of equations comprises the equations of motion of plasma, the electromagnetic field equations, the equations describing the heating of electronic and ionic components, and the equations for the external electric circuit. Numerical methods of combining the first two sets of equations with the artificial inclusion of the Hall effect have already been developed [1, 2]. In this paper, we present an effective method for solving the complete system of magnetohydrodynamic equations with allowance for the Hall effect. We implement the method to simulate a single-fluid two-temperature plasma on a two-dimensional Euler mesh in the cylindrical coordinates (r, z).

BASIC EQUATIONS OF THE NUMERICAL MODEL

We simulate a plasma composed of ions with the density N_i and average charge Z_i and of electrons with the density $N = Z_i N_i$. The density ρ and hydrodynamic velocity $\mathbf{U}$ of the plasma are taken as the density and mass velocity of ions, respectively. The plasma dynamics is described by the continuity equation and the equation of motion subject to the electromagnetic force $\mathbf{F}_{\text{em}} = \dfrac{[\boldsymbol{j} \times \boldsymbol{B}]}{c}$. The specific internal energies $\varepsilon_i(\rho, T_i)$ and $\varepsilon_e(\rho, T_e)$ and the pressures $P_i = P_i(\rho, T_i)$ and $P_e = P_e(\rho, T_e)$ correspond to the temperatures T_i and T_e of the plasma components, respectively. The energy balance involves the intercomponent energy transfer $Q_{ei} = \beta(P, T, B)(T_e - T_i)$ and the Joule heating Q_J. In addition to the magnetic-field transport due to both macroscopic motion and diffusion, which is taken into account as usual, we allow for the transfer owing to the Hall effect. In this case, the magnetohydrodynamic equations take the form

$$\frac{\partial \rho}{\partial t} + \operatorname{div}(\rho \mathbf{U}) = 0,$$

$$\frac{\partial \rho \mathbf{U}}{\partial t} + \mathbf{U}\operatorname{div}(\rho \mathbf{U}) + (\rho \mathbf{U}\nabla)\mathbf{U} = -\nabla(P_i + R_e) + \mathbf{F}_{\text{em}},$$

$$\rho\left(\frac{\partial \varepsilon_i}{\partial t} + (\mathbf{U}\nabla)\varepsilon_i\right) = -P_i \operatorname{div}\mathbf{U} + \operatorname{div}\kappa_i \nabla T_i + Q_{ei},$$

$$\rho\left(\frac{\partial \varepsilon_e}{\partial t} + (\mathbf{V}^e\nabla)\varepsilon_e\right) = -P_e \operatorname{div}\mathbf{V}^e + \operatorname{div}\kappa_e \nabla T_e - Q_{ei} + Q_J,$$

$$\frac{\partial \mathbf{B}}{\partial t} - \operatorname{curl}[\mathbf{U} \times \mathbf{B}] = -c\operatorname{curl}\mathbf{E}, \quad j = \frac{c}{4\pi}[\nabla \times \mathbf{B}],$$

$$\mathbf{E} = \frac{\mathbf{j}}{\sigma} + \frac{[\mathbf{j} \times \mathbf{B}]}{ceN_e}.$$

Here, c is the speed of light; $\mathbf{j}$ is the current density; $\mathbf{B}$ is the magnetic field strength; $\mathbf{E}$ is the electric field strength; $\sigma(P, T, B)$ and $\kappa(P, T, B)$ are the electrical and thermal conductivities, respectively; and $\mathbf{V}^e = \mathbf{U} - \dfrac{\mathbf{j}}{eN_e}$ is the velocity of the electron liquid. The disregard of displacement currents negligibly influences the simulation results.

For axisymmetric flows, $\mathbf{U} = (U_r, 0, U_z)$, $\mathbf{B} = (0, B_\varphi, 0)$, $\mathbf{j} = (j_r, 0, j_z)$, and $\mathbf{E} = (E_r, 0, E_z)$. In this case, all the quantities depend only on $r \in [R_{\min}, R_{\max}]$ and $z \in [Z_{\min}, Z_{\max}]$. We impose the following initial and boundary conditions.

For the equations of motion: $S_z(r, z) = S_r(r, z) = 0$, $\rho = \rho_0(r, z)$, and $S_z(r, Z_{\min}) = S_z(r, Z_{\max}) = S_r(R_{\min}, z) = S_r(R_{\max}, z) = 0$, where $S_r = \rho U_r$ and $S_z = \rho U_z$ are the radial and axial momentum densities, respectively.

Russian Federal Nuclear Center VNIIEF, pr. Mira 37, Sarov, Nizhegorodskaya oblast, 607188 Russia

1028-3358/05/5001-0025$26.00

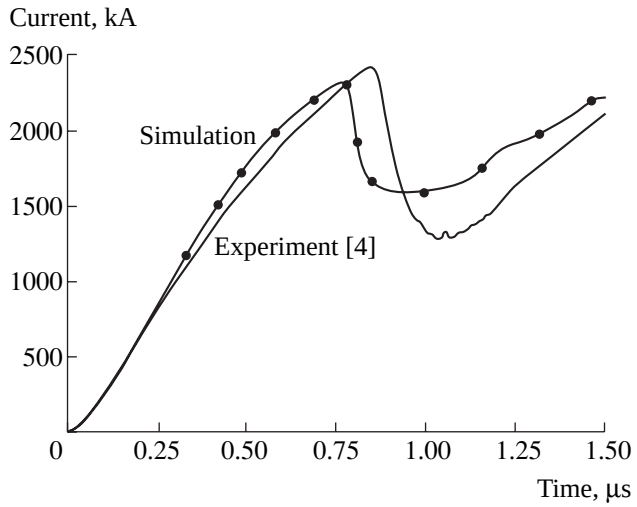

Fig. 1. Current through the plasma opening switch.

For electromagnetic field equations: $B_\varphi(r, z) = 0$, $B_\varphi(r, Z_{\min}) = -\dfrac{2I_2(t)}{r}$, $R_{\min} \le r \le r_k$; $E_r(r, Z_{\min}) = E_r(r, Z_{\max}) = E_z(R_{\min}, z) = E_z(R_{\max}, z) = 0$.

For heat transfer equations: $T_i = T_{0i}(r, z)$, $T_e = T_{0e}(r, z)$, $T_i(r, Z_{\min}) = \varphi_1(r)$, $T_i(r, Z_{\max}) = \varphi_2(r)$, $T_i(R_{\min}, z) = \varphi_3(z)$, $T_i(R_{\max}, z) = \varphi_4(z)$, $T_e(r, Z_{\min}) = \phi_1(r)$, $T_e(r, Z_{\max}) = \phi_2(r)$, $T_e(R_{\min}, z) = \phi_3(z)$, and $T_e(R_{\max}, z) = \varphi_4(z)$.

Basic difficulties of the simulation are due to the nonlinear terms in the electromagnetic field equations:

$$\frac{\partial B_\varphi}{\partial t} = -\frac{\partial(B_\varphi U_r)}{\partial r} - \frac{\partial(B_\varphi U_z)}{\partial z} - c\frac{\partial E_r}{\partial z} + c\frac{\partial E_z}{\partial r},$$

$$E_r = -\frac{c}{4\pi\sigma}\frac{\partial B_\varphi}{\partial z} + C_z B_\varphi, \quad C_z = -\frac{c}{4\pi e N_e}\frac{1}{r}\frac{\partial(rB_\varphi)}{\partial r},$$

$$E_z = \frac{c}{4\pi\sigma}\frac{1}{r}\frac{\partial(rB_\varphi)}{\partial r} - C_r B_\varphi, \quad C_r = +\frac{c}{4\pi e N_e}\frac{\partial B_\varphi}{\partial z}.$$

These equations include the transfer terms proportional to the radial C_r and axial C_z velocities, which are usually assumed to be zero. The velocities C_r and C_z are proportional to the spatial derivatives of B and inversely proportional to the plasma density. The corresponding terms are pronounced in low-density regions; i.e., an analog of the Kingsepp–Mokhov–Chukbar effect takes place [3]. The method proposed here allows us to overcome this difficulty. For an arbitrary numerically stable algorithm for solving the time-dependent equation, all quantities for the computational discrete mesh and for all grid functions should be approximated with minimum errors. We developed and analyzed a multipoint iteration approximation of the quantities C_z and C_r, which allowed us to find smooth solutions up to second-order accuracy.

RESULTS AND DISCUSSION

We tested the method and code by the numerical simulation of the experiments reported in [4, 5]. As is seen in Fig. 1, the calculation results are in close agreement with the current measurements [4] with a plasma opening switch. A change in the cathode radius $R_{\min}$ by 0.5 cm results in a change in the current switching moment by 30 ns. The plasma opening switch is similarly sensitive to the parameters of both the plasma and the electric circuit. The calculation results are in accordance with the measurements of generator current and load current [5].

The potentialities of the method and code were demonstrated by simulating the operation of the plasma opening switch constructed at the Russian Federal Nuclear Center VNIIEF (see Fig. 2) [6]. A capacitor bank or a magnetic explosion generator can serve as an energy source S_1 for such an interrupter. The operation of the plasma opening switch was simulated with various input data; namely, we varied the dimensions of the chamber, the characteristics of the plasma, and the parameters of the electric circuit. We here present the calculation results for the case of the capacitor bank, taking the following parameters: bank capacitance C_1 =

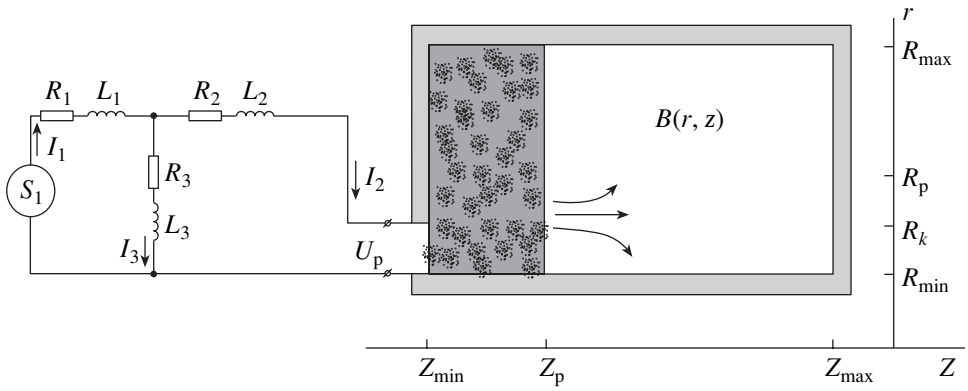

Fig. 2. Electrical circuit and layout of the plasma opening switch constructed at the Russian Federal Nuclear Center VNIIEF [6]: $Z_{\min}$, $Z_{\max}$, $R_{\min}$, $R_{\max}$, and R_k are the linear dimensions of the chamber; and Z_p and r_p are the initial sizes of the plasma sheath.

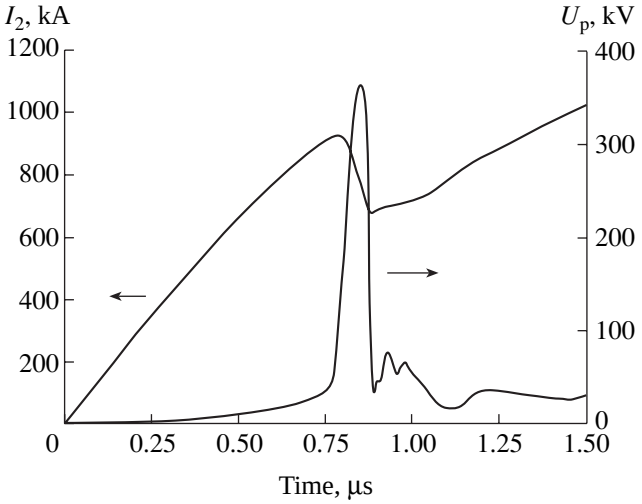

Fig. 3. Time dependences of the total current I_2 and voltage U_p at the input of the plasma opening switch chamber developed at VNIIEF [6].

32 μF, initial voltage U_{C_1} = 100 kV, R_1 = 4 mΩ, L_1 = 70 nH, $R_2 = 0$, $L_2 = L_3 = 0$, $R_3 = \infty$, cathode radius R_{min} = 6 cm, anode radius R_{max} = 12 cm, chamber radius R_{max} = 12 cm, high-voltage input radius R_k = 6 cm, $Z_{min} = 0$, Z_{max} = 40 cm, the initial length of the plasma sheath Z_p = 4 cm, initial plasma (nitrogen) density $\rho_0(r, z)$ = 0.1 μg cm^{-3}, and initial plasma temperature $\varphi_i = \phi_i$ = 1 eV. The electric circuit was described by the Kirchhoff equations. We studied the space–time development of the magnetic field and plasma density in the plasma opening switch chamber. We observed the plasma ejection from the cathode to the anode and the subsequent penetration of the magnetic field into the gap along the cathode. Figure 3 shows the current I_2 through the plasma opening switch and its input voltage, which was evaluated from the equations

$$U_p = \frac{d}{dt}\int\limits_{(S)} BdS, \quad S = (Z_p - Z_{min})(R_{max} - R_{min}).$$

It is seen that the electrical resistance of the chamber increases stepwise because of the current breakdown in the plasma opening switch, i.e., the current flip-over into load.

Thus, we developed a two-dimensional method for solving the magnetohydrodynamic equations in single-fluid two-temperature approximation with allowance for the Hall effect. The method was tested by the numerical simulation of actual plasma opening switches. The time dependences of the current evaluated are in close agreement with published experimental data. The potentialities of the method and code are demonstrated by the detailed simulation of the plasma opening switch constructed at the Russian Federal Nuclear Center VNIIEF. We are going to develop the method in order to allow for the measurement of more delicate effects.

ACKNOWLEDGMENTS

We are grateful to Prof. L.P. Babich for valuable remarks and help in this work.

REFERENCES

1. J. D. Huba, J. M. Grossmann, and P. F. Ottinger, Phys. Plasmas **1**, 3444 (1994).
2. O. Z. Zabaydullin, Phys. Plasmas **7**, 1321 (2000).
3. A. S. Kingsep, Yu. V. Mokhov, and K. V. Chukbar, Fiz. Plazmy **10**, 854 (1984) [Sov. J. Plasma Phys. **10**, 495 (1984)].
4. W. Rix, P. Coleman, R. Thompson, *et al.*, IEEE Trans. Plasma Sci. **PS-25**, 169 (1997).
5. D. Hinshelwood, B. Weber, J. Grossmann, *et al.*, Phys. Rev. Lett. **68**, 3567 (1992).
6. K. I. Almazova, A. S. Boriskin, V. V. Borovkov, *et al.*, Zh. Tekh. Fiz. **73**, 125 (2003) [Tech. Phys. **48**, 920 (2003)].

Translated by V. Chechin

Doklady Physics, Vol. 50, No. 1, 2005, pp. 28–31. Translated from Doklady Akademii Nauk, Vol. 400, No. 3, 2005, pp. 333–337.

PHYSICS

Effect of the Structure of the $Ni_{2.14}Mn_{0.81}Fe_{0.05}Ga$ Alloy on the Temperature Dependence of Magnetization

R. N. Imashev[1], Kh. Ya. Mulyukov[2], V. V. Koledov[2], and V. G. Shavrov[3]

Presented by Academician A.S. Bugaev August 18, 2004

Received August 18, 2004

The physical properties of solids change significantly upon creating a nanocrystalline structure in them by the method of severe plastic deformation, i.e., by grinding crystals to sizes of 10–100 nm under high pressure without a change in density [1]. The remarkable combination of high strength and plasticity is observed in nanocrystalline materials thus obtained. This phenomenon, called superplasticity, is associated with an increase in the threshold of formation of dislocations in the nanocrystalline structure and with an increase in the role of quasi-morphized atoms, which form the boundaries of nanosize crystallites. The observation of the strong effect of the nanocrystalline structure on the magnetic properties of ferromagnetic metals Ni and Dy is also of interest [2, 3]. Attention should be paid to the recent works [4, 5] devoted to nonferromagnetic nanocrystalline NiTi-based alloys exhibiting the shape-memory effect. In those works, the possibility of both the complete amorphization of alloys and the smooth formation of the nanocrystalline structure in them by means of annealing was demonstrated. In an amorphized nanocrystalline alloy, the disappearance of property jumps, which are characteristic of a thermoelastic martensitic transformation, can be observed. The subsequent annealing allows the smooth recovery of both the structure, by gradually increasing the size of crystallites, and thereby the martensitic transformation. It was convincingly shown that annealing not only recovers the martensitic transformation with the inherent thermomechanical memory effects and increases plasticity and strength but also qualitatively affects thermomechanical memory effects (contracts the temperature hysteresis loop of the martensitic transformation and increases the restoring strain).

Heusler alloys of the Ni_2MnGa family are characterized by the rare combination of physical properties such as the thermoelastic structural transition and ferromagnetic order. As a result, the structural transition in them is sensitive to a magnetic field; the reversible structural transition with respect to the field at constant temperature, as well as the shape memory effect controlled by the magnetic field, can be observed [6–8]. In single crystals of this alloy, giant (up to 10%) magnetically induced strains are found. They are attributed to the effect of the magnetic field on the twinning structure of the low-temperature martensitic phase of the alloy [9]. The aim of this work is to obtain and analyze the nanocrystalline ferromagnetic alloy $Ni_{2.14}Mn_{0.81}Fe_{0.05}Ga$ exhibiting the shape memory effect, to search for the effects of severe plastic deformation on the structural transition and magnetic order in this material, and to study the effect of subsequent annealing on both the magnetic order and the structural martensitic transformation.

Nanocrystalline samples were fabricated from the initial polycrystalline plates of the $Ni_{2.14}Mn_{0.81}Fe_{0.05}Ga$ alloy by the method of severe plastic deformation—torsion by 5–10 turns in Bridgman anvils under a pressure of 6 GPa at room temperature.

The microstructure of the initial coarse-crystalline sample was studied by an AXIOVERT 100A metallographic optical microscope equipped with a digital video camera and a computer. As is seen on the image of the microstructure (Fig. 1) obtained at a temperature of 283 K (low-temperature phase), the coarse-crystalline sample is a polycrystal with a mean grain size of 0.5 mm. Characteristic martensitic plates are observed in grains. Cracks, which are obviously responsible for the brittleness of the sample, are clearly seen at the boundary of the grains.

The microstructure of the nanocrystalline state of this alloy was studied by a JEM-2000EX transmission electron microscope. As is seen in the image of the microstructure (Fig. 2), the sample subjected to plastic deformation consists of very small crystallites without

[1] *Bashkortostan State University, ul. Frunze 32, Ufa, 450007 Bashkortostan, Russia*
e-mail: ram79@mail.ru

[2] *Institute for Metals Superplasticity Problems, Russian Academy of Sciences, ul. Khalturina 39, Ufa, 450001 Bashkortostan, Russia*
e-mail: mulyuk@anrb.ru; koledov@cplire.ru

[3] *Institute of Radio Engineering and Electronics, Russian Academy of Sciences, ul. Mokhovaya 17/7, Moscow, 125009 Russia*
e-mail: shavrov@cplire.ru

1028-3358/05/5001-0028$26.00

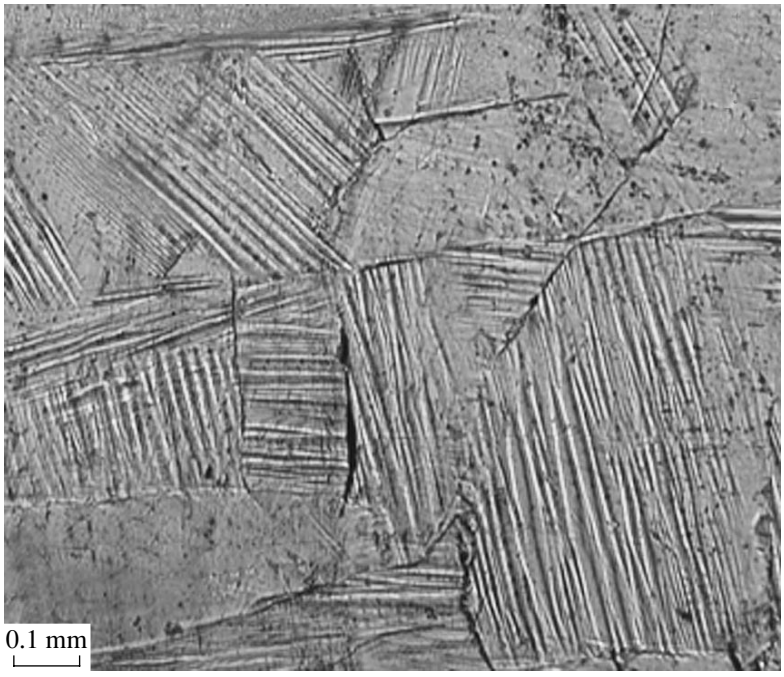

Fig. 1. Microstructure of the $Ni_{2.14}Mn_{0.81}Fe_{0.05}Ga$ alloy in the coarse-crystalline state.

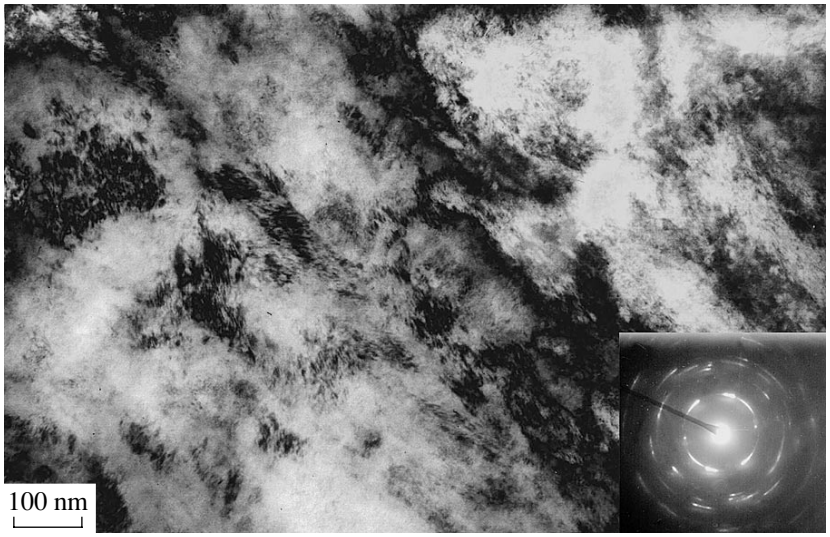

Fig. 2. Microstructure and (inset) the electron-diffraction pattern of the $Ni_{2.14}Mn_{0.81}Fe_{0.05}Ga$ alloy in the nanocrystalline state.

distinct boundaries between them. The azimuthal spread of reflections on the electron-diffraction pattern indicates that the crystallographic axes of crystallites in the nanocrystalline structure are disoriented by large angles. The mean grain size determined from the dark-field image is equal to 40 nm.

The temperature dependences of the magnetization $\sigma(T)$ of the alloy samples under investigation were recorded on an automatic magnetometer [10]. This dependence was studied because it is very informative and distinctly presents both magnetic and structural transitions. Figure 3 shows the set of the temperature dependences of the magnetization $\sigma(T)$ measured upon heating for a sample with the coarse-crystalline structure for various magnitudes of the external magnetic field H. As is seen, the dependences $\sigma(T)$ are complex and differ from $\sigma(T)$ for typical ferromagnetic materials. In particular, a dip is seen in line *1*, obtained in a field of H = 80 kA/m at a temperature of 270 K. At the bottom of the dip, magnetization is almost constant when the temperature increases to 293 K. Then, σ

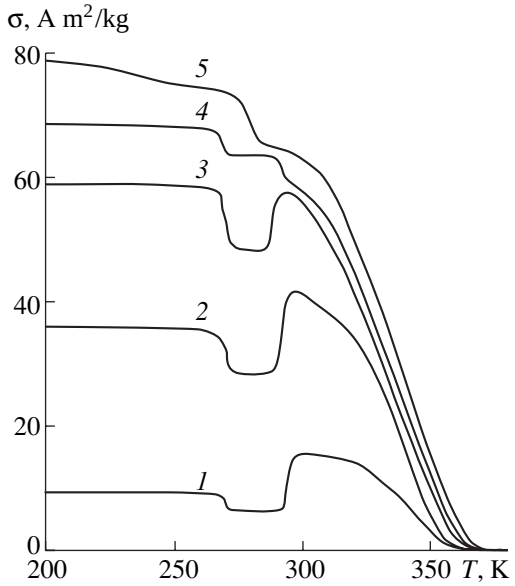

Fig. 3. Temperature dependence of magnetization in the coarse-crystalline state as measured in magnetic fields of (*1*) 80, (*2*) 160, (*3*) 220, (*4*) 400, and (*5*) 720 kA/m.

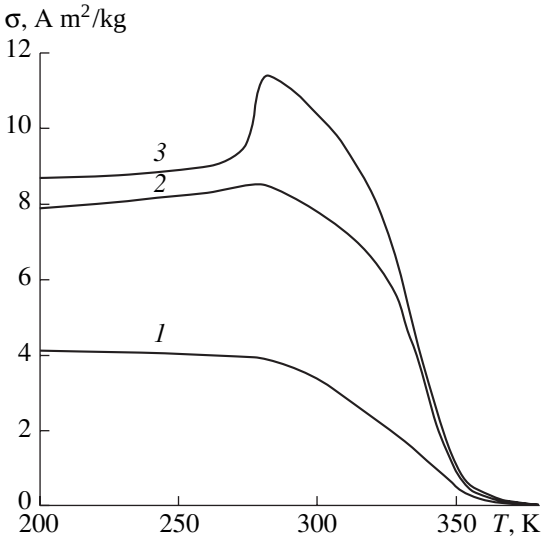

Fig. 4. Temperature dependence of magnetization measured in a magnetic field of 80 kA/m for the states obtained by the annealing of the nanocrystalline sample at temperatures (*1*) 623, (*2*) 673, and (*3*) 773 K.

increases abruptly and becomes maximal at a temperature of about 300 K. We emphasize that the magnetization before the dip is much lower than the value at the maximum. The heating of the sample above 300 K leads to a decrease in σ to zero, which is characteristic of ferromagnetic materials, with a Curie point of 357 K. For H = 160 kA/m (line *2*), the dip becomes deeper. In this case, the difference of the magnetizations at the boundaries of the dip decreases. In line *3*, obtained for H = 220 kA/m, the magnetizations at the boundaries of the dip become equal to each other. For H = 400 kA/m (line *4*), σ decreases abruptly at 270 K, as in the first three lines. The maximum that exists in weaker magnetic fields is absent in this line, and it degenerates to the point of inflection. The further increase in H to 720 kA/m (line *5*) leads to smoothing of the σ(T) plot.

The formation of the dip in the σ(T) plot for certain Ni–Mn–Ga alloys is also observed in other works [11, 12]. A sharp decrease in σ at T = 270 K in relatively weak magnetic fields can likely be attributed to the fact that a different magnetic order is formed at this temperature due to a change in the interatomic distance, because the exchange interaction responsible for the magnetic order is a function of the interatomic distance. The magnetic moments of Ni, Mn, and Fe atoms, which are involved in the formation of the sample magnetization, can form the corresponding magnetic order in dependence on the magnitude and sign of the exchange integral. The disappearance of the dip with the subsequent maximum at H = 720 kA/m can be attributed to the fact that a strong field returns the orientation of the atomic magnetic moments to the parallel orientation along the field and any spin-reorientation phase transition is absent in this case. The change in the interatomic distance that leads to the formation of the different magnetic order at 270 K is apparently induced by the transition of the unmodulated *T* martensite to the modulated *M* martensite [12], which is transformed to the high-temperature cubic phase (austenite) when the temperature increases to 293 K.

The alloy under consideration in the nanocrystalline state does not exhibit ferromagnetic properties. This fact can apparently be explained by both disordering of atoms of the alloy upon severe plastic deformation [13] and the effect of the sizes of crystallites on the formation of the magnetic order. This is corroborated by the appearance of a noticeable magnetization after annealing. Figure 4 shows the σ(T) plots recorded in a magnetic field of H = 80 kA/m for states obtained by the recrystallization of the nanocrystalline sample in a vacuum of 1.33×10^{-2} Pa at temperatures (*1*) 623 and (*2*) 673 K for 2 h and at a temperature of (*3*) 773 K for 30 min. As is seen, the dip observed in the sample with the coarse-crystalline structure is absent in line *1*. This absence indicates that structural phase transitions are absent in this state. However, the existence of magnetization shows that the formation of the ferromagnetic order begins in this state. We emphasize that the annealing of the nanocrystalline sample at temperatures lower than 623 K does not lead to the appearance of ferromagnetic properties. Line *2* exhibits an increase in magnetization with temperature and a maximum at a temperature of 278 K, which is observed near the dip bottom for the coarse-crystalline sample. A decrease in magnetization to zero, which is typical for the given samples, is observed above 278 K. This maximum becomes more pronounced in line *3*, and it is observed at a temperature of 283 K. The temperatures of maxima

approximately correspond to the finish temperature of the martensite–austenite structural transformations. The above discussion provides the conclusion that, upon annealing above 673 K, the size of crystallites increases and their structure is improved so that the formation of the martensitic phase in them becomes possible. The conclusion that the appearance of the maximum in lines *2* and *3* is associated with the beginning of the recovery of the martensite–austenite transformation is indirectly corroborated by the fact that maxima are not observed in measurements of $\sigma(T)$ in stronger magnetic fields (above 200 kA/m). An increase in the temperatures of the structural transitions with an increase in the annealing temperature can be explained by the effect of the sizes of crystallites. As is known, the interface between martensite and austenite phases upon transition moves due to the motion of transformation dislocations, which are atomic-size martensitic steps at interfaces. The temperature of the martensitic transformation must depend on the size of grains, because the grain boundaries are obstacles for the motion of the dislocations and restrict their free path [14]. We note that, even after annealing at 773 K, the modulation structural transition does not return, which is likely due to an insufficient degree of ordering of the compound under investigation upon this thermal treatment.

Thus, it has been shown that the dependence $\sigma(T)$ in the $Ni_{2.14}Mn_{0.81}Fe_{0.05}Ga$ alloy in the coarse-crystalline state is complex, which is attributed to the magnetic and structural transitions occurring in it. This alloy becomes nonferromagnetic in the nanocrystalline state. This effect indicates that the structural order is of special importance upon the formation of the ferromagnetic order in it. In particular, the saturation magnetization in the nanocrystalline nickel is lower than that in the coarse-crystalline state by 30% [3]. In addition, the structural phase transitions (martensitic and modulation) in the $Ni_{2.14}Mn_{0.81}Fe_{0.05}Ga$ nanocrystalline alloy are not observed in the temperature range under consideration.

It is also found that the annealing of the nanocrystalline sample of the $Ni_{2.14}Mn_{0.81}Fe_{0.05}Ga$ alloy at a temperature of 623 K recovers its ferromagnetic properties. The recovery of the martensitic phase transformation begins only after the annealing of the nanocrystalline sample at a temperature of 673 K. After annealing at 773 K, this transformation is more pronounced. The fact that the magnetic order occurs earlier upon annealing can be explained as follows. The magnetic order in the Ni_2MnGa alloys is associated with the exchange interaction between ions responsible for magnetism. It is known that Mn ions make the largest contribution to the magnetic moment of this compound, whereas the contribution from Ni ions is smaller by at least one order of magnitude. It can be assumed that only a certain degree of ordering of only these ions is enough for recovering the ferromagnetic order. The recovery of the structural transition requires a higher degree of ordering of all types of atoms in the crystal cell and, therefore, more effective annealing.

In conclusion, the results of this work show that it is promising to search for processes in which the structure of a material is modified and its strength and plasticity increase simultaneously with the conservation and improvement of its functional capabilities associated with the martensitic and thermoelastic transformations.

ACKNOWLEDGMENTS

We are grateful to V.G. Pushin for discussion of the work and to V.V. Khovaĭlo for placing the initial samples at our disposal. This work was supported by the Russian Foundation for Basic Research (project nos. 03-02-17443, 03-02-39006, and 04-02-81058) and the Ministry of Education of the Russian Federation (project no. 202.01.01.054).

REFERENCES

1. A. I. Gusev and A. A. Rempel, *Nanocrystalline Materials* (Fizmatlit, Moscow, 2000; Cambridge International Science Publishing, Cambridge, 2004).
2. Kh. Ya. Mulyukov, G. F. Korznikova, and S. A. Nikitin, J. Appl. Phys. **79** (11), 8584 (1996).
3. R. Z. Valiev, G. F. Korznikova, Kh. Ya. Mulyukov, *et al.*, Philos. Mag. B **75** (7), 803 (1997).
4. V. G. Pushin, V. V. Stolyarov, R. Z. Valiev, *et al.*, Phys. Met. Metallogr. **94** (Suppl. 1), 54 (2002).
5. V. G. Pushin, V. V. Stolyarov, R. Z. Valiev, *et al.*, Ann. Chim. Sci. Mater. **27** (1), 77 (2002).
6. A. N. Vasilev, A. D. Bozhko, V. V. Khovailo, *et al.*, Phys. Rev. B **59** (2), 1113 (1999).
7. I. E. Dikshteĭn, D. I. Ermakov, V. V. Koledov, *et al.*, Pis'ma Zh. Éksp. Teor. Fiz. **72** (7), 536 (2000) [JETP Lett. **72**, 373 (2000)].
8. A. A. Cherechukin, I. E. Dikshtein, D. I. Ermakov, *et al.*, Phys. Lett. A **291**, 175 (2001).
9. R. O'Handley, *Modern Magnetic Materials: Principles and Applications* (Wiley, New York, 2000).
10. Kh. Ya. Mulyukov, I. Z. Sharipov, and S. S. Absalyamov, Prib. Tekh. Éksp., No. 3, 149 (1998).
11. W. H. Wang, G. H. Wu, J. L. Chen, *et al.*, Appl. Phys. Lett. **79** (8), 1148 (2001).
12. S.-Y. Chu, R. Gallaher, M. De Graef, and M. E. McHenry, IEEE Trans. Magn. **37** (4), 2666 (2001).
13. I. Z. Sharipov, R. R. Mulyukov, and Kh. Ya. Mulyukov, Fiz. Met. Metalloved. **95** (1), 47 (2003).
14. G. A. Malygin, Fiz. Tverd. Tela **42** (8), 1469 (2000) [Phys. Solid State **42**, 1512 (2000)].

Translated by R. Tyapaev

Doklady Physics, Vol. 50, No. 1, 2005, pp. 3–6. Translated from Doklady Akademii Nauk, Vol. 400, No. 1, 2005, pp. 37–40.

PHYSICS

Effect of a High-Entropy Layer on Heat Transfer in the Region of the Incidence of an Oblique Shock Wave on a Blunted-Plate Surface

V. Ya. Borovoĭ[1], I. V. Egorov[2], A. S. Skuratov[3], and I. V. Struminskaya[3]

Presented by Academician G.G. Chernyĭ July 5, 2004

Received July 8, 2004

Investigations of the interaction of an oblique shock wave with a boundary layer began in the late 1950s, although this phenomenon had been discovered much earlier. For a long time (until the 1980s), attention was focused on 2D flows [1–8]. The interference of a boundary layer with an oblique shock wave incident from outside, as well as with shock waves formed in the compression angle and upstream of a step, has been studied. The basic features and properties of a flow at the separation point formed under the action of a strong shock wave have been revealed. In particular, it has been shown that, for "free" interaction, the characteristics of the flow upstream of the separation region and at its beginning are independent of the type of perturbations initiating separation. The relation of the pressures at the separation point and in the plateau region to the Mach and Reynolds numbers has been found experimentally and theoretically. Investigations of heat transfer under 2D interaction (see, e.g., the review in [9]) show that the heat-transfer coefficient increases abruptly at the end of the separation region induced by the shock wave and the "peak" of the heat flux is formed. The correlation formulas obtained describe the maximum heat-transfer coefficient for laminar and turbulent flows as a function of the flow parameters and shock-wave intensity. Beginning with the 1990s, researchers focused their attention on experimental and numerical studies of simple three-dimensional flows, e.g., near sharp wedges placed on a plate. Both free and forced interactions are taken into account.

In almost all of the above works, the interaction of the shock wave with the boundary layer of the sharp body was considered. On the one hand, the leading edges of the construction elements of a hypersonic aircraft (e.g., air-inlet cowl) must have a certain blunting for the reduction of both the heat flow to the leading edge and its maximum temperature. On the other hand, the blunting radius of the leading edge should be limited in order to avoid worsening of the aerodynamic characteristics of the aircraft.

In this work, the flow in the region of the incidence of the shock wave on sharp and blunted plates is analyzed experimentally and numerically on the basis of 2D equations of motion of a viscous gas for Mach numbers M = 6, 8, and 10 and Reynolds numbers $\mathrm{Re}_L = (0.2–1.3) \times 10^6$. An undisturbed boundary layer is in the laminar state, and the flow becomes turbulent in the interference region. It has been found that the formation of a high-entropy layer with decreased gas density downstream of the blunted edge leads to a considerable reduction of the maximum heat transfer in the interference region. This heat entropy effect is enhanced as the Mach number increases. At the same time, it has been shown that the blunting value virtually does not affect the discovered effect if the blunting radius is larger than the displacement thickness of the undisturbed boundary layer.

The model under consideration (Fig. 1) is a plate 120 mm long and 150 mm in width. An oblique shock wave generated by a sharp wedge is incident on the plate. In experiments, variable parameters were the blunting radius of the leading edge (r = 1, 2, 4, and 10 mm), the apex angle of the shock-wave generator wedge ($\theta = 10°$, 15°, and 20°), and the distance of the incident shock wave from the leading edge of the plate X_I. Experiments were carried out in a UT-1M TsAGI setup, which is a short-term Ludwieg-type wind tunnel (steady-flow duration is 40 ms). The heat flow was measured by the thin-wall method with the use of thermocouple sensors with a sufficiently high spatial resolution.

The laminar flow is numerically simulated by solving the 2D system of Navier–Stokes equations. The laminar–turbulent flow is analyzed by applying Reynolds equations with the use of the Boussinesq hypothesis on the Reynolds stresses and the differential

Zhukovskiĭ Central Institute of Aerohydrodynamics, ul. Zhukovskogo 1, Zhukovskiĭ, Moscow oblast, 140180 Russia

[1] *e-mail: volf-borovoy@mtu.ru*

[2] *e-mail: cfd@tsagi.ru*

[3] *e-mail: vgor@tsagi.ru*

1028-3358/05/5001-0003$26.00

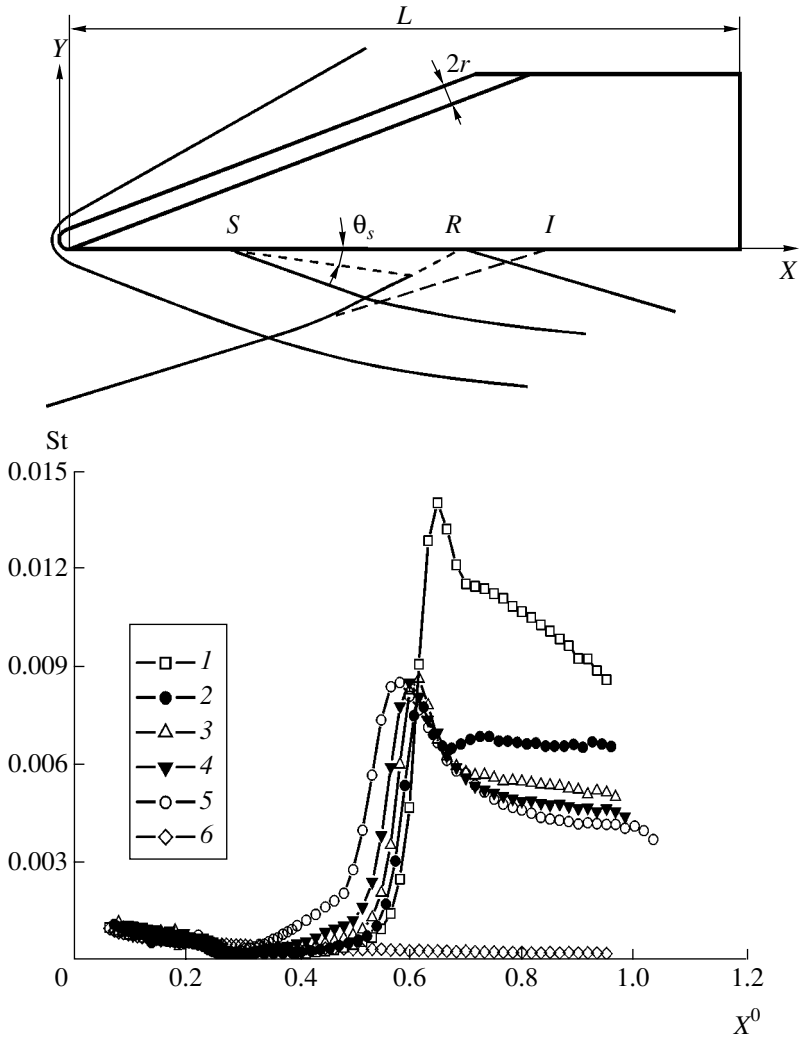

Fig. 1. Layout of the model (*S* is the separation point and *R* is the reattachment point) and the effect of the blunting radius on the Stanton-number distribution over the plate length $\left(X^0 = \frac{X}{L}\right)$ for a Mach number of M = 6 and a Reynolds number of $\mathrm{Re}_L = 1.26 \times 10^6$ [with a shock wave, $\theta = 15°$, r = (*1*) 0, (*2*) 1, (*3*) 2, (*4*) 4, and (*5*) 10 mm; without a shock wave, r = (*6*) 0].

q–ω model of turbulence [10]. The steady-flow solution was obtained as a limiting case for $t \longrightarrow \infty$ (time-dependent method). The differential equations were approximated by an algebraic system of finite difference equations of the second order of accuracy. The system of the nonlinear finite difference equations was solved by the modified Newton method. The numerical-analysis technique for the 2D Navier–Stokes and Reynolds equations in application to supersonic flows of a perfect gas was developed in [11] and in more recent works by the same authors.

Heat transfer on the isolated plate, i.e., in the absence of the incident shock wave, is analyzed first. Measurements of the heat flow on the sharp plate for a Mach number of M = 6 and large Reynolds numbers nearly coincide (standard deviation is 6%) with calculations in the framework of the theory of the laminar boundary layer. Therefore, the accuracy of measurements is satisfactory. For the Mach numbers M = 8 and 10, the measured heat flow considerably exceeds the calculated values due to the viscous–inviscid hypersonic interaction. Investigation shows that, for weak and moderate interactions limited by the hypersonic-interaction parameter $\bar{\chi} \leq 4$, an increase in the Stanton number (dimensionless heat-transfer coefficient) on the sharp plate is satisfactorily described by the empirical relation

$$\frac{\mathrm{St}}{\mathrm{St}_0} = \left(\frac{P}{P_\infty}\right)^{0.5},$$

where

$$\mathrm{St} = \frac{q}{\rho_\infty u_\infty c_p (T_0 - T_\mathrm{w})},$$

q is the measured heat flow, ρ_∞ and u_∞ are the gas density and undisturbed-flow velocity, c_p is the specific

heat at constant pressure, T_0 is the stagnation temperature, T_w is the wall temperature, St_0 is the Stanton number calculated using boundary layer theory disregarding the viscous–inviscid interaction, and $\frac{P}{P_\infty}$ is the pressure increase factor calculated for weak hypersonic interaction [12].

The blunting of the plate leads to an increase in pressure near the leading edge [13]. At the same time, the gas density downstream of the blunted edge decreases due to an increase in temperature, which approaches the stagnation temperature as the Mach number increases unboundedly. As a result, the blunting of the plate enhances heat transfer near the leading edge [14]. Experiments and numerical simulation show that the blunting of the plate increases the heat-transfer coefficient by a factor of 2 for the flow parameters under investigation. This factor increases when the blunting value, as well as the Mach number, increases and the Reynolds number decreases.

The interaction of the shock wave with the plate surface was studied under the same conditions as a flow around the isolated plate. We investigated free interaction when the flow region undisturbed by the incident shock wave holds near the leading edge of the plate. In all cases under investigation, the shock wave initiated the separation of the laminar boundary layer. At the end of the separation region (near the attachment point), the heat-transfer coefficient is higher than the value in the absence of the incident shock wave by a factor of several tens. The enhancement of heat transfer is caused by an increase in pressure downstream of the incident and reflected shock waves, as well as by the formation of the divergence point and the thinning of the boundary layer near it. Moreover, the comparison of experimental data with numerical-simulation results (Fig. 2) shows that the significant enhancement of heat transfer is caused by the transition of the flow at the end of the separation region from the laminar state to the turbulent one. With allowance for the turbulence of the flow, the numerical-simulation results for the interference flow over the sharp plate satisfactorily agree with the experimental data.

The blunting of the plate significantly reduces the maximum Stanton number St_m in the interference region (by about 35% for M = 6) in contrast to the behavior observed for the flow around the isolated plate. Change in the blunting radius over the wide range barely affects the St_m value (Fig. 1). This result is obtained for large relative blunting radii (for $\frac{r}{\delta^*} \geq 1.1$, where δ^* is the displacement thickness of the undisturbed boundary layer on the sharp plate at the incidence point of the shock wave; $\delta^* \simeq 0.9$ mm in the example under consideration), when the high-entropy layer is weakly mixed with the boundary layer. According to [15], the thickness of the high-entropy layer is much larger than the blunting radius due to the low density of the gas in this layer. Therefore, one can suppose that much smaller blunting values of the leading edge of the plate than those studied in this work will give rise to a decrease in the maximum heat-transfer coefficient in the interference region.

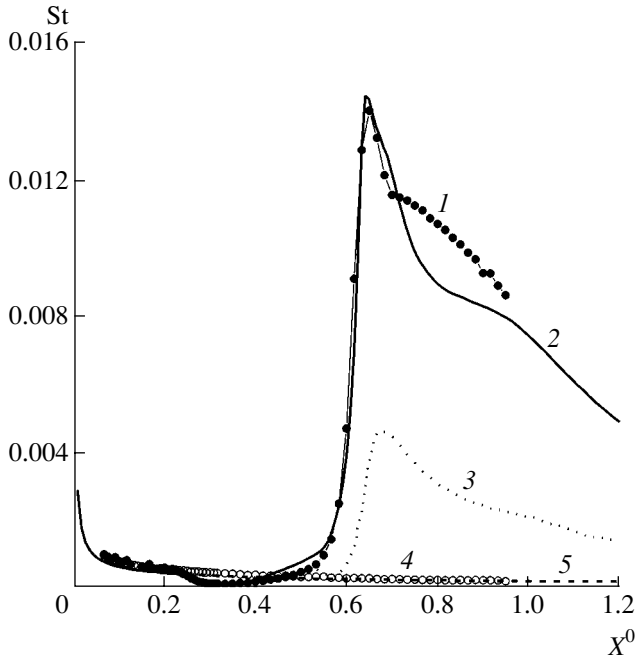

Fig. 2. Stanton-number distribution over the sharp-plate length for a Mach number of M = 6 and a Reynolds number of $Re_L = 1.3 \times 10^6$, $\theta = 15°$: experiment (*1*) with and (*4*) without an incident shock wave and computational fluid dynamics (*2*) including turbulence, (*3*) disregarding turbulence, and (*5*) without a shock wave.

The above effect of the blunting on heat transfer in the interference region is also observed for different Mach numbers. With an increase in the Mach number, the observed effect is enhanced and all features of the flow are more pronounced. As seen in Fig. 3, the blunting of the plate enhances heat transfer upstream of the separation point, as well as on the isolated plate. At the beginning of the separation region, the heat-transfer coefficient on the blunted plate is higher than that on the sharp plate (Fig. 3, M = 10), which is due to an increase in pressure downstream of the bow shock wave generated by blunting. However, blunting reduces the heat-transfer coefficient in the flow-reattachment region. This effect is likely due to the thickening of the mixing layer at the outer boundary of the separation region that is caused by the inclusion of the high-entropy layer into it. In turn, this reduces the velocity gradient and thickening of the boundary layer in the reattachment region. Analysis of the numerical-simulation results corroborates this assumption. Indeed, according to the calculation results, blunting barely affects the pressure in the reattachment region, and it simultaneously increases the mixing-layer thickness in this region.

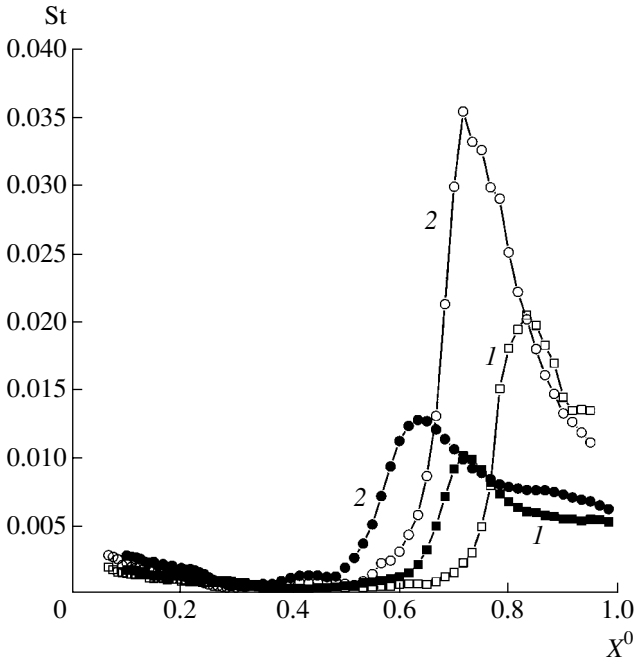

Fig. 3. Stanton-number distribution over the length of the sharp and blunted plates for (*1*) M = 8 and $\mathrm{Re}_L = 0.8 \times 10^6$ and (*2*) M = 10 and $\mathrm{Re}_L = 0.47 \times 10^6$ and r = (open points) 0 and (closed points) 4 mm.

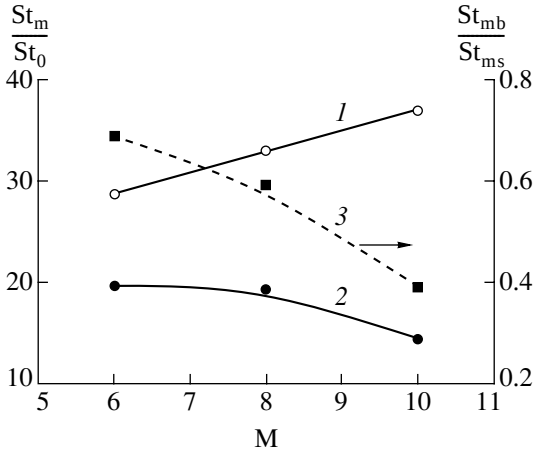

Fig. 4. Mach-number effect on the degree of the maximum enhancement of heat transfer.

Figure 4 shows the maximum Stanton number St_m as a function of the Mach number. With an increase in the Mach number, the ratio $\frac{\mathrm{St}_m}{\mathrm{St}_0}$ increases for the sharp plate (line *1*) and decreases for the blunted plate (line *2*). As a result, the ratio of the maximum Stanton number in the interference region for the blunted plate (St_{mb}) to this value for the sharp plate (St_{ms}) decreases from about 0.65 for M = 6 to 0.4 for M = 10 (line *3*). The enhancement of the blunting effect is caused by an increase in the losses in the total pressure in the bow shock wave with increasing Mach number.

ACKNOWLEDGMENTS

This work was supported by the Russian Foundation for Basic Research (project no. 01-01-00468).

REFERENCES

1. S. M. Bogdonoff and C. E. Kepler, J. Aeronaut. Sci., No. 6, 430 (1955).
2. D. Chapman, D. Kuehn, and H. Larson, NACA Rept., No. 1356, 40 (1958).
3. J. Erdos and A. Pallone, Proc. Heat Transfer and Fluid Mechanics Inst. Stanford: Stanford Univ. Press, 239 (1962).
4. D. M. Bushnell and L. M. Weinstein, J. Spacecr. Rockets **5** (9), 1111 (1968).
5. V. Ya. Neĭland, Izv. Akad. Nauk SSSR, Mekh. Zhidk. Gaza **1** (3), 22 (1970).
6. G. T. Coleman and J. L. Stollery, J. Fluid Mech. **56**, 741 (1972).
7. C. C. Horstman, G. S. Settles, I. E. Vas, *et al.*, AIAA J. **15** (8), 1152 (1977).
8. F. T. Hung, S. N. Greenschlag, and C. A. Scottoline, J. Spacecraft **14** (1), 25 (1977).
9. V. Ya. Borovoĭ, *Gas Flow and Heat Transfer in Regions of Interaction of Shock Waves with the Boundary Layer* (Mashinostroenie, Moscow, 1983) [in Russian].
10. T. J. Coakley and P. G. Huang, AIAA Paper, No. 92-0436 (1993).
11. V. A. Bashkin, I. V. Egorov, M. V. Egorova, and D. V. Ivanov, Izv. Akad. Nauk, Ser. Mekh. Zhidk. Gaza, No. 5, 31 (2000).
12. W. D. Hayes and R. F. Probstein, *Hypersonic Flow Theory* (Academic Press, New York, 1965; Inostrannaya Literatura, Moscow, 1962).
13. G. G. Chernyĭ, *Gas Flows with a High Supersonic Velocity* (Fizmatlit, Moscow, 1959) [in Russian].
14. H. K. Cheng, J. G. Hall, T. C. Golian, and A. Hertzberg, J. Aerosp. Sci. **28** (5), 353 (1961).
15. V. V. Lunev, *Hypersonic Aerodynamics* (Mashinostroenie, Moscow, 1975) [in Russian].

Translated by R. Tyapaev

Doklady Physics, Vol. 50, No. 1, 2005, pp. 32–36. Translated from Doklady Akademii Nauk, Vol. 400, No. 1, 2005, pp. 41–45.

MECHANICS

Free Filtration from Watercourses with Broken Curved Profiles

K. N. Anakhaev

Presented by Academician S.S. Grigoryan June 2, 2004

Received April 19, 2004

In a number of cases, the cross-sectional profiles of watercourses (rivers, canals, water-storage reservoirs, river-bed settlers, etc.) have broken curved shapes formed in the course of the natural evolution of river beds [1] or as a result of a purposeful design approach to natural relief [2]. The water filtration from such watercourses (in the case of deep subsoil waters or the presence of a highly permeable drainage interlayer in the bulk of bottom soil, etc.) is considered to be free. In addition, if the watercourses are rather long, the filtration becomes plane-parallel. As applied to watercourses with smooth curved profiles, this problem was solved previously by the hydromechanical method with the use of the half-inverse technique [3–5]. It should be noted that, in the studies of Vedernikov [4] and Pavlovskiĭ [5], a circular profile shape of a watercourse in the domain of the Joukowski complex was analyzed:

$$\theta = z - iW = (x + \psi) + i(y - \varphi) = \theta_1 + i\theta_2, \quad (1)$$

where $z = x + iy$ is the complex filtration domain with the running coordinates x and y (Fig. 1) and $W = \varphi + i\psi$ is the domain of the reduced complex potential with the coordinates of the pressure-head function φ and the stream function ψ with the specific filtration flow rate Q from a watercourse (Fig. 2g). The values of these functions are taken to be $W = \frac{W_n}{k}$, $\varphi = \frac{\varphi_n}{k}$, $\psi = \frac{\psi_n}{k}$, and $Q = \frac{Q_n}{k}$, where the values marked by the subscript n are real, k is the filtration coefficient of the bottom soil, and

$$\theta_1 = x + \psi, \quad \theta_2 = y - \varphi \quad (2)$$

are the coordinates of the Joukowski complex domain (Fig. 2a).

The above solution makes it possible to find the shape of the smooth curved profile of a watercourse and the values of required parameters for its filtration flow, provided that the width B and the depth H of the watercourse are known.

To evaluate the free filtration from a watercourse with a broken curved profile, we make use of the following conditions in the filtration domain $z = x + iy$ (Fig. 1): (i) the water depth along the watercourse axis (at the point A) is $H = 1$ (in arbitrary units); (ii) the stream function ψ increases from $\psi = -\frac{Q}{2}$ at the point **1** to $\psi = +\frac{Q}{2}$ at the point **2**, and its zero value corresponds to the point A of the watercourse profile, meaning that $\psi_A = 0$; (iii) lines **1**–**4** and **2**–**3** correspond to the left and right depression surfaces of the filtration domain, respectively, whose positions are initially unknown and are found in the course of solving the problem; (iv) the width of the filtration flow between points **3** and **4** (as $y \longrightarrow \infty$) is $B_\infty = Q$, since, in this case, the pressure-head gradient tends to unity; (v) points C and D, which are symmetric with respect to the watercourse axis, are the break points of the watercourse curved profile.

Then, a half-circle with the vertical cut C–A–D in the lower half-plane of the Joukowski complex domain corresponds to the above-described filtration domain **1**–C–A–D–**2**–**3**–**4** (hereinafter, domain **1**–**4**) (Fig. 1). The value S of the cut determines the watercourse profile shape (Fig. 2a). In this case, the points of the domain **1**–**4** correspond to the following parameter values:

$$\begin{gathered}
\textbf{1} \text{ and } \textbf{2}\text{: } x = \pm\frac{B}{2},\ y = 0,\ \psi = \mp\frac{Q}{2},\ \varphi = 0,\\
\theta_1 = \mp\frac{(Q - B)}{2},\ \theta_2 = 0;\\
C \text{ and } D\text{: } x = \pm x_{C(D)},\ y = H + S = 1 + S,\\
\psi = \mp\psi_{C(D)},\quad \varphi = 0,\quad \theta_1 = 0,\quad \theta_2 = 1 + S;\\
A\text{: } x = 0,\ y = H = 1,\quad \psi_A = 0,\ \varphi = 0,\\
\theta_1 = 0,\ \theta_2 = 1;\\
\textbf{3} \text{ and } \textbf{4}\text{: } x = \mp\frac{B_\infty}{2},\ y = \infty,\ \psi = \pm\frac{Q}{2},\ \varphi = \infty,\\
\theta_1 = 0,\ \theta_2 = 0
\end{gathered} \quad (3)$$

Kabardino-Balkariya State Agricultural Academy, ul. Tolstogo 185, Nal'chik, 360004 Russia
e-mail: anaha13@mail.ru

1028-3358/05/5001-0032$26.00

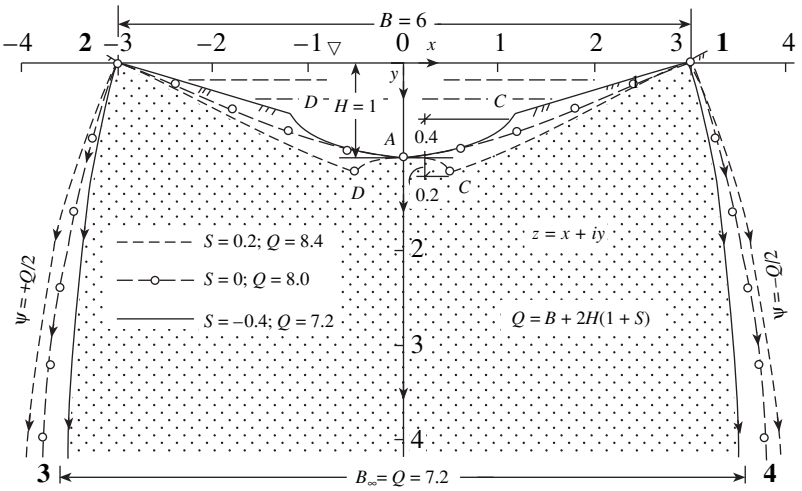

Fig. 1. Free filtration from a watercourse with a broken (smooth) curved profile ($\frac{B}{H}$ = 6; S = –0.4, 0, and 0.2).

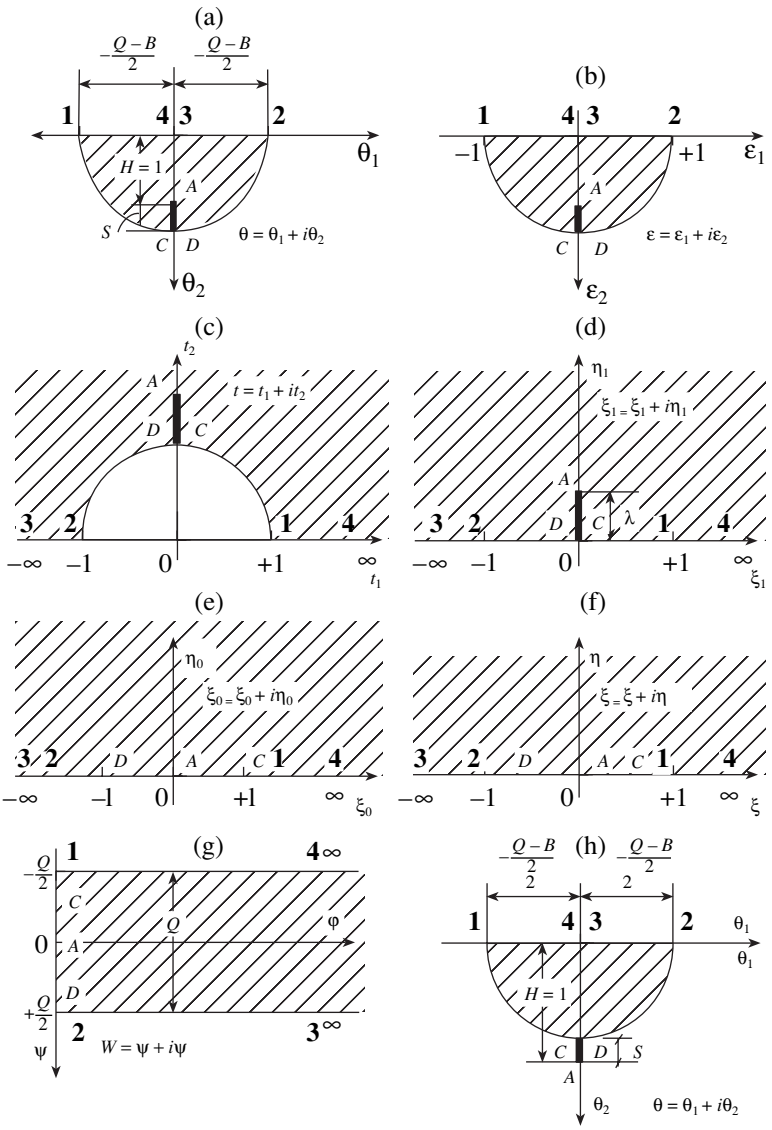

Fig. 2. Sequence of successive conformal mappings of the Joukowski complex domain $\theta = \theta_1 + i\theta_2$ onto the complex-potential domain $W = \varphi + i\psi$.

(the upper and lower signs (plus or minus) relate to the points (**1**, *C*, and **3**) and (**2**, *D*, and **4**), respectively). Within the segments *C–A* and *D–A*, the values of the stream function ψ are equal to the negative values of the *x* coordinates of the points under consideration; i.e., $\psi = -x$.

From the analysis of Fig. 2 and relations (3), it is possible to find the value of the filtration flow rate

$$Q = B + 2H(1 + S), \tag{4}$$

which equals the maximum width of the filtration domain B_∞.

Using the function

$$\varepsilon = \frac{2\theta}{Q - B}, \tag{5}$$

we now conformally map the domain $\theta = \theta_1 + i\theta_2$ onto the similar unit half-circle with the cut *C–A–D* within the domain $\varepsilon = \varepsilon_1 + i\varepsilon_2$ (Fig. 2b). In this case, for the points **1**–**4**, the following correspondence takes place: for the points **1** and **2**, $\varepsilon = \mp 1$; for the points *C* and *D*, $\varepsilon = i$; for the point *A*, $\varepsilon = i\frac{2}{Q - B}$; and for the points **3** and **4**, $\varepsilon = 0$. The upper and lower signs (plus or minus) relate to the points **1** and **2**, respectively.

Furthermore, using the negative-inversion operation

$$t = -\frac{1}{\varepsilon}, \tag{6}$$

we map the domain $\varepsilon = \varepsilon_1 + i\varepsilon_2$ onto the upper half-plane $t = t_1 + it_2$ with the eliminated unit half-circle and cut *C–A–D* (Fig. 2c). Then, the values of parameters in the domain **1**–**4** are $t = \pm 1$ for the points **1** and **2**; $t = i$ for the points *C* and *D*; $t = i\frac{Q - B}{2} = i(1 + S)$ for the point *A*; and $t = \mp\infty$ for the points **3** and **4**. The upper and lower signs (plus or minus) correspond to points (**1**, **3**) and (**2**, **4**), respectively.

Using the Joukowski function

$$\varsigma_1 = 0.5\left(t + \frac{1}{t}\right) \tag{7}$$

and ignoring (see [6]) the cut *C–A–D*, we conformally map the half-plane $t = t_1 + it_2$ with the eliminated unit half-circle onto the upper half-plane $\varsigma_1 = \xi_1 + i\eta_1$ (Fig. 2d). Next, returning to the cut *C–A–D*, we find its position, which, by virtue of symmetry of the problem, coincides with the axis $O\eta_1$. As a result, we have the following results for the points **1**–**4**: $\varsigma_1 = \pm 1$ at the points **1** and **2**; $\varsigma_1 = 0$ at the points *C* and *D*; and $\varsigma_1 = \mp\infty$ at the points **3** and **4**. At the point *A*,

$$\varsigma_1 = i\frac{(Q - B)^2 - 4}{4(Q - B)} = i\frac{S(2 + S)}{2(1 + S)} = i\lambda. \tag{8}$$

The upper and lower signs (plus and minus) relate to the points (**1**, **3**) and (**2**, **4**), respectively.

Using the function [5]

$$\varsigma_0 = \sqrt{\lambda^2 + \varsigma_1^2}, \tag{9}$$

we map the obtained domain $\varsigma_1 = \xi_1 + i\eta_1$ (the upper half-plane with the vertical cut *C–A–D* and with the value λ determined by formula (8)) onto the upper half-plane $\varsigma_0 = \xi_0 + i\eta_0$ (Fig. 2e).

Then, the parameters of the domain **1**–**4** take the following values: $\varsigma_0 = \pm\sqrt{1 + \lambda^2}$ at the points **1** and **2**; $\varsigma_0 = \pm\lambda$ at the points *C* and *D*; $\varsigma_0 = 0$ at the point *A*; and $\varsigma_0 = \mp\infty$ at the points **3** and **4**. The upper and lower signs (plus or minus) relate to the points (**1**, *C*, and **3**) and (**2**, *D*, and **4**), respectively.

Next, using the linear-fractional transformation

$$\varsigma = \frac{\varsigma_0}{\sqrt{1 + \lambda^2}}, \tag{10}$$

we map the domain $\varsigma_0 = \xi_0 + i\eta_0$ onto the similar upper half-plane $\varsigma = \xi + i\eta$ (Fig. 2f) in order to obtain correspondence to the domain **1**–**4**: $\varsigma = \pm 1$ for the points **1** and **2**; $\varsigma = \pm\frac{\lambda}{\sqrt{1 + \lambda^2}}$ for the points *C* and *D*; $\varsigma = 0$ for the point *A*; and $\varsigma = \mp\infty$ for the points **3** and **4** (the upper and lower signs (plus and minus) relate to the points (**1**, *C*, **3**) and (**2**, *D*, **4**), respectively).

Using the function

$$W = \varphi + i\psi = -i\frac{Q}{\pi}\arcsin\varsigma, \tag{11}$$

we map the obtained domain $\varsigma = \xi + i\eta$ onto the horizontal half-strip in the domain of the complex potential $W = \varphi + i\psi$ (Fig. 2g). Then, we have the following values of parameters in the domain **1**–**4**: $W = \mp\frac{iQ}{2}$ at the points **1** and **2**; $W = \mp i\psi_{C(D)}$ at the points *C* and *D*; $W = 0$ at the point *A*; and $W = \infty \pm \frac{iQ}{2}$ at the points **3** and **4** (the upper and lower signs (plus or minus) relate to the points (**1**, *C*, and **3**) and (**2**, *D*, and **4**), respectively).

Substituting the values of ς, ς_0, ς_1, *t*, and ε from expressions (5)–(10) into Eq. (11), we find the interre-

lation between the domains of the Joukowski complex $\theta = \theta_1 + i\theta_2$ and the complex potential $W = \varphi + i\psi$. Separating the real and imaginary parts, we finally arrive at the following relationships:

$$\varphi = \frac{Q}{\pi}\operatorname{arccosh}\frac{M}{2}, \quad \psi = -\frac{Q}{\pi}\arcsin\frac{2\xi}{M}, \tag{12}$$

where

$$M = \sqrt{(1+\xi)^2+\eta^2} + \sqrt{(1-\xi)^2+\eta^2},$$

$$\xi = \frac{\xi_0}{\sqrt{1+\lambda^2}}, \quad \eta = \pm\frac{\eta_0}{\sqrt{1+\lambda^2}},$$

$$\xi_0 = \sqrt{\frac{\sqrt{(\xi_1^2-\eta_1^2+\lambda^2)^2+4\xi_1^2\eta_1^2}+(\xi_1^2-\eta_1^2+\lambda^2)}{2}},$$

$$\eta_0 = \sqrt{\frac{\sqrt{(\xi_1^2-\eta_1^2+\lambda^2)^2+4\xi_1^2\eta_1^2}-(\xi_1^2-\eta_1^2+\lambda^2)}{2}}, \tag{13}$$

$$\xi_1 = \frac{t_1-\varepsilon_1}{2}, \quad \eta_1 = \frac{t_2-\varepsilon_2}{2}, \quad t_1 = -\frac{\varepsilon_1}{\varepsilon_1^2+\varepsilon_2^2},$$

$$t_2 = \frac{\varepsilon_2}{\varepsilon_1^2+\varepsilon_2^2},$$

$$\varepsilon_1 = \frac{\theta_1}{1+S}, \quad \varepsilon_2 = \frac{\theta_2}{1+S}, \quad \lambda = 0.5S\frac{2+S}{1+S}$$

(the upper and lower signs relate to $S \geq 0$ and $S < 0$, respectively).

From relations (13), it follows that, for $\eta = 0$, the quantity M and other parameters take the following values:

$$M = 2,\ \psi = -\frac{Q}{\psi}\arcsin\xi,\ \varphi = 0 \text{ for } |\xi| \leq 1;$$

$$M = 2|\xi|,\ \psi = \mp\frac{Q}{2},\ \varphi = \frac{Q}{\pi}\operatorname{arccosh}|\xi| \text{ for } |\xi| > 1$$

(the upper and lower signs relate to $\xi > 0$ and $\xi < 0$, respectively).

For the given values of B, H, and S, the hydrodynamic solution thus obtained makes it possible to calculate the shape of the broken curved profile of a watercourse and to find the basic parameters of its free filtration flow. In particular, the coordinates of the watercourse profile are found by the following formulas.

Within the segment **1**–C (**2**–D),

$$x = -(1+S)\sqrt{(1+\lambda^2)\sin^2\left(-\frac{\pi\psi}{Q}\right)-\lambda^2} - \psi,$$
$$y = (1+S)\sqrt{(1+\lambda^2)}\cos\frac{\pi\psi}{Q}. \tag{14}$$

For the points C and D,

$$x_{C(D)} = \mp\psi_{C(D)} \text{ and } y_{C(D)} = 1+S.$$

Here, the flow-rate values at the points C and D are

$$\psi_{C(D)} = \mp\frac{Q}{\pi}\arcsin\frac{\lambda}{\sqrt{1+\lambda^2}} \tag{15}$$

(the upper and lower signs relate to the points C and D, respectively).

Within the segment C–A (D–A),

$$x = -\psi,$$
$$y = (1+S)\left[\sqrt{(1+\lambda^2)}\cos\frac{\pi\psi}{Q} \mp \sqrt{\lambda^2-(1+\lambda^2)\sin^2\frac{\pi\psi}{Q}}\right] \tag{16}$$

(the upper and lower signs relate to $S \geq 0$ and $S < 0$, respectively), where the stream function is

$$\psi = \mp\frac{Q}{\pi}\arcsin\xi, \tag{17}$$

and where

$$\xi = \sqrt{\frac{\lambda^2-\eta_1^2}{1+\lambda^2}},$$
$$\eta_1 = \frac{1-\varepsilon_2^2}{2\varepsilon_2} = \frac{1}{2\theta_2}\left[1+S-\frac{\theta_2^2}{1+S}\right]. \tag{18}$$

In Eq. (17), the signs (minus and plus) are used for the sections C–A and D–A, respectively.

Derived analytical dependences (12)–(18) for the values $S > 0$ (internal vertical cut C–A–D, Fig. 2a) provide the solution to the broken curved profile of a watercourse with a concave central part (Fig. 1, $S = 0.2$ and Fig. 3, $S = 0.3$). For $S < 0$ (external vertical slit C–A–D, Fig. 3h), we deal with the solution to the watercourse with a convex central part (Fig. 1, $S = -0.4$ and Fig. 3, $S = -0.4$). In the case when $S = 0$, the above dependences correspond to a watercourse with a smooth curved profile. In particular, the formulas for constructing the profile of such a watercourse take the form

$$x = \sin\frac{\pi\psi}{Q} - \psi, \quad y = \cos\frac{\pi\psi}{Q}, \tag{19}$$

which coincides with the results of the solution obtained by Vedernikov [4] and Pavlovskiĭ [5] for watercourses with a smooth curved profile (Fig. 1, $S = 0$ and Fig. 3, $S = 0$).

It should be noted that, while calculating the broken curved profile of a watercourse, two-sheeted domains in the neighborhoods of points C and D appear, but in much less significant measure than the domains that appear in the course of solving the problem on the

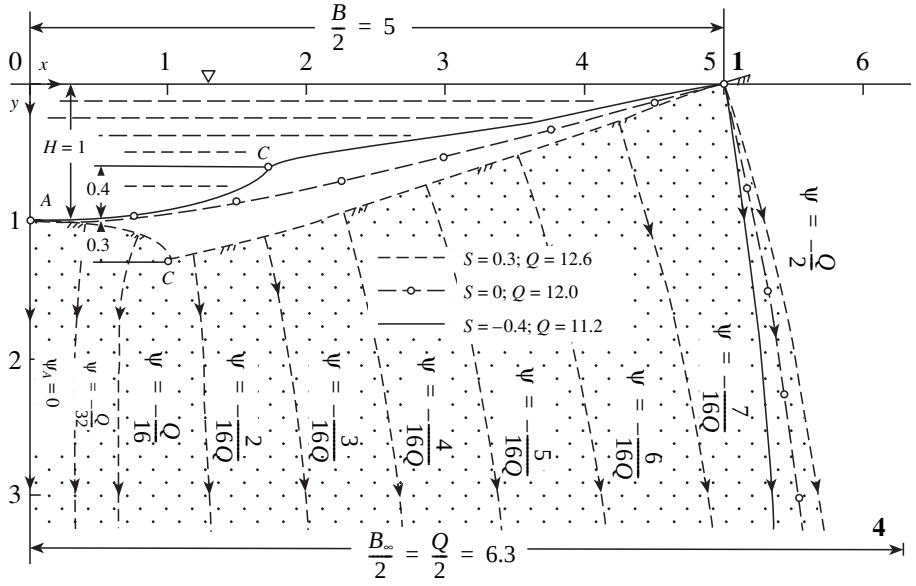

Fig. 3. Profile shapes and filtration from a watercourse with a broken (smooth) curved profile: $\frac{B}{H} = 10$; $S = -0.4$, 0, and 0.3. Only the right-hand part of the cross-sectional cut is shown.

smooth curved profile by the iterative Gersevanov method [7].

The depression surfaces **1**–**4** and **2**–**3** are calculated for the values $\psi = \mp\frac{Q}{2}$, $\theta_2 = 0$, and $\theta_1 = \pm x \mp \frac{Q}{2}$, which are based on the dependence

$$y = \varphi = \frac{Q}{\pi}\operatorname{arccosh}|\xi|, \qquad (20)$$

where

$$\xi = \sqrt{\frac{\xi_1^2 + \lambda^2}{1 + \lambda^2}}, \quad \xi_1 = -\frac{1 + \varepsilon_1^2}{2\varepsilon_1},$$

$$\varepsilon_1 = \frac{\theta_1}{1 + S} = \frac{\pm x \mp Q/2}{1 + S}$$

(the upper and lower signs relate to sections **1**–**4** at $x \geq \frac{B}{2}$ and **2**–**3** at $x \leq -\frac{B}{2}$, respectively).

At $S = 0$, formula (20) enables one to find the positions of the depression surfaces in the particular case of a watercourse with a smooth curved profile (Fig. 1, $S = 0$ and Fig. 3, $S = 0$), which completely coincides with the results of exact solutions obtained in [4, 5].

Figures 1 and 3 show the cross-sectional profiles for broken (smooth) curved watercourses with the corresponding positions of the depression surfaces **1**–**4** and **2**–**3**. The profiles were constructed using the above dependences for $H = 1$, $B = 6$ ($S = -0.4$, 0, and 0.2), and $B = 10$ ($S = -0.4$, 0, and 0.3 for the right-hand part of the watercourse). In the latter case, the streamlines forming flow-rate tapes with equal values of filtration flow rates $\left(\Delta\psi = -\frac{Q}{16}\right)$ are also shown.

The results obtained in this study can be used to calculate filtration from watercourses of different configurations, including the determination of parameters of filtered contaminations from storages of industrial enterprises, etc.

REFERENCES

1. V. S. Lapshenkov, *River-Bed Water Engineering* (NGMA, Novocherkassk, 1999) [in Russian].
2. I. S. Rumyantsev and M. A. Popov, *Environment-Protecting Constructions* (MGUP, Moscow, 2001) [in Russian].
3. J. Kozeny, Wasserkraft und Wasserwiz. **26** (3), 28 (1931).
4. V. V. Vedernikov, *Filtration Theory and Its Application in the Fields of Irrigation and Drainage* (GSI, Moscow, 1939) [in Russian].
5. N. N. Pavlovskiĭ, *Collected Papers*, Vol. 2: *Motion of Subsoil Waters* (Izd. Akad. Nauk SSSR, Moscow, 1956).
6. K. N. Anakhaev, Doctoral Dissertation in Technical Sciences (MGUP, Moscow, 1997).
7. A. R. Tsitskishvili, Prikl. Mat. Mekh. **21** (2), 291 (1957).

Translated by Yu. Vishnyakov

Doklady Physics, Vol. 50, No. 1, 2005, pp. 37–39. Translated from Doklady Akademii Nauk, Vol. 400, No. 1, 2005, pp. 46–48.

MECHANICS

First Integrals in the Problem of the Motion of a Paraboloid of Revolution over a Rough Plane

A. S. Kuleshov

Presented by Academician V.V. Rumyantsev July 8, 2004

Received July 8, 2004

We consider the problem on the motion of a heavy dynamically symmetric rigid body bounded by a contour in the form of a surface of revolution. The body moves without slipping over a fixed horizontal plane. As is well-known, in addition to the energy integral, the equations of motion of a body admit two first integrals that are linear with respect to the quasi-velocities. However, these integrals are obtained in explicit form only for several particular cases [1–3]. In this paper, we present the explicit forms of these integrals for the case when the moving body is a paraboloid of revolution.

MOTION OF A BODY OF REVOLUTION OVER A ROUGH PLANE: FORMULATION OF THE PROBLEM

Let a rigid body symmetric in both its shape and mass distribution with respect to the $G\zeta$ axis that passes through the body's center of gravity G be at rest at a point M on a fixed horizontal plane Oxy. We below use the following notation: θ is an angle between the body's symmetry axis and the vertical; β is an angle between the meridian $M\zeta$ and an arbitrary fixed meridional plane; α is an angle between the horizontal tangent MQ to the meridian $M\zeta$ and the Ox axis. The position of the body is completely determined by the angles α, β, and θ and by the coordinates x and y of the point M.

In addition, we introduce the coordinate system $G\xi\eta\zeta$ moving in both the space and the body so that the $G\xi$ axis permanently lies in the plane of the vertical meridian, whereas the $G\eta$ axis is perpendicular to this plane (see figure). Let the vectors of the velocity $\mathbf{v}$ of the center of mass G, of the body's angular velocity $\boldsymbol{\omega}$, of the angular velocity $\boldsymbol{\Omega}$ of the trihedron $G\xi\eta\zeta$, and the vector $\mathbf{R}$ of the plane reaction be specified in the coordinate system $G\xi\eta\zeta$ by their components v_ξ, v_η, v_ζ; p, q, r; Ω_ξ, Ω_η, Ω_ζ, and R_ξ, R_η, R_ζ, respectively. Let the mass of the body be m, the moment of inertia with respect to the $G\xi$ and $G\eta$ axes be A_1, and the moment of inertia with respect to the symmetry axis be A_3.

We note (see [1–3]) that the distance GQ from the center of gravity of the body to the Oxy plane is a function of angle θ; i.e., $GQ = f(\theta)$. In the coordinate system $G\xi\eta\zeta$, the coordinates ξ, η, and ζ of the point M of body–plane contact are also functions only of angle θ, with $\eta = 0$, and

$$\begin{aligned} \xi &= -f(\theta)\sin\theta - f'(\theta)\cos\theta, \\ \zeta &= -f(\theta)\cos\theta + f'(\theta)\sin\theta. \end{aligned} \tag{1}$$

Since in the body the $G\zeta$ axis is fixed, we have $\Omega_\xi = p$ and $\Omega_\eta = q$. The $G\xi\zeta$ plane is always vertical; therefore, $\Omega_\zeta - \Omega_\xi \cot\theta = 0$. The velocity of the point of contact M is zero; hence,

$$v_\xi + q\zeta = 0, \quad v_\eta + r\xi - p\zeta = 0, \quad v_\zeta - q\xi = 0.$$

After simple transformations, the momentum variation law in the projection onto the $G\eta$ axis and the

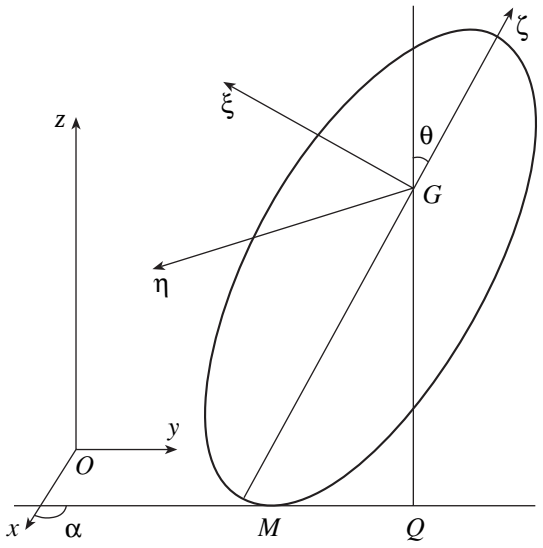

Figure.

Moscow State University,
Vorob'evy gory, Moscow, 119899 Russia

1028-3358/05/5001-0037$26.00

angular-momentum variation law for the $G\xi$ and $G\zeta$ axes yields the following:

$$\frac{d(p\zeta - r\xi)}{dt} - pq(\zeta\cot\theta + \xi) = \frac{R_\eta}{m},$$

$$A_1\frac{dp}{dt} + (A_3 r - A_1 p\cot\theta)q = -\zeta R_\eta, \qquad (2)$$

$$A_3\frac{dr}{dt} = \xi R_\eta.$$

Ignoring further a particular case θ = const and excluding R_η from Eqs. (2), by virtue of $q = -\frac{d\theta}{dt}$, we arrive at

$$\begin{aligned} A_1\frac{dp}{d\theta} + A_3\frac{\zeta}{\xi}\frac{dr}{d\theta} &= -A_1 p\cot\theta + A_3 r, \\ \zeta\frac{dp}{d\theta} - \frac{(A_3 + m\xi^2)}{m\xi}\frac{dr}{d\theta} &= -(\zeta\cot\theta + \xi + \zeta')p + \xi' r. \end{aligned} \qquad (3)$$

Thus, set (3) allows us to determine two first integrals that are linear with respect to p and r. At present, the explicit form of these integrals is known only in the case when a moving body is a nonhomogeneous dynamically symmetric ball. In the case of the motion of a circular disk over a plane, the solution of set (3) yields expressions for the quantities p and r in terms of hypergeometric functions. Below, we present the explicit form of the first integrals linear in p and r for the case of the motion of a paraboloid of revolution over a plane.

FIRST INTEGRALS IN THE CASE OF A PARABOLOID

We now replace the variables p and r in Eqs. (3) by the new variables K_γ^Δ and K_z^Δ. These variables are linked to the variables p and r by the relations

$$K_\gamma^\Delta = (A_1 p\sin\theta + A_3 r\cos\theta)\sqrt{A_1A_3 + A_1 m\xi^2 + A_3 m\zeta^2},$$

$$K_z^\Delta = A_3 r\sqrt{A_1A_3 + A_1 m\xi^2 + A_3 m\zeta^2}.$$

Set (3) written in terms of the new variables K_γ^Δ and K_z^Δ has the form

$$\begin{aligned} \frac{dK_\gamma^\Delta}{d\theta} &= \frac{m(A_3(\xi + \zeta')\cos\theta - (A_3\zeta - A_1\xi')\sin\theta)}{(A_1A_3 + A_1 m\xi^2 + A_3 m\zeta^2)\sin\theta} \\ &\quad\times[\xi K_\gamma^\Delta + (\zeta\sin\theta - \xi\cos\theta)K_z^\Delta], \\ \frac{dK_z^\Delta}{d\theta} &= \frac{mA_3(\xi + \zeta')}{(A_1A_3 + A_1 m\xi^2 + A_3 m\zeta^2)\sin\theta} \\ &\quad\times[\xi K_\gamma^\Delta + (\zeta\sin\theta - \xi\cos\theta)K_z^\Delta]. \end{aligned} \qquad (4)$$

We now assume that the body of revolution moving without slipping over a horizontal plane is a paraboloid. Then,

$$f(\theta) = \frac{\lambda}{\cos\theta}, \quad \xi = -\frac{2\lambda\sin\theta}{\cos\theta}, \quad \zeta = \frac{\lambda\sin^2\theta}{\cos^2\theta} - \lambda,$$

$$\xi^2 = 4\lambda(\zeta + \lambda).$$

With the expressions for ξ and ζ taken into account, we can obtain from Eqs. (4) the following second-order equation for K_γ^Δ:

$$\begin{aligned} &\frac{d^2K_\gamma^\Delta}{d\theta^2} - \frac{2m\lambda^2\sin\theta(2(A_3 - A_1)\cos^2\theta - A_3)}{\Phi(\theta)\cos\theta}\frac{dK_\gamma^\Delta}{d\theta} \\ &- \frac{1 + 3\sin^2\theta}{\sin\theta\cos\theta}\frac{dK_\gamma^\Delta}{d\theta} + \frac{2m\lambda^2(2A_1 - A_3)\sin^2\theta}{\Phi(\theta)}K_\gamma^\Delta = 0. \end{aligned} \qquad (5)$$

Here,

$$\begin{aligned} \Phi(\theta) &= (A_1A_3 + 4m\lambda^2(A_3 - A_1))\cos^4\theta \\ &\quad - 4m\lambda^2(A_3 - A_1)\cos^2\theta + A_3 m\lambda^2. \end{aligned}$$

Instead of the function K_γ^Δ, we now introduce the other function $P(\theta)$ linked to the former by the relation

$$K_\gamma^\Delta = \frac{\sqrt{(A_1A_3 + 4m\lambda^2(A_3 - A_1))\cos^2\theta + 2m\lambda^2(2A_1 - A_3)}}{\cos\theta}P(\theta).$$

For the function $P(\theta)$, we may write out second-order linear differential equation (5) in the form

$$\frac{d^2P}{d\theta^2} - \frac{\frac{d^2S}{d\theta^2}}{\frac{dS}{d\theta}}\frac{dP}{d\theta} + \left(\frac{dS}{d\theta}\right)^2 P = 0, \qquad (6)$$

where the function $S = S(\theta)$ can be represented as the indefinite integral

$$S(\theta) = -\int_0^\theta \frac{m\lambda^2\sqrt{2A_1A_3(2A_1 - A_3)(A_3 + 4m\lambda^2)}\sin\varphi\, d\varphi}{((A_1A_3 + 4m\lambda^2(A_3 - A_1))\cos^2\varphi + 2m\lambda^2(2A_1 - A_3))\sqrt{\Phi(\varphi)}}.$$

Solving Eq. (6), we find

$$P(\theta) = C_1\cos S(\theta) + C_2\sin S(\theta),$$

where C_1 and C_2 are arbitrary constants. Therefore, for the functions K_γ^Δ, the following relationship is valid:

$$K_\gamma^\Delta = \frac{\sqrt{(A_1A_3 + 4m\lambda^2(A_3 - A_1))\cos^2\theta + 2m\lambda^2(2A_1 - A_3)}}{\cos\theta}(C_1\cos S(\theta) + C_2\sin S(\theta)). \quad (7)$$

After the expressions for the function K_γ^Δ depending on the variable θ and arbitrary constants have been derived, we can obtain on the basis of set (4) the expressions for the function K_z^Δ:

$$\begin{aligned} K_z^\Delta &= \frac{2m\lambda^2A_3\cos 2\theta(\cos^2\theta)^{-1}}{\sqrt{(A_1A_3 + 4m\lambda^2(A_3 - A_1))\cos^2\varphi + 2m\lambda^2(2A_1 - A_3)}}(C_1\cos S(\theta) + C_2\sin S(\theta)) \\ &+ \frac{\sqrt{2A_1A_3(A_3 + 4m\lambda^2)(2A_1 - A_3)^{-1}\Phi(\theta)}}{\cos\theta\sqrt{(A_1A_3 + 4m\lambda^2(A_3 - A_1))\cos^2\theta + 2m\lambda^2(2A_1 - A_3)}}(C_2\cos S(\theta) - C_1\sin S(\theta)). \end{aligned} \quad (8)$$

It is worth noting that, for $A_3 = 2A_1$, it follows from Eq. (5) that K_γ^Δ = const. This is the case that was previously analyzed in [2].

Thus, the first integrals (linear with respect to quasivelocities) of the equations of motion for a heavy paraboloid of revolution that is rolling over a perfectly rough plane can be derived from relationships (7) and (8). In this case, no additional constraints were imposed on the moments of inertia A_1 and A_3. The results of this study are consistent with those obtained in [2] for the particular case $A_3 = 2A_1$.

ACKNOWLEDGMENTS

This work was supported by the Russian Foundation for Basic Research, project no. 04-01-00398, and by the Council of the President of the Russian Federation for Support of Young Russian Scientists and Leading Scientific Schools (project nos. MK-1393.2003.01 and NSh-2000.2003.1).

REFERENCES

1. S. A. Chaplygin, Trudy Otd. Fiz. Nauk Obshchestva Lyubiteleĭ Estestvozn., Antropologii, Étnografii **3**, 10 (1897).
2. Kh. M. Mushtari, Mat. Sb. **39** (1/2), 105 (1932).
3. A. P. Markeev, *Dynamics of a Body Touching a Solid Surface* (Nauka, Moscow, 1992) [in Russian].

Translated by G. Merzon

Doklady Physics, Vol. 50, No. 1, 2005, pp. 40–43. Translated from Doklady Akademii Nauk, Vol. 400, No. 1, 2005, pp. 49–52.

MECHANICS

Fluid Dynamics with Transitions in the Topology of the Flow Domain: Breakup of Jets and Rupture of Films

Yu. D. Shikhmurzaev

Presented by Academician R.I. Nigmatulin June 29, 2004

Received July 14, 2004

The breakup of jets and rupture of liquid films are two typical examples from a wide class of flows, where the topology of the domain occupied by a fluid changes in a finite time. In the case of an axisymmetric liquid thread, the known solutions [1, 2] aimed at describing its breakup are singular and predict unbounded pressures and velocities as breakup is approached. Experimental investigations carried out to verify predictions made on the basis of these solutions, in particular, for the evolution of the thread immediately after its breakup, point out qualitative and quantitative discrepancies between theory and experiment [3, 4]. This situation indicates that, as the topological transition is approached, additional physical effects appear that are not included in the standard formulation of the problem and, to remove the singularities, one has to identify these effects and make a corresponding generalization of the model.

The missing physics can be identified by analyzing the known singular solutions [1, 2] from the viewpoint of their limits of applicability. This analysis shows that, according to these solutions, the local relative rate at which the free-surface area is created tends to infinity as the diameter of the liquid thread goes to zero: to leading order, these solutions describe a plug flow corresponding to the stretching of a liquid cylinder. Since the rate at which the free surface acquires its specific "surface" properties (such as the surface tension) is physically finite, the singular solutions, where the surface tension is assumed to be constant, fall outside their limits of applicability when the characteristic time associated with the creation of fresh free-surface area becomes comparable with the surface-tension-relaxation time. Thus, the breakup of a jet is actually a particular case of a more general physical phenomenon, namely, flows with the formation (and/or disappearance) of interfaces, and to describe it adequately, one can apply, without any *ad hoc* alterations, a theory of such flows developed earlier [5, 6]. This theory was formulated using methods of irreversible thermodynamics and was originally used to simulate processes of dynamic wetting [5–8]. To study a free-surface flow with a topological transition of the flow domain in the framework of this theory, one has to consider those solutions of the Navier–Stokes equations

$$\nabla \cdot \mathbf{u} = 0, \quad \rho\left(\frac{\partial \mathbf{u}}{\partial t} + \mathbf{u} \cdot \nabla \mathbf{u}\right) = -\nabla p + \mu \nabla^2 \mathbf{u}, \quad (1)$$

that satisfy the boundary conditions

$$\frac{\partial f}{\partial t} + \mathbf{v}^s \cdot \nabla f = 0, \quad (2)$$

$$\begin{aligned} -p + \mu \mathbf{n} \cdot [\nabla \mathbf{u} + (\nabla \mathbf{u})^*] \cdot \mathbf{n} &= \sigma \nabla \cdot \mathbf{n}, \\ \mu \mathbf{n} \cdot [\nabla \mathbf{u} + (\nabla \mathbf{u})^*] \cdot (\mathbf{I} - \mathbf{nn}) + \nabla \sigma &= 0, \end{aligned} \quad (3)$$

$$\begin{aligned} \rho(\mathbf{u} - \mathbf{v}^s) \cdot \mathbf{n} &= (\rho^s - \rho_e^s)\tau^{-1}, \\ \frac{\partial \rho^s}{\partial t} + \nabla \cdot (\rho^s \mathbf{v}^s) &= -(\rho^s - \rho_e^s)\tau^{-1}, \end{aligned} \quad (4)$$

$$\begin{aligned} (1 + 4\alpha\beta)\nabla\sigma &= 4\beta(\mathbf{v}^s - \mathbf{u}) \cdot (\mathbf{I} - \mathbf{nn}), \\ \sigma &= a\rho^s - b(\rho^s)^2 \end{aligned} \quad (5)$$

at the *a priori* unknown free surface $f(\mathbf{r}, t) = 0$ with the inward normal $n = \dfrac{\nabla f}{|\nabla f|}$, together with some conditions in the far field specifying a particular flow and initial conditions. In addition to the known kinematic condition given by Eq. (2) and conditions on the normal and tangential stress (Eq. (3)), where $\mathbf{I}$ is the metric tensor, the model takes into account the mass exchange between the bulk and surface phases [Eq. (4)] that is associated with the relaxation of the interface towards its equilibrium state as the surface density ρ^s tends to its equilibrium value ρ_e^s (τ is the relaxation time and $\mathbf{u}$ and $\mathbf{v}^s$ are the bulk and the surface-phase velocity, respec-

School of Mathematics and Statistics, University of Birmingham, Edgbaston, Birmingham, B15 2TT, United Kingdom
e-mail: yulii@for.mat.bham.ac.uk

1028-3358/05/5001-0040$26.00

tively). For spatially nonuniform flows, such as the breakup of a jet, the appearing gradient of the surface tension σ first, influences the flow via the tangential-stress condition (the Marangoni effect, the second of Eqs. (3)) and, second, by forming a torque with the tangential stress, leads to the deviation of the tangent to the interface components of the surface velocity $\mathbf{v}^s$ from the corresponding component of the bulk velocity $\mathbf{u}$ evaluated at the interface (the first of Eqs. (5)). The equation of state in the surface phase (the second of Eqs. (5)) is taken in a simple "barotropic" form, which takes into account that the surface tension decreases from its equilibrium value $\sigma_e = \sigma(\rho_e^s)$ if the surface phase becomes compressed or extremely rarefied; $\rho_e^s \geq \frac{a}{2b}$ for all liquid–gas interfaces studied so far. The dependence of the phenomenological material constants α, β, and τ on viscosity and their estimates for particular fluids have been obtained by analyzing experiments on dynamic wetting [7, 8].

The breakup problem can be considerably simplified by using the slender-jet approximation, where the ratio ε of characteristic length scales in the radial and axial directions is used as a small parameter. If the free-surface shape in the suitably chosen cylindrical coordinates is given by $r = h(z, t)$, and u, u^s, w, and w^s denote the radial and axial components of the bulk and surface velocities, respectively, then the slender-jet approximation can be obtained by using the following asymptotic expansions:

$$r = L\varepsilon^2 r^*, \quad z = L\varepsilon z^*, \quad t = T\varepsilon^2 t^*,$$

$$hL^{-1} = \sum_{n=0}^{\infty} \varepsilon^{2(n+1)} h_n,$$

$$(u, u^s)U^{-1} = \sum_{n=0}^{\infty} \varepsilon^{2n} (u_n, u_n^s),$$

$$(w, w^s)U^{-1} = \sum_{n=0}^{\infty} \varepsilon^{2n-1} (w_n, w_n^s),$$

$$pP^{-1} = \sum_{n=0}^{\infty} \varepsilon^{2(n-1)} p_n,$$

$$(\sigma\sigma_e^{-1}, \rho^s b a^{-1}) = \sum_{n=0}^{\infty} \varepsilon^{2n} (\sigma_n, \rho_n^s) \quad \text{for} \quad \varepsilon \longrightarrow 0,$$

where $L = \mu^2(\rho\sigma_e)^{-1}$, $T = \mu^3\rho^{-1}\sigma_e^{-2}$, $U = \sigma_e\mu^{-1}$, and $P = \rho\sigma_e^2\mu^{-2}$. The equations following from the standard asymptotic analysis can be further simplified for medium- and high-viscosity fluids by using the estimates for material constants of the model obtained from experiments on dynamic wetting [8]. These estimates show that $a\mu(\rho\sigma_e\tau b)^{-1} \ll 1$ and $\beta\mu\rho^{-1}\sigma_e^{-1}(1 + 4\alpha\beta)^{-1} \gg 1$ for such fluids and, hence, to the leading order in ε and in these parameters, one can neglect the difference between the components of the surface-phase velocity (u_0^s, w_0^s) and the corresponding components of the bulk velocity (u_0, w_0).

Then, one arrives at an initial-value problem for the following set of equations:

$$\frac{\partial w}{\partial t} + w\frac{\partial w}{\partial z} = \frac{1}{h^2}\frac{\partial}{\partial z}(h\sigma) + \frac{3}{h^2}\left(h^2\frac{\partial w}{\partial z}\right), \tag{6}$$

$$\frac{\partial F}{\partial t} + w\frac{\partial F}{\partial z} + \frac{F}{2}\frac{\partial w}{\partial z} = 0, \quad F = (h, \rho^s); \qquad \sigma = a\rho^s - b(\rho^s)^2. \tag{7}$$

(Hereinafter, for brevity, we omit the superscript * and the subscript 0, which mark the dimensionless independent variables and the zeroth approximation of the functions, respectively.) The first term on the right-hand side of Eq. (6) describes the combined action of the following two factors: the capillary pressure, $-\frac{\sigma\partial(1/h)}{\partial z}$, and the Marangoni effect due to the surface-tension gradient, $\frac{1}{h}\frac{\partial\sigma}{\partial z}$. If one sets $\sigma = 1$ in Eq. (6), this equation, together with Eq. (7) for $F = h$, forms a closed system studied earlier [1], which leads to singular solutions.

The evolution equations for h and ρ^s turn out to be identical (but initial conditions in the general case are, of course, different), because, with an increase in the rate at which the fresh free-surface area is produced, it eventually becomes much larger than the finite rate ($\sim\tau^{-1}$) at which the interface acquires its surface properties, and the relaxation mechanisms become too slow to restore the equilibrium state of the interface. As a result, in the regime considered here, the surface density evolves entirely due to the change in the geometry of the free surface and, as the radius of the minimum cross-section decreases and the surface area correspondingly increases, the surface density also decreases. According to Eqs. (7), this eventually leads to a decrease in the surface tension, so that the capillary pressure ($\sigma\nabla\cdot\mathbf{n}$) in the minimum cross section remains finite. At the same time, since the surface density decreases proportionally to the radius and, hence, spatially nonuniformly, there appears a surface tension gradient directed away from the plane of the minimum cross section. This gradient tends to pinch off the thread by pulling the fluid out of the minimum cross section due to the Marangoni effect. Thus, in the present model,

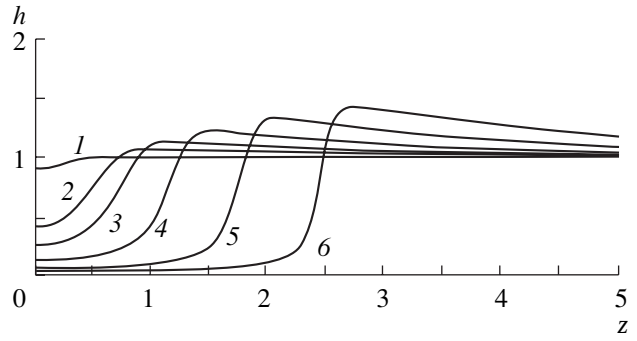

Fig. 1. Free-surface profiles for t = (*1*) 0, (*2*) 10, (*3*) 11, (*4*) 12, (*5*) 13, and (*6*) 14.

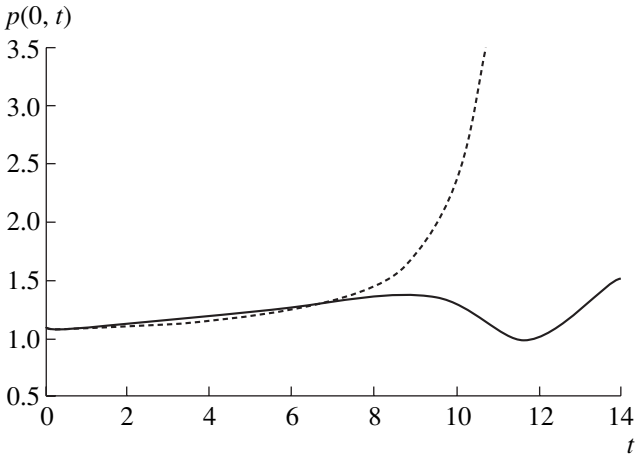

Fig. 2. Time dependence of the pressure in the minimum cross section as obtained using (solid line) the present theory and (dashed line) the standard model ($\sigma = 1$).

the breakup of a jet appears as a result of the combined action of a finite capillary pressure and a finite surface-tension gradient, unlike the scenario proposed by the singular solutions [1, 2], where the capillary pressure, pressure in the liquid, and the axial velocity tend to infinity.

The breakup mechanism described above is illustrated in Figs. 1 and 2 obtained by numerically solving Eqs. (6) and (7) for a model disturbance of the free surface (Fig. 1, curve *1*) and $\rho^s(z, 0) \equiv \rho_e^s$ (the dimensionless value of ρ_e^s is set to be 0.6). As the breakup is approached, one can see the formation of a distinct structure consisting of a recoiling tip of the main thread and a vanishing "residual" filament. In the latter, the surface tension decreases to zero proportionally to its radius. As shown in Fig. 2, the formation of this structure corresponds to a characteristic phase in the evolution of the pressure in the minimum cross section, where the pressure passes through a local minimum. Then, the pressure increases again but its limiting value is finite, as one can demonstrate analytically by examining a locally self-similar solution for Eqs. (6) and (7) in the following variables:

$$t' = \delta^2 t, \quad z' = \delta^2 z, \quad (h, \rho^s, \sigma) = \sum_{n=0}^{\infty} \delta^{n+1}(h_n, \rho_n^s, \sigma_n),$$

$$w = \sum_{n=0}^{\infty} \delta^n w_n \quad \text{for} \quad \delta \longrightarrow 0.$$

This limit is considered within the short-time limit $\varepsilon \longrightarrow 0$ ($\varepsilon\delta^{-3} \longrightarrow 0$ as $\varepsilon \longrightarrow 0$, $\delta \longrightarrow 0$), so that, physically, the breakup takes place on a time scale that is small compared with τ. The locally self-similar solution also gives that, to leading order, the recoiling ends of the macroscopic thread no longer affect each other and behave as if the breakup has already taken place (though it takes some time after the formation of the "residual" thread before it finally disappears).

Since, according to independent experiments [7, 8], the surface-tension-relaxation time is proportional to the viscosity of the fluid, $\tau \backsim \mu$, one can explain why, for chemically similar fluids with viscosities varying in a wide range, the minimum diameter of a liquid thread observed in experiments before the breakup is viscosity-independent [3]. Indeed, the breakup mechanism described above is triggered when the relative rate of change in the free-surface area obtained using the standard model becomes comparable with τ^{-1}. By considering the dimensional form of the singular solution [1], one can show that this corresponds to the thread thickness in the minimum cross section independent of viscosity.

The developed approach allows one to unify the mathematical description of different fluid motions with topological changes of the flow domain without introducing any *ad hoc* alterations of the model. This can be demonstrated by considering, as an example, the rupture of free films or films on a solid substrate. Since the capillary pressure is always a restoring force in this case, in the approaches known in the literature (e.g., [9]), the topological transition is ensured by explicitly incorporating (singular) intermolecular forces into a model formulated in the framework of continuum mechanics. The corresponding terms added to the Navier–Stokes equations play the same role as the capillary pressure does in the case of a cylindrical jet: they increase the amplitude of initial disturbances of the free surface, bringing together the opposite boundaries.

The present model given by Eqs. (1)–(5) and applied to the free-film rupture problem can be analyzed, asymptotically in the thin-film approximation and/or numerically, in the same way as that described above. The results show that, in the thin-film approximation, to leading order, the capillary pressure does not appear, so that the film rupture is driven entirely by the Marangoni effect. This effect is triggered by external disturbances

of the free surface when the relative rate of creation of a fresh free-surface area becomes comparable with τ^{-1}. Then, the film ruptures if it is thin enough, so that the Marangoni stresses can break it before the relaxation mechanisms driving the free surface back to its equilibrium state eliminate these stresses. Otherwise, the surface tension relaxes to its equilibrium value and the capillary pressure, becoming the only driving force, restores the initial shape of the free surface. As a result, the magnitude and speed of external disturbances correlate with the maximum thickness of the film that can be ruptured by these disturbances. This situation is qualitatively different from the case of a cylindrical thread, which, due to capillary effects, is linearly unstable to long-wave disturbances [10].

REFERENCES

1. J. Eggers, Phys. Rev. Lett. **71**, 3458 (1993).
2. D. T. Papageorgiou, Phys. Fluids **7**, 1529 (1995).
3. T. A. Kowalewski, Fluid. Dyn. Res. **17**, 121 (1996).
4. D. M. Henderson, W. G. Pritchard, and L. B. Smolka, Phys. Fluids **9**, 3188 (1997).
5. Yu. D. Shikhmurzaev, Dokl. Akad. Nauk SSSR **321**, 44 (1991) [Sov. Phys. Dokl. **36**, 749 (1991)].
6. Yu. D. Shikhmurzaev, Int. J. Multiphase Flow **19**, 589 (1993).
7. Yu. D. Shikhmurzaev, Phys. Fluids **9**, 266 (1997).
8. T. D. Blake and Y. D. Shikhmurzaev, J. Coll. Interface Sci. **253**, 196 (2002).
9. W. W. Zhang and J. R. Lister, Phys. Fluids **11**, 2454 (1999).
10. Lord Rayleigh, Philos. Mag. **34**, 177 (1872).

Translated by Yu. Shikhmurzaev

Doklady Physics, Vol. 50, No. 1, 2005, pp. 44–48. Translated from Doklady Akademii Nauk, Vol. 400, No. 2, 2005, pp. 192–196.

MECHANICS

Investigation of Coupled Boundary Value Problems of Continuum Mechanics and Mathematical Physics

Academician V. A. Babeshko and O. M. Babeshko

Received August 18, 2004

We present a method of studying coupled boundary value problems for systems of linear partial differential equations of arbitrary finite order with constant coefficients in arbitrary convex domains. New relations for solutions of such boundary value problems are derived. These relations enable one to separate and analyze the effect of the parameters of boundary value problems on the behavior of solutions. The approach represents a fragment of a mathematical technique for studying stresses in lithospheric plates in seismology, when it is necessary to simultaneously take into account how a solution is affected by numerous physical parameters of fields described by boundary value problems, as well as the geometric parameters of the definition domains of boundary value problems.

In [1–4], the method was demonstrated for most frequently applied systems of boundary value problems for second-order partial differential equations. The topological approach used for these aims makes it possible to derive exact relations for describing solutions in terms of convenient formulations of boundary value problems. In contrast to numerous variants of the boundary-element method, fundamental solutions, variational numerical methods, and methods of finite difference approximations, the method proposed in this work has several undeniable advantages, conceding, perhaps, in simplicity. Among these advantages are

(i) the absence of the requirement of *a priori* solvability of a problem,

(ii) independence from the type (bounded, semibounded, or unbounded) of domain,

(iii) explicit expansion of the solution in terms of the basis elements, where the parameters of the expansion are determined by the solutions of pseudodifferential equations.

In view of these circumstances, the method is the same research method in arbitrary multidimensional domains as that of systems of ordinary differential equations on a segment. It has numerous applications in boundary value problems for continuum media in various fields.

1. Any system of linear partial differential equations with constant coefficients or one partial differential equation with constant coefficients of an arbitrary finite order can be reduced to the system of first-order linear partial differential equations. This reduction is achieved by introducing new variables that are the derivatives of the initial variables, which leads to the reduction of the differentiation order in equations with a simultaneous increase in the number of unknowns. Supposing that the described transformations are made, we consider a boundary value problem for the following system of first-order partial differential equations with constant coefficients in a convex domain Ω with the smooth boundary $\partial\Omega$:

$$\sum_{m=1}^{N}\sum_{p=1}^{3}\left(\alpha_{nmp}\frac{\partial}{\partial x_p}+\alpha_{nm}\right)\varphi_m(\mathbf{x}) = g_n(\mathbf{x}),\ \mathbf{x}\in\Omega,$$
$$\boldsymbol{\varphi} = \{\varphi_m\},\ \varphi(\mathbf{x}) = \varphi(x_1, x_2, x_3),\ n = 1, 2, \ldots, N, \tag{1}$$
$$\mathbf{x} = \{x_1, x_2, x_3\}.$$

After transformations, the number of boundary conditions, whose order is not higher than the first, increases. We assume that they have the form (derivatives appearing in the boundary conditions are replaced by new unknowns)

$$\sum_{m=1}^{M}\sum_{p=1}^{3}\left(b_{smp}\frac{\partial}{\partial x_p}+b_{sm}\right)\varphi_m(\mathbf{x}) = g_{0,s}(\mathbf{x}),\quad \mathbf{x}\in\partial\Omega, \tag{2}$$

where

$$s = 1, 2, \ldots, M,\quad M\le N,\ \mathbf{g} = \{g_n\},\ \mathbf{g}_0 = \{g_{0,n}\}.$$

The solution $\boldsymbol{\varphi} = \{\varphi_m\}$ and specified functions are assumed to belong to certain spaces $\mathbf{H}_p$ introduced in [1–4]. The notation accepted in those works will be used below. As in those works, it is assumed that the topology introduced is induced by the Euclidean metric of the initial coordinate system.

The above relations can be treated as a differentiable mapping of the vector field $\boldsymbol{\varphi}$ specified on the orient-

Kuban State University,
ul. Karla Libknekhta 149, Krasnodar, 350640 Russia
e-mail: babeshko@kubsu.ru

1028-3358/05/5001-0044$26.00

able manifold with the boundary $M^3 \equiv (\Omega \cup \partial\Omega)$ to the vector field specified by the right-hand side of Eq. (1) and considered on the same manifold M^3. The mapping is realized by a differential expression described by the left-hand sides of the above relations.

Thus, the linear differential mapping specifies the transformation of the vector field $\boldsymbol{\varphi}$ given on M^3 to the vector field $\mathbf{g} + \mathbf{g}_0$ on M^3, i.e., the automorphism of M^3 into itself. It is necessary to reconstruct the vector field $\boldsymbol{\varphi}$. The mapping is associated with a certain, generally irreducible, three-parametric group of transformations of M^3 into itself. Subjecting the transformation to the above automorphism, we obtain necessary relations for a local representation of the indicated group of transformations. When the domain Ω is simple—e.g., a layer, a sphere, a cylinder—the global representation of the group can be constructed.

We introduce a vector $\boldsymbol{\omega}$ whose components are the external forms

$$\boldsymbol{\omega} = \{\omega_m\}, \quad n = 1, 2, \ldots, N,$$

$$\omega_n = -\sum_{m=1}^{N}\sum_{p=1}^{3} a_{nmp}\varphi_m e^{i\langle\boldsymbol{\alpha}\mathbf{x}\rangle} dx_{p-1} \wedge dx_{p+1}, \tag{3}$$

$$\boldsymbol{\varphi} = \{\varphi_n\}, \quad \boldsymbol{\Phi} = \{\Phi_n\}, \quad \boldsymbol{\alpha} = \{\alpha_1, \alpha_2, \alpha_3\},$$

$$G_n(\boldsymbol{\alpha}) = \iiint_{\Omega} g_n(\mathbf{x}) e^{i\langle\boldsymbol{\alpha}\mathbf{x}\rangle} d\mathbf{x} \equiv Fg_n, \quad \Phi_m = F\varphi_m.$$

Here, $x_0 = x_3$ and $x_4 = x_1$.

Using the transformations presented in [1–4], relation (1) can be represented in the equivalent form

$$\sum_{m=1}^{N} k_{nm}(\boldsymbol{\alpha})\Phi_m(\boldsymbol{\alpha}) = -G_n(\boldsymbol{\alpha}) + \iint_{\partial\Omega} \omega_n(\boldsymbol{\alpha}),$$

$$\mathbf{K}(\boldsymbol{\alpha}) = \|k_{nm}(\boldsymbol{\alpha})\|,$$

$$\omega_n = \sum_{m=1}^{N} \varphi_m e^{i\langle\boldsymbol{\alpha}\mathbf{x}\rangle} (\alpha_{nm1} dx_2 \wedge dx_3 - \alpha_{nm2} dx_1 \wedge dx_3 + \alpha_{nm3} dx_1 \wedge dx_2),$$

$$k_{nm}(\alpha) = \sum_{p=1}^{3} (a_{nmp} \cdot i\alpha_p - a_{nm}).$$

Thus, this system can be written in the vector form

$$\mathbf{K}\boldsymbol{\Phi} = -\mathbf{G}(\alpha) + \iint_{\partial\Omega} \omega. \tag{4}$$

2. We will assume below that the parameters α_1 and α_2 are on the real axis and α_3 varies in the complex plane. We suppose that the matrix function $\mathbf{K}(\alpha)$ is not triangular or diagonal, and it is not reduced to such matrices by a matrix with constant coefficients. Otherwise, such matrix functions are simply factorized by the known formulas.

Let us factorize the matrix functions $\mathbf{K}(\alpha)$ with respect to the parameter α_3 by the factorization formulas [5] in the form

$$\mathbf{K}(\alpha_3) = \mathbf{K}_+(\alpha_3)\mathbf{K}_-(\alpha_3), \quad K(\alpha_3) = K_+(\alpha_3)K_+(\alpha_3),$$

$$K(\alpha_3) = \det\mathbf{K}(\alpha_3), \quad K_\pm(\alpha_3) = \det\mathbf{K}_\pm(\alpha_3).$$

Here, λ_+ and λ_- are the upper and lower half-planes, respectively.

However, in contrast to [5], we first construct the elements of the matrix function $\mathbf{K}_+(\alpha)$ rather than the elements of the matrix function $\mathbf{K}_-(\alpha)$. Using the approach proposed in [5], we obtain the matrix function inverse to the matrix function $\mathbf{K}_+(\alpha)$ in the form

$$\mathbf{K}_+^{-1} = \begin{vmatrix} 1 & 0 & \ldots & 0 & \ldots & 0 \\ S_{m1} & S_{m2} & \ldots & S_{mm} & \ldots & S_{mN} \\ 0 & 0 & \ldots & 0 & \ldots & 0 \end{vmatrix}.$$

Only the diagonal elements and elements of the mth row of this matrix function are nonzero. All other elements are identically equal to zero:

$$S_{mp} = \frac{1}{2\pi i}\int_{C_m}\sum_{s=1}^{N} \frac{Q_{ps}(m, z)K_{ms}(z)dz}{Q_m(z)K_+(z)(z-\alpha_3)}, \quad \alpha_3 \in \lambda_-,$$

$$S_{mm} = K_+^{-1}(\alpha_3).$$

Here, $Q_m^{-1}(z)Q_{ps}(m, z)$ are the elements of the $(N-1)$-order matrix function inverse to the matrix function obtained from the matrix conjugate to the matrix $\mathbf{K}$, where the mth row and column are removed. It is assumed that the determinant of this matrix $Q_m(z)$ has no common zeros with the function $K_+(z)$.

We use the unity decomposition in the integrals entering into the right-hand side of Eq. (3); i.e., we represent

$$\iint_{\partial\Omega} \boldsymbol{\omega} = \iint_{\partial\Omega}\sum_{\sigma} \varepsilon_\sigma \boldsymbol{\omega}, \quad \sum_{\sigma} \varepsilon_\sigma = 1.$$

Applying the method developed in [4, 5], we pass in Eq. (3) to the tangent bundle on $\partial\Omega$. Taking certain fixed points of the decomposition-projection domains on $\partial\Omega$ with allowance for the orientability of surfaces

as the base of the tangent bundle, we construct the coordinate system with any two linearly independent (orthogonal) vectors of the tangent bundle and outer-normal vector as the coordinate axes. It is supposed that the coordinate system introduced matches the coordinate system induced on $\partial\Omega$ by the orientation of the domain Ω.

In this work, we apply a method of deriving systems of equations that differs from the method used in [1–4] and is valid for convex domains. We sequentially consider system (3) in thus constructed coordinate systems $\mathbf{x}^\sigma = \{ x_1^\sigma, x_2^\sigma, x_3^\sigma \}$ with all σ values. Then, the system of equations (3) in the coordinate system $\mathbf{x}^\nu = \{ x_1^\nu, x_2^\nu, x_3^\nu \}$ for arbitrary $\sigma = \nu$ with the Fourier-transform parameters $\alpha^\nu = \{ \alpha_1^\nu, \alpha_2^\nu, \alpha_3^\nu \}$ is represented in the form

$$\mathbf{K}(\alpha^\nu)\mathbf{\Phi}^-(\alpha^\nu) = -\mathbf{G}^-(\alpha^\nu) + \iint\limits_{\partial\Omega} \boldsymbol{\omega}^-(\alpha^\nu). \qquad (5)$$

Here,

$$\Phi(\alpha^\nu) = \Phi(\alpha_1^\nu, \alpha_2^\nu, \alpha_3^\nu),$$

and the minus sign means that the functions of the parameter α_3^ν that enter into Eq. (5) are regular in the domain λ_- for the real parameters α_1^ν and α_2^ν. As mentioned above, we pass from the original coordinate system $\mathbf{x}$ to the local system $\mathbf{x}^\nu$ that is described in [1–4] and will be called the initial system.

Multiplying Eq. (5) by $\mathbf{K}_+^{-1}(\alpha_3^\nu)$, we obtain

$$\mathbf{K}_-(\alpha_3^\nu)\mathbf{\Phi}^-(\alpha_3^\nu) = \mathbf{K}_+^{-1}(\alpha_3^\nu)\left[\sum_\nu \iint\limits_{\partial\Omega} \varepsilon_\nu \boldsymbol{\omega}^-(\boldsymbol{\alpha}^\nu) - \mathbf{G}(\boldsymbol{\alpha}^\nu)\right], \qquad (6)$$

where all components of the vector function on the left-hand side are regular in the domain λ_-. We require that the vector function on the right-hand side has the same property. Then, the projection of the right-hand side of the analytic functions of the parameter α_3^ν onto the domain λ_+ is equated to zero, and we arrive at the expressions

$$\int\limits_\Gamma \mathbf{K}_+^{-1}(\alpha_3^\nu)\left[\sum_\nu \iint\limits_{\partial\Omega} \varepsilon_\nu \boldsymbol{\omega}^-(\boldsymbol{\alpha}^\nu) - \mathbf{G}^-(\boldsymbol{\alpha}^\nu)\right] \times (\alpha_3^\nu - \beta_3^\nu)^{-1} d\alpha_3^\nu = 0, \quad \beta_3^\nu \in \lambda_+. \qquad (7)$$

We note that the elements of the mth row of the matrix function $\mathbf{K}_+^{-1}(\alpha_3^\nu)$ are representable as

$$S_{mn}(\alpha_1^\nu, \alpha_2^\nu, \alpha_3^\nu) = \frac{S_{mn}^0(\alpha_1^\nu, \alpha_2^\nu, \alpha_3^\nu)}{K_+(\alpha_3^\nu)},$$

where the functions in the numerator of the right-hand side have no singularities in the domain λ_-. Let $\alpha_{3\tau}^{\nu-}$ be zeros of the determinant $\mathbf{K}_+(\alpha_3^\nu)$ that lie in the lower half-plane and depend on α_k^ν, $k = 1, 2, \ldots$. For simplicity, we suppose that zeros are simple with unit codimension. In this case, the Leray form residual is determined by simple formulas.

Closing the integration contour Γ in Eq. (7) in the lower half-plane, we arrive at the relations

$$\sum_{n=1}^N S_{mn}^0(\alpha_1^\nu, \alpha_2^\nu, \alpha_{3\tau}^{\nu-}) \times \iint\limits_{\partial\Omega} \sum_\sigma [\varepsilon_\sigma \omega_n^-(\alpha_1^\nu, \alpha_2^\nu, \alpha_{3\tau}^{\nu-}) - G_n^-(\alpha_1^\nu, \alpha_2^\nu, \alpha_{3\tau}^{\nu-})] = 0, \qquad (8)$$

$$\tau = 1, 2, \ldots, T, \quad T \le N.$$

The number of equations is equal to the number T of the zeros of the function $\mathbf{K}_+(\alpha_1^\nu, \alpha_2^\nu, \alpha_3^\nu)$ as a function of $\alpha_{3\tau}^{\nu-} = \alpha_{3\tau}^{\nu-}(\alpha_1^\nu, \alpha_2^\nu)$ that lie in the domain λ_-.

Using the properties of exterior forms in the chosen coordinate system, we represent the element $\varepsilon_\nu \omega_n^-(\alpha_1^\nu, \alpha_2^\nu, \alpha_{3\tau}^{\nu-})$ as

$$\varepsilon_\nu \omega_n^- = \sum_{m=1}^N \varphi_m(x_1^\nu, x_2^\nu, 0) e^{i\langle \alpha^\nu \mathbf{x}^\nu \rangle} \alpha_{nm3} dx_1^\nu \wedge dx_2^\nu.$$

We now consider an element with an index $\sigma \ne \nu$, i.e., $\varepsilon_\sigma \omega_n^-(x_1^\nu, x_2^\nu, x_3^\nu, \alpha_1^\nu, \alpha_2^\nu, \alpha_3^{\nu-})$, which includes three terms in parentheses in its representation. Passing in it to the local coordinate system corresponding to the decomposition element ε_σ and remaining the Fourier-transform parameters $\boldsymbol{\alpha}^\nu$ unchanged, we arrive at the representation

$$\varepsilon_\sigma \omega_n^- = \sum_{m=1}^N \varphi_{m\sigma}(x_1^\sigma, x_2^\sigma, 0) e^{i\langle \boldsymbol{\alpha}^\nu \mathbf{x}^\nu(\mathbf{x}^\sigma) \rangle} \times \alpha_{nm3} R(x_1^\sigma, x_2^\sigma) dx_1^\sigma \wedge dx_2^\sigma.$$

Here, $\mathbf{x}^\nu(\mathbf{x}^\sigma)$ is the linear transformation from the initial system x^ν to the new system x^σ, $R(x_1^\sigma, x_2^\sigma)$ is the Jacobian of the transition from the initial system to the new one, and

$$\varepsilon_\sigma \varphi_m = \varphi_{m\sigma}(x_1^\sigma, x_2^\sigma, 0). \quad (9)$$

3. Let us treat the vectors $\varphi_\sigma = \{\varphi_{m\sigma}(x_1^\sigma, x_2^\sigma, 0)\}$ as the elements of a certain Banach space, e.g., L_p, $p > 1$, specified in domains $\partial\Omega_\sigma$, which are the supports of the projectors ε_σ.

Expressing one of the functions in terms of others from boundary conditions (1), substituting these functions into Eqs. (8), and taking the introduced Banach space into account, we obtain the pseudodifferential equation

$$\sum_\sigma \int\int_{\partial\Omega_\sigma} \sum_{q=1}^N s_{mq}(x_1^\nu, x_2^\nu, \xi_1^\sigma, \xi_2^\sigma)\varphi_{q\sigma}(\xi_1^\sigma, \xi_2^\sigma, 0)$$

$$\times R(\xi_1^\sigma, \xi_2^\sigma)\xi_1^\sigma \wedge \xi_2^\sigma = F^{-1}(x_1^\nu, x_2^\nu)G_{m\nu}(\alpha_1^\nu, \alpha_2^\nu, \alpha_{3\tau}^{\nu-}),$$

$$s_{mq}(x_1^\nu, x_2^\nu, \xi_1^\sigma, \xi_2^\sigma) = \frac{1}{4\pi^2}\int_{-\infty}^{\infty}\int \sum_{k=1}^N S_{mk}^0(\alpha_1^\nu, \alpha_2^\nu, \alpha_{3\tau}^{\nu-})a_{kq3}, \quad (10)$$

$$\exp i[\langle \alpha_1^\nu \xi_1^\nu(\xi^\sigma) + \alpha_2^\nu \xi_1^\nu(\boldsymbol{\xi}^\sigma) + \alpha_{3\tau}^{\nu-}(\alpha_1^\nu, \alpha_2^\nu)\xi_3^\nu(\boldsymbol{\xi}^\sigma)\rangle$$

$$- \langle \alpha_1^\nu x_1^\nu + \alpha_2^\nu x_2^\nu\rangle]d\alpha_1^\nu \wedge d\alpha_2^\nu,$$

$$x_1^\nu, x_2^\nu \in \partial\Omega_\nu.$$

Here, it is necessary to replace M linearly independent functions $\varphi_{q\sigma}(\xi_1^\sigma, \xi_2^\sigma, 0)$ that are obtained by solving system (2) by $N - M$ dependent functions, which become unknown for the system of pseudodifferential equations.

For the decomposition element $\sigma = \nu$, kernel (10) takes a form where $\xi_3^\nu(\boldsymbol{\xi}^\nu) = 0$ should be assumed with allowance for this replacement. Moreover, the following inequalities are valid:

$$\mathrm{Im}\alpha_{3\tau}^{\nu-}(\alpha_1^\nu, \alpha_2^\nu) < 0, \quad \xi_3^\nu(\boldsymbol{\xi}^\sigma) < 0, \quad \sigma \neq \nu. \quad (11)$$

Then, for the assumed decomposition element, we obtain the representation

$$s_{mq}(x_1^\nu, x_2^\nu, \xi_1^\nu, \xi_2^\nu) = \frac{1}{4\pi^2}\int_{-\infty}^{\infty}\int \sum_{k=1}^N S_{mk}^0(\alpha_1^\nu, \alpha_2^\nu, \alpha_{3\tau}^{\nu-})a_{kq3}, \quad (12)$$

$$\exp i[\langle \alpha_1^\nu(\xi_1^\nu - x_1^\nu) + \alpha_2^\nu(\xi_2^\nu - x_2^\nu)\rangle]d\alpha_1^\nu \wedge d\alpha_2^\nu.$$

Thus, the resulting pseudodifferential equation belongs to the equations of the theory of vibration-strength viruses [6], and the mathematical technique developed in that work can be applied for its inversion.

Inverting the pseudodifferential operator with kernel (12), we represent system (10) in the form of the system of integral equations of the second kind [1–4]. In view of properties (11), this system is normally solvable in L_p, $p > 1$. For sufficiently large $|\mathrm{Im}\xi_3^\nu(\xi^\sigma)|$, $\sigma \neq \nu$, the operator of the second kind is a contraction. Various methods of discretization of the system are applicable in the general case.

Solving the system of pseudodifferential equations (10) and substituting the component of the desired vector function $\boldsymbol{\varphi}$ into Eq. (6), we represent the solution in the form

$$\boldsymbol{\varphi}(\mathbf{x}) = \frac{1}{8\pi^3}\iiint \mathbf{K}_-^{-1}(\alpha_3^\nu)\mathbf{K}_+^{-1}(\alpha_3^\nu)$$

$$\times\left[\sum_\sigma \int\int_{\partial\Omega_\sigma} \varepsilon_\sigma \boldsymbol{\omega}_\sigma^-(\boldsymbol{\alpha}^\nu) - \mathbf{G}(\boldsymbol{\alpha}^\nu)\right],$$

$$e^{-i\langle \boldsymbol{\alpha}^\nu \mathbf{x}^\nu\rangle}d\alpha_1^\nu \wedge d\alpha_2^\nu \wedge d\alpha_3^\nu.$$

The derived representation of solutions of the system of coupled boundary value problems is similarly generalized for spaces of higher dimensions. It ensures determination of the effect of the parameters of various fields [7–10] on the characteristics of the individual components of coupled fields. Solutions in certain nonconvex and multiply connected domains can be described by similar formulas with the use of a method simply modified for domains of a more complex structure constructed from convex domains of type Ω.

The representation allows a number of simplifications that make it possible to analyze the basic properties of solutions.

ACKNOWLEDGMENTS

This work was supported by the Russian Foundation for Basic Research (project no. 03-01-00694); the R2003YuG program, the Russian Foundation for Basic Research (project nos. 03-01-96537, 03-01-96527, 03-01-96519, 03-01-96584); the "Integratsiya" program (project no. B0121); the Council of the President of the Russian Federation for Support of Young Russian Scientists and Leading Scientific Schools (project no. NSh-2107.2003); and the Branch of Physical and Technical Problems of Energetics and Presidium of the RAS through the programs conducted by the Southern Scientific Center, Russian Academy of Sciences.

REFERENCES

1. V. A. Babeshko and O. M. Babeshko, Dokl. Akad. Nauk **389**, 184 (2003) [Dokl. Phys. **48**, 134 (2003)].
2. V. A. Babeshko and O. M. Babeshko, Dokl. Akad. Nauk **392**, 767 (2003) [Dokl. Phys. **48**, 594 (2003)].
3. V. A. Babeshko and O. M. Babeshko, Dokl. Akad. Nauk **392**, 163 (2003) [Dokl. Phys. **48**, 512 (2003)].
4. V. A. Babeshko and O. M. Babeshko, Dokl. Akad. Nauk **399** (3) (2004) (in press).
5. V. A. Babeshko and O. M. Babeshko, Dokl. Akad. Nauk **399** (1) (2004) (in press).
6. V. A. Babeshko and O. M. Babeshko, Dokl. Akad. Nauk **393** (4), 473 (2003) [Dokl. Phys. **48**, 669 (2003)].
7. W. Nowacki, *Electromagnetic Effects in Solids* (PWN, Warsaw, 1983; Mir, Moscow, 1986).
8. V. M. Sorokin and G. V. Fedorovich, *Physics of Slow MHD Waves in the Ionospheric Plasma* (Énergoizdat, Moscow, 1982) [in Russian].
9. V. A. Babeshko, O. V. Evdokimova, and S. M. Evdokimov, Ékol. Vestn. Nauch. Tsentrov Chernomor. Ékon. Sotrudnichestva, No. 1, 6 (2003).
10. O. M. Babeshko, Ékol. Vestn. Nauch. Tsentrov Chernomor. Ékon. Sotrudnichestva, No. 1, 82 (2004).

Translated by R. Tyapaev

Doklady Physics, Vol. 50, No. 1, 2005, pp. 49–51. Translated from Doklady Akademii Nauk, Vol. 400, No. 2, 2005, pp. 197–199.

MECHANICS

Regimes of the Flow around a Pair of Plates Perpendicular to the Flow

A. V. Gudzovskiĭ

Presented by Academician O.M. Belotserkovskiĭ August 19, 2004

Received August 25, 2004

Oscillatory regimes of a viscous incompressible flow around a pair of plates set transverse to the flow in the same plane are investigated and the regime-stability boundaries are determined. The conditions under which the flow around long plates of width d is plane and unsteady are considered; they correspond to the Reynolds numbers $30 < \mathrm{Re} = \frac{Vd}{\nu} \le 80$, where V is the freestream velocity and ν is the kinematic viscosity. The second parameter of the problem, namely, the width G of the gap between the plates, is not greater than 3 (the variables are normalized on the length d, time $\frac{d}{V}$, and pressure V^2 scales).

1. The transverse flow around a pair of plates is similar to the flow around a pair of circular cylinders of diameter d, which is studied in more detail in [1, 2]. The visually determined flow patterns may be either oscillatory (regular) or aperiodic. Regular oscillations can occur both in phase and in opposite phase. The period-averaged parameters of the flow downstream of the bodies can be either equal (E-type regime) or different (D-type regime, in which the gap flow is on average diverted toward one of the bodies).

The boundaries of the realization domains for different flow regimes in the (Re, G) plane were determined in the numerical experiments in [2]; they are different from the sought flow-regime-stability boundaries (see, e.g., [3]).

2. We will place the origin in the middle of the gap between the plates and align the x axis with the flow. Then, the y axis passes through both plates.

The numerical experiments were carried out using the FlowVision code [4]. The velocity and pressure fields are determined by integrating the Navier–Stokes equations on a staggered Cartesian grid by an explicit finite-volume projection-type method. Conventional boundary conditions [5] are imposed on the boundaries of the rectangular computation domain $-20 \le x \le 70$, $|y| \le 20$ and on the plates. The computation grid steps Δx and Δy are nonuniform; the cells are minimum ($\Delta x = \Delta y = 0.05$) in the vicinities of the plates and in the near wake ($|y| \le 3$, $-0.2 \le x \le 4$) and increase up to $\Delta x = \Delta y = 0.5$ in the periphery.

We define the flow-regime-stability boundaries in the (Re, G) plane as curves on which the dependence of the flow regime on the problem parameters Re and G becomes discontinuous [5, 6]. In determining the stability boundary for a certain regime R, the flow is calculated for a set of points. For each new point (Re_1, G_1), the solution at the neighboring point (Re_2, G_2), which belongs to the regime-R stability domain, is taken for the initial approximation. If the type of the flow thus obtained at the point (Re_1, G_1) is different from R, then the regime-R stability boundary is let pass between these points.

3. In classifying the oscillatory regimes of the flow around the plates, we proceed from the assumption that the flow regime with a vortex street downstream of a plate is a hydrodynamic oscillator (self-oscillation system), while the flow behind a set of plates is a result of the nonlinear interaction between oscillators. Both an individual oscillator and several interacting oscillators are characterized by the time (t) dependence of the drag coefficients of the plates $C_{\mathrm{D},i}(t)$, $i = 1, 2$. These dependences are the integral characteristics of the vortex flow in the near wake downstream of the plate.

In the interaction of hydrodynamic oscillators, long-wavelength modes are excited with frequencies that are multiples of the frequency of the vortex shedding downstream of one plate. In regular flow regimes, the function $C_{\mathrm{D},i}(t) - C^{(0)}_{\mathrm{D},i}$, where $C^{(0)}_{\mathrm{D},i}$ is the mean value of $C_{\mathrm{D},i}(t)$, can be presented as a superposition of N oscillation modes ($N = 1$, 2, or 3) with multiple frequencies $f^{(k)}$, $k = 1, 2, \ldots, N$, such that $f^{(k)} = n_{k+1} f^{(k+1)}$, where n_{k+1} are integers ($5 \le n_2 \le 27$ and $5 \le n_3 \le 9$ under the conditions considered above). For the ith plate, the kth mode is characterized by an amplitude $B_i^{(k)}$, a phase

Institute for Computer Aided Design,
Russian Academy of Sciences,
Vtoraya Brestskaya ul. 19/18, Moscow, 123056 Russia
e-mail: agudzovsky@mtu-net.ru

1028-3358/05/5001-0049$26.00

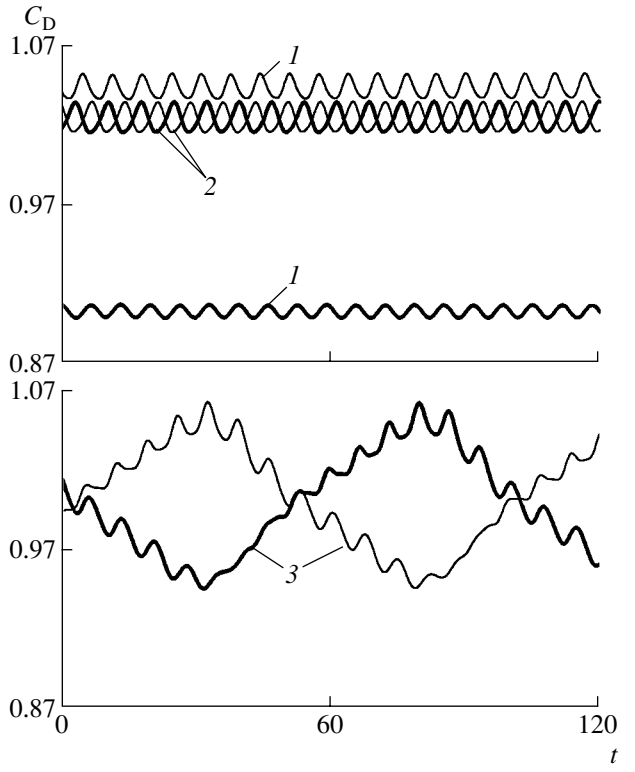

Fig. 1. $C_{D,i}(t)$ dependences for i = (thin lines) 1 and (thick lines) 2 at Re = 28.46 and G = 2.3 in the (*1*) DS, (*2*) EA, and (*3*) ESδ regimes.

$\varphi_i^{(k)}$ $(0 \le \varphi_i^{(k)} < 1)$, and the form of a periodic function $F_i^{(k)}(t)$ (the mean value of $F_i^{(k)}(t)$ over the period $\tau^{(k)} = \frac{1}{f^{(k)}}$ is equal to zero).

The flow may be of either the E type, if $C_{D,1}^{(0)} = C_{D,2}^{(0)}$, or the D type, if $C_{D,1}^{(0)} \neq C_{D,2}^{(0)}$. In the D flow regime, both the functions $F_1^{(k)}(t)$ and $F_2^{(k)}(t)$ and the amplitudes $B_1^{(k)}$ and $B_2^{(k)}$ are different, whereas in the E regime they coincide.

Four base types of oscillations of the *k*th mode were found, namely, S (in-phase oscillations, $\Delta\varphi^{(k)} = \varphi_1^{(k)} - \varphi_2^{(k)} = 0$); A (antiphase oscillations, $\Delta\varphi^{(k)} = \text{const} > 0$); δ (oscillations with a fundamental mode phase difference, $\Delta\varphi^{(1)} = \delta(t)$ varying during an oscillation period); and C (degenerate oscillations with $f^{(k)} = 0$). Moreover, for the second mode (k = 2), a μ oscillation type is observable, in which $F_i^{(2)}(t)$ has more than two extrema in a period.

We will use a set of $N + 1$ symbols for indicating the flow regime. The first symbol indicates the type of the flow regime, E or D, while the $(k + 1)$th symbol indicates the type of the *k*th-mode oscillation.

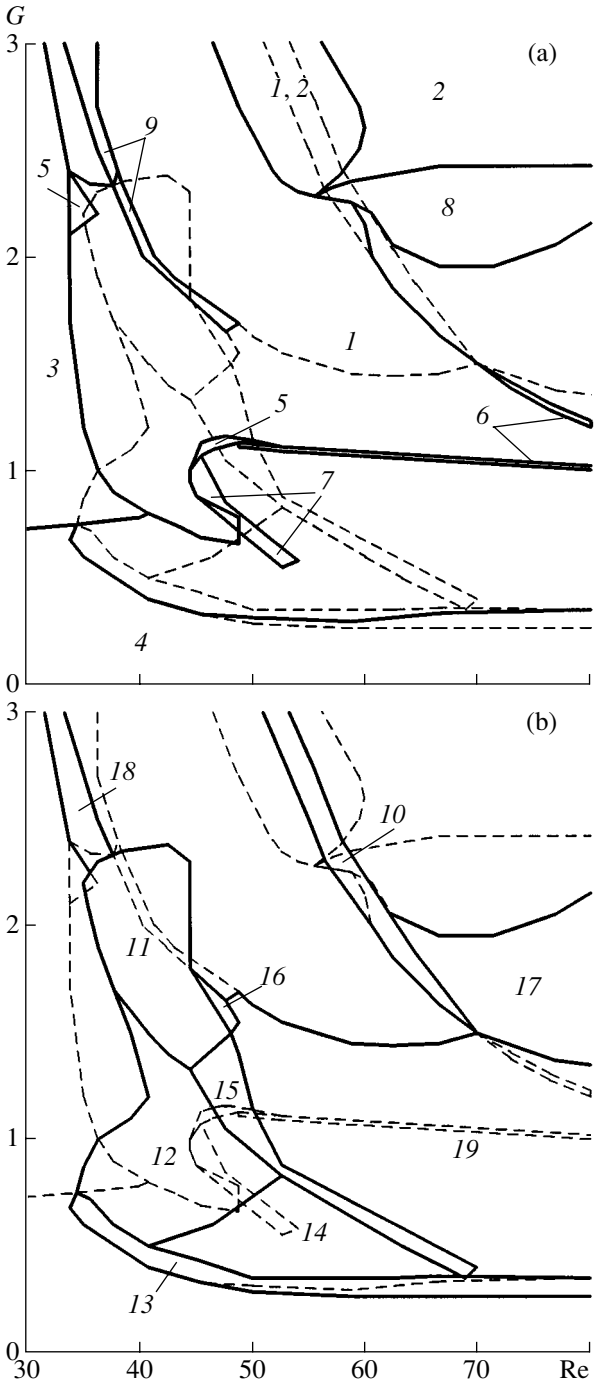

Fig. 2. Stability boundaries for the (a) E-type regimes: (*1*) EA, (*2*) ES, (*3*) EC, (*4*) EA_2, (*5*) EAA, (*6*) EAA and EAAA, (*7*) EAAS, (*8*) EAδ, and (*9*) ESδ; and (b) D-type regimes: (*10*) DA, (*11*) DS, (*12*) DC, (*13*) DA_2, (*14*) DS_2, (*15*) DSA, (*16*) DSμ, (*17*) DAδ, (*18*) DSδ, and (*19*) D*.

Figure 1 presents an example of the $C_{D,i}(t)$, i = 1, 2, dependence for the DS, EA, and ESδ regimes obtained for Re = 38.46 and G = 2.3.

4. In the (Re, *G*) plane, the stability boundaries were determined for the following regimes of the flow around the pair of plates: type-E flow regimes (EA, ES, EC, EAA, EAδ, ESδ, EAAA, and EAAS) and type-D regimes (DA, DS, DC, DSA, DSμ, DAδ, and DSδ), for which the fundamental mode frequency $f^{(1)}$ is equal to the frequency of the vortex shedding behind one plate of width *d*, as well as EA_2, DA_2, and DS_2 regimes, for which $f^{(1)}$ is equal to the frequency of oscillations behind a plate of width 2*d*. Moreover, the stability boundary of the flow regime with aperiodic oscillations is determined. This regime, which is designated as D*, belongs to the type-D flows.

In Fig. 2, the regime-stability boundaries are grouped according to the type of the regime: the solid lines in Figs. 2a and 2b show the stability boundaries for the E and D regimes, respectively. The dashed lines in Fig. 2 indicate the boundaries of the regimes of the opposite type.

A particular group is formed by the "resonance" regimes DA, ESδ, DSA, EAAA, and EAAS. For these regimes, the stability domains in the (Re, *G*) plane are narrow bands. In Fig. 3, curves $G\left(\frac{\mathrm{Re}}{\mathrm{Re}_1}\right)^{\gamma} = 1$, where Re_1 and γ are some constants, are plotted on the stability-domain boundaries (dashed lines). It is seen that these curves pass along the bands of all the "resonance" regimes and certain stability boundaries, as well as in the vicinities of singular points at which the stability boundaries of regimes of different types intersect each other (in Fig. 3, they are shown as circles).

Many stability regions for regimes of the same type do not overlap with each other. For this reason, regime-to-regime transitions are continuous. An exception is the overlapping stability domains EA and ES and the resonance-regime domains, overlapping partially the domains of "conventional" regimes (thus, ESδ and EAAS overlap with EA, DSA and EAA with DC, and DA with DAδ).

The boundaries of transitions between flow regimes of different types do not usually coincide, so that transitions between regimes are accompanied by hysteresis. Exceptions are the EAδ $\rightleftharpoons$ DAδ, ESδ $\leftrightarrow$ DSδ, and, partially, $EA_2 \rightleftharpoons DA_2$ (for small Re) transitions.

Varying the parameters Re and *G* (see Fig. 2), we can go from single-mode regimes (EA, DC, DS, DA_2, DS_2) to the aperiodic D* regime via multimode regimes (EAA, EAAA, DSA, and DSμ). The D* regime occurs due to long-wave instability of the multimode flow regimes.

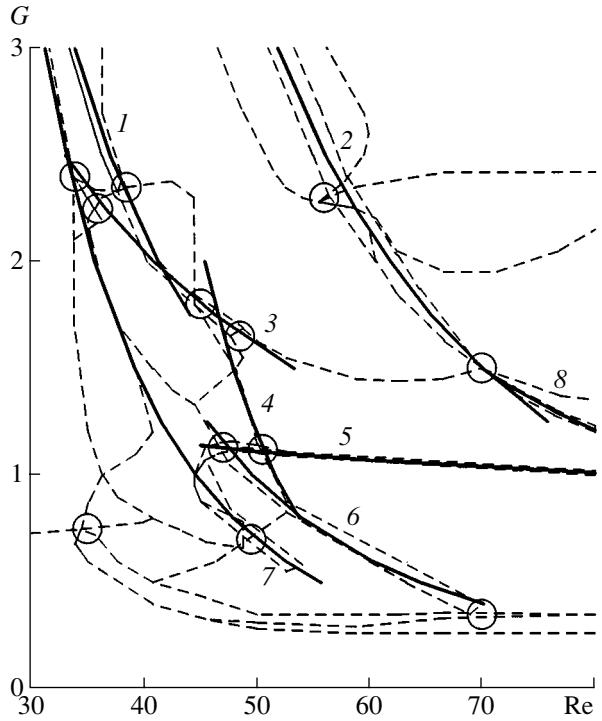

Fig. 3. (Dashed lines) Stability boundaries of the E-type and D-type regimes and curves $G\left(\frac{\mathrm{Re}}{\mathrm{Re}_1}\right)^{\gamma} = 1$; γ = (*1*) 2.08, (*2*) 2.30, (*3*) 1.08, (*4*) 5.43, (*5*) 0.207, (*6*) 2.64, (*7*) 3.12, and (*8*) 1.89; Re_1 = (*1*) 57.7, (*2*) 84.5, (*3*) 77.7, (*4*) 51.6, (*5*) 83.6, (*6*) 49.7, (*7*) 44.6, and (*8*) 86.6.

REFERENCES

1. C. H. K. Williamson, J. Fluid Mech. **150**, 1 (1985).
2. S. Kang, Phys. Fluids **15** (9), 2486 (2003).
3. A. V. Gudzovskiĭ, in *Proceedings of the 2nd Russian Conference on Heat Transfer* (MÉI, Moscow, 1998) [in Russian].
4. A. V. Gudzovskiĭ, Zh. Vychisl. Mat. Mat. Fiz. **41**, 1250 (2001).
5. A. V. Gudzovskiĭ, Izv. Akad. Nauk, Mekh. Zhidk. Gaza, No. 2, 56 (2003).
6. A. V. Gudzovskiĭ, Dokl. Akad. Nauk **397** (1), 49 (2004) [Dokl. Phys. **49**, 428 (2004)].

Translated by M. Lebedev

Doklady Physics, Vol. 50, No. 1, 2005, pp. 52–55. Translated from Doklady Akademii Nauk, Vol. 400, No. 2, 2005, pp. 200–203.

MECHANICS

Hydrodynamic and Electromagnetic Model of Strata Saturated with Oil and Free Gas

N. K. Korsakova*, V. I. Pen'kovskiĭ*, and Corresponding Member of the RAS M. I. Épov**

Received July 6, 2004

Mathematically modeling hydrodynamic processes of penetration of drilling-mud filtrate into strata saturated with oil and water is the basis for a new method of probabilistic convolutions [1]. This method is developed for interpreting the data of electromagnetic sounding in boreholes. The much more complicated problem is the description of the process of penetration into strata containing three combined immiscible phases: oil, gas, and mineralized connate water bound with the stratum skeleton. In this case, we have to seek the solution to a system of two quasi-linear equations, which is impossible to represent in an analytical form. In addition, the character of the interaction of the fresh mud filtrate with stratum water depends on the mutual position of two fronts, namely, the displacement of gas by water and oil by water.

In this study, we propose both a new formulation and a method for solving the problem concerning the interpretation of electromagnetic-logging data for strata containing a combination of oil, gas, and native water. We have found a noticeable dependence for shapes of the curves corresponding to sounding-device data on the degree of the stratum saturation with free gas.

As long as the gas dynamic viscosity is small compared to that of liquid fluids, the process of the filtrate penetrating into a gas-bearing layer [2] is similar to that of piston-like displacement. This fact makes it possible to substantiate the partial linearization of three-phase filtration equations.

While drilling a borehole, the action of capillary forces in penetration processes is small compared to that of hydrodynamic forces. In the axisymmetric case, the three-phase immiscible filtration in the near-borehole zone can be described by the set of Bucley–Leverett equations [3]

$$\frac{1}{r}\frac{\partial}{\partial r}(rv_i) + m\frac{\partial s_i}{\partial t} = 0,$$
$$v_i = -k_i f_i \frac{\partial h}{\partial r}. \tag{1}$$

Here, r, t, and m are, respectively, the coordinate, time, and porosity. The quantities without subscripts correspond to the oil phase, whereas the subscripts $i = 0, 1$ refer to the gas and water phases, respectively. The first three equations in set (1) describe the mass-conservation law for moving phases. The following three equations correspond to the generalized Darcy law that links the radial velocities of motion v_i with the gradient of head h identical for all the phases. The filtration coefficients k_i are inversely proportional to the dynamic viscosities μ_i of the phases and are directly proportional to the collector permeability. The relative phase permeabilities f_i are usually expressed in the form of power-law functions depending on the effective saturations s_i^n, where the exponent n is $n \approx 3.5$. Since $\sum_i s_i = 1$, set of equations (1) has the first integral

$$r(v + v_0 + v_1) = r_w V(t), \tag{2}$$

where r_w is the borehole radius and $V(t)$ is the total volume velocity for the phases. We now introduce the generalized Leverett functions

$$F_i(s, s_0) = \frac{\alpha_i f_i(s_i)}{\sum_i \alpha_i f_i(s_i)},$$

$$\sum_i F_i(s, s_0) = 1, \quad \alpha_i = \frac{\mu_i}{\mu_1}, \quad \alpha_1 = 1, \quad \alpha \le 1,$$
$$\alpha_0 \gg 1.$$

From the law of phase motion and relationship (2), we obtain the expression for the phase filtration velocity:

$$rv_i = F_i(s, s_0) r_w V(t). \tag{3}$$

* *Lavrent'ev Institute of Hydrodynamics, Siberian Division, Russian Academy of Sciences, pr. Lavrent'eva 15, Novosibirsk, 630090 Russia*
e-mail: korsakova@hydro.nsc.ru; penkova@hydro.nsc.ru;

** *Institute of Geophysics, Siberian Division, Russian Academy of Sciences, pr. Akademika Koptyuga 3, Novosibirsk, 630090 Russia*
e-mail: mepov@uiggm.nsc.ru

1028-3358/05/5001-0052$26.00

Set of equations (1) is transformed into the simple form

$$\begin{aligned}\frac{\partial s_0}{\partial \tau} + \frac{\partial F_0}{\partial s}\frac{\partial s}{\partial x} + \frac{\partial F_0}{\partial s_0}\frac{\partial s_0}{\partial x} &= 0,\\ \frac{\partial s}{\partial \tau} + \frac{\partial F}{\partial s}\frac{\partial s}{\partial x} + \frac{\partial F}{\partial s_0}\frac{\partial s_0}{\partial x} &= 0,\end{aligned} \tag{4}$$

where $\tau = \frac{2}{mr_w}\int_0^t V(t)dt$ and $x = \left(\frac{r}{r_w}\right)^2$ are new independent variables. The variable τ is associated with the conditional radius $r_n = r_w\sqrt{1+\tau}$ of the volume penetration of the filtrate into a stratum. Let s_0, s_1^0, $s_0^0 = 1 - (s^0 + s_1^0)$ be the initial values of the stratum saturation for oil, water, and gas phases, respectively. The mobilities of each phase basically depend on the products $\alpha_i f_i$. The gas phase is the most mobile ($\alpha_0 \approx 50$). Therefore, its displacement by liquids is similar to the piston-like displacement. At the fronts $r = r_{fi}$ of the displacement of oil or gas ($i = 0$) by water, kinematic conditions

$$\begin{aligned}&v_i(r_{fi} - 0, t) - v_i(r_{fi} + 0, t)\\ &= m[s_i(r_{fi} - 0) - s_i(r_{fi} + 0)]\frac{dr_{fi}}{dt}\end{aligned} \tag{5}$$

must be fulfilled. These conditions follow from the integral laws of mass conservation [3]. Two cases are possible, depending on the relation between the stratum saturation with oil s_0 and with gas s_0^0, namely, either the gas displacement front advances the oil displacement front; i.e., $r_{f0} > r_f$, or the stratum saturation with gas is as low that the front of its displacement delays with respect to the oil displacement front; i.e., $r_{f0} < r_f$. In the first case, from Eq. (5) and relationship (3) for $i = 0$, with allowance for the initial condition $r_{f0} = r_w$ we obtain

$$r_{f0} = r_w\sqrt{1 + \frac{\tau F_0(s^0, s_0^0)}{s_0^0}}. \tag{6}$$

In the case of the piston-like displacement, the gas-saturation distribution in the stratum near-borehole zone has the form of a step function: $s_0 \equiv 0$ for $r_w < r < r_{f0}(\tau)$ and $s_0 \equiv s_0^0$ for $r > r_{f0}(\tau)$. This distribution corresponds to the transport equation

$$\frac{\partial s_0}{d\tau} + \frac{F(s^0, s_0^0)}{s_0^0}\frac{\partial s_0}{\partial x} = 0.$$

This equation is obtained from the first equation of set (4) if we assume $\frac{\partial s}{\partial x} = \frac{\partial s_0}{\partial x} = 0$ and

$$\frac{\partial F_0}{\partial s} \approx \frac{\Delta F_0}{\Delta s_0} = \frac{F_0(s^0, s_0^0) - F(s^0, s_0^0)}{s_0^0} = \frac{F_0(s^0, s_0^0)}{s_0^0}.$$

Then, the second equation of set (4) takes the form

$$\frac{\partial s}{\partial \tau} + F_s'(s, 0)\frac{\partial s}{\partial x} = 0, \quad 1 < x \le x_f = \left(\frac{r_f}{r_w}\right)^2. \tag{7}$$

The function $F(s, 0)$ coincides with the Leverett function for two-phase filtration. In this case, features of the behavior of the solutions to Eq. (7), which were found previously (see [1, 2]), are conserved. In particular, the following properties turn out to be the most important. If the initial stratum oil saturation s^0 is higher than the point of the maximum $s = s_{\max}$ at which $F_{ss}''(s_{\max}, 0) = 0$, then the solution $s = s(x, \tau)$ has discontinuities. The saturation at the displacement front $s_f < s^0$ is determined by the root of the transcendental equation

$$s_f = s^0 + \frac{F(s_f, 0) - F(s^0, 0)}{F_s'(s_f, 0)}, \tag{8}$$

that follows from kinematic condition (5). For $s^0 \le s_{\max}$, the solution $s = s(x, \tau)$ is continuous, and $s_f = s^0$. The position of the oil displacement front is determined by the formula

$$r_f = r_w\sqrt{1 + \tau F_s'(s_f, 0)}. \tag{9}$$

The average (with respect to the displacement area) oil saturation $\langle s\rangle$ is time-independent and is determined to be in the form

$$\langle s\rangle = s_f - \frac{F(s_f, 0)}{F_s'(s_f, 0)}. \tag{10}$$

We now consider the case of small s_0^0 when $r_{f0} < r_f$. In accordance with the piston-like displacement pattern, $s_0 = 0$ for $r < r_{f0}$ and $s_0 = s_0^0$ for $r_{f0} < r < r_f$. For all r except the point $r = r_{f0}$, we have $\frac{\partial s_0}{\partial r} = 0$. Therefore, in this case, the equation for the desired function $s(x, \tau)$ also is analogous to Eq. (7). The difference consists in the fact that the generalized Leverett function $F(s, s_0)$ does not coincide with the function $F(s, 0)$ for all values of r. $F(s, s_0) = F(s, s_0^0)$ within the interval $r_{f0} < r < r_f$. However, since the value of s_0^0 is low compared to the initial oil saturation s^0, we can ignore this difference in our calculations and use approximations (8)–(10). The

position of the gas displacement front can be calculated with a reasonable accuracy by the formula

$$r_{f0} = r_w\sqrt{1 + \frac{\tau F_0(\langle s\rangle, s_0^0)}{s_0^0}}.$$

This is obtained from kinematic condition (5) under the assumption that the value s of the oil saturation can be replaced by the average value $\langle s\rangle$ independent of the front position r_f.

As follows from the Archi law [4], at all other things being the same, the resistivity of a stratum with a given content is inversely proportional to the electrolyte saturation squared of the stratum porous space. The penetration of the mud water filtrate characterized by a certain salt concentration c_p into a reservoir containing oil, gas, and relatively immobile mineralized water with an unknown salt concentration c_0 is accompanied by processes of rapid salt exchange between these solutions. For the sake of simplicity, we assume that, in the region $r \in (r_w, r_f)$, the function $s(x, \tau)$ can be replaced by the average value $\langle s\rangle$ of the oil saturation. It is determined only by the initial value s^0. In the case of $r_{f0} > r_f$, the equation for the salt-mass balance

$$(r_f^2 - r_w^2)(s^0 - \langle s\rangle) + (r_{f0}^2 - r_w^2)s_0^0 = (r_{0z}^2 - r_w^2)(1 - \langle s\rangle)$$

must be fulfilled. It follows from here that the position ($r = r_{0z}$) of the boundary separating fresh and salt water is determined by the expression

$$r_{0z} = \sqrt{\frac{s_0^0 r_{f0}^2 + (s^0 - \langle s\rangle)r_f^2 + s_1^0 r_w^2}{1 - \langle s\rangle}}. \qquad (11)$$

Based on the Archi law and taking into account the distribution of the saturation of the stratum porous space with solutions of different mineralizations, we obtain four values of the resistivity:

$$R = \begin{cases} R_n = \dfrac{R_n^0}{(1 - \langle s\rangle)^2}, & r \in (r_w, r_{0z}), \\ R_{0z} = R_0\left(\dfrac{1 - s^0 - s_0^0}{1 - \langle s\rangle}\right)^2, & r \in (r_{0z}, r_f), \\ R_f = R_0\left(\dfrac{1 - s^0 - s_0^0}{1 - s^2}\right)^2, & r \in (r_f, r_{f0}), \\ R_0 = \dfrac{R^0}{(1 - s^0 - s_0^0)^2}, & r \in (r_{f0}, \infty). \end{cases} \qquad (12)$$

Here, R^0 and R_n^0 are the resistivities of a stratum completely saturated with native water and with mud filtrate, respectively.

When the initial gas content s_0^0 in a stratum decreases, the front of its displacement r_{f0} approaches that of oil r_f. The length of the interval (r_f, r_{f0}) tends to zero. Thus, in accordance with the convolution equation [1], the contribution of the specific resistance R_f to the calculation result for seeming resistances $\bar{R}_i$ becomes small. In the case of small s_0^0 when $r_{f0} < r_f$, we can see that the mass-balance equation for salts in the solution with salt concentration c_p is of the form

$$(r_f^0 - r_w^2)(s^0 - \langle s\rangle) + (r_{f0}^2 - r_w^2)s_0^0 = (r_{0z}^2 - r_w^2)(1 - \langle s\rangle) - (r_{0z}^2 - r_{f0}^2)s_0^0.$$

Hence, we arrive at the formula for the determination of the radius r_{0z} of the bordering zone:

$$r_{0z} = \sqrt{\frac{s^0 - \langle s\rangle r_f^2 + s_1^0 r_w^2}{1 - \langle s\rangle - s_0^0}}. \qquad (13)$$

The distribution of the resistivity in a stratum can be represented by a step function

$$R = \begin{cases} R_n = \dfrac{R_n^0}{(1 - \langle s\rangle)^2}, & r \in (r_w, r_{f0}), \\ R_{f0} = R_n\left(\dfrac{1 - \langle s\rangle}{1 - \langle s\rangle - s_0^0}\right)^2, & r \in (r_{f0}, r_{0z}), \\ R_{0z} = R_0\left(\dfrac{1 - s^0 - s_0^0}{1 - \langle s\rangle - s_0^0}\right)^2, & r \in (r_{0z}, r_f), \\ R_0 = \dfrac{R^0}{(1 - s^0 - s_0^0)^2}, & r \in (r_f, \infty). \end{cases} \qquad (14)$$

As $s_0^0 = 0$, formulas (11) and (13) coincide with each other and with the expression previously obtained in [2], which was used for the calculation of the bordering-zone radius r_{0z} in an oil-saturated stratum.

We now consider the centers r_i of probe sensitivities as current coordinates. Then, with due regard for Eqs. (12) and (14), from the representations of seeming resistances in the form of integral convolutions [1], for an arbitrary number of probes with identical isoparameters [5] and dispersion σ, we obtain the expressions

$$\bar{R}(r_i) = \frac{R_n - R_{f0}}{2}\left[1 + \operatorname{erf}\left(\frac{1}{2\sqrt{\sigma}}\ln\frac{x_{f0}}{x_i} - \frac{\sigma}{\sqrt{2}}\right)\right]$$

$$+ \frac{R_{f0} - R_{0z}}{2}\left[1 + \operatorname{erf}\left(\frac{1}{2\sqrt{\sigma}}\ln\frac{x_{0z}}{x_i} - \frac{\sigma}{\sqrt{2}}\right)\right]$$

$$+ \frac{R_{0z} - R_0}{2}\left[1 + \operatorname{erf}\left(\frac{1}{2\sqrt{\sigma}}\ln\frac{x_f}{x_i} - \frac{\sigma}{\sqrt{2}}\right)\right] + R_0$$

for $r_{f0} < r_f$,

$$\bar{R}(r_i) = \frac{R_n - R_{0z}}{2}\left[1 + \operatorname{erf}\left(\frac{1}{2\sqrt{\sigma}}\ln\frac{x_{0z}}{x_i} - \frac{\sigma}{\sqrt{2}}\right)\right]$$

$$+ \frac{R_{0z} - R_f}{2}\left[1 + \operatorname{erf}\left(\frac{1}{2\sqrt{\sigma}}\ln\frac{x_f}{x_i} - \frac{\sigma}{\sqrt{2}}\right)\right]$$

$$+ \frac{R_f - R_0}{2}\left[1 + \operatorname{erf}\left(\frac{1}{2\sqrt{\sigma}}\ln\frac{x_{f0}}{x_i} - \frac{\sigma}{\sqrt{2}}\right)\right] + R_0$$

for $r_{f0} > r_f$,

$$x_i = \left(\frac{r_i}{r_w}\right)^2, \quad x_{0z} = \left(\frac{r_{0z}}{r_w}\right)^2, \quad x_f = \left(\frac{r_f}{r_w}\right)^2,$$

$$x_{f0} = \left(\frac{r_{f0}}{r_w}\right)^2, \quad i = 1, 2, \ldots .$$

As our calculations show, even a small amount of gas in a stratum significantly affects the shape of the electromagnetic-logging curve. In particular, for small s_0^0, the curves of seeming resistances, along with a minimum characteristic of oil-bearing strata, possess a local maximum attainable in the zone of sensitivity centers of the first probes in the devices being employed.

REFERENCES

1. V. I. Pen'kovskiĭ and M. I. Épov, Dokl. Akad. Nauk **390**, 685 (2003).
2. M. I. Épov, V. I. Pen'kovskiĭ, N. K. Korsakova, *et al.*, Prikl. Mekh. Tekh. Fiz. **44** (6), 56 (2003).
3. I. A. Charnyĭ, *Underground Hydrodynamics and Gas-Dynamics* (Gostekhteorizdat, Moscow, 1963) [in Russian].
4. R. Collins, *Fluid Flows through Porous Materials* (New York, 1961; Mir, Moscow, 1964).
5. Yu. N. Antonov, Geol. Geofiz. **46**, 81 (1980).

Translated by G. Merzon

Doklady Physics, Vol. 50, No. 1, 2005, pp. 56–58. Translated from Doklady Akademii Nauk, Vol. 400, No. 3, 2005, pp. 338–340.

MECHANICS

Spin Detonation of Fuel–Air Mixtures in a Cylindrical Combustor

F. A. Bykovskiĭ, S. A. Zhdan, and E. F. Vedernikov

Presented by Academician V.M. Titov August 18, 2004

Received September 3, 2004

Presently, in engine combustors, turbulent burning is used. However, an alternative method, namely, detonation burning, is well-known. In the case of reliable control, it is possible to significantly intensify and to more profitably (from a thermodynamic standpoint [1]) realize the fuel combustion. The regime of continuous spin detonation combustion of an acetylene–oxygen mixture in a radial circular channel was employed for the first time in [2]. Under these conditions, the wave velocities of the reaction products were close to the sonic velocity. In the case of a separate supply of oxygen and a fuel to a combustor with the circular cylindrical geometry, the regimes of stationary burning of gaseous and liquid fuels in transverse detonation waves, which are similar to the regimes of spin detonation in circular tubes [3], were realized in [4–6]. The physicomathematical models of flows under conditions of the existence of transverse detonation waves are presented in [5, 7]. The detonation combustion of fuel–air mixtures in combustors of the liquid-fuel jet-engine type with the plane-radial geometry was investigated in [8]. A specific interest for practical investigation is the continuous detonation of fuel–air mixtures in conditions characteristic of scramjets. In this paper, we describe the realization of the steady-state regime of the detonation combustion of an acetylene–oxygen mixture in a ducted cylindrical combustor (a variant of a scramjet).

The detonation combustion chamber used by us was a coaxial channel of diameter $d_c = 30.6$ cm, length $L_c = 65.5$ cm, and width $\Delta = 2.3$ cm (Fig. 1). Air was delivered into the chamber from a circular collector with an axial cross section of 29.6 cm^2 through a circular slit with a gap of width $\delta = 0.1$, 0.2, 0.3, or 1.0 cm. At the same time, acetylene was delivered into the chamber through a spray nozzle supplied with in-pair counterflow channels with the total cross-sectional area $S_{\delta f} = 2$ cm^2, situated at a distance $L_f = 0.1$ cm downstream of the air-supply slit, and inclined at an angle of 45°. The channels are uniformly distributed over the chamber circumference. The gases were delivered from a separate receivers with volumes $V_{rA} = 79.8$ l for air and $V_{rf} = 13.3$ l for acetylene through electrically driven fast valves. Detonation products flew out directly into the atmosphere. The duration of the process was set within the time range $\tau_d \in (0.3–0.55)$ s by a control system. The flow rate of the components varied within the limits $G_{A0} = 5.3–2.12$ kg s^{-1} and $G_{f0} = 0.3–0.21$ kg s^{-1}. The fuel-excess factor was $\Phi = 0.44–1.37$ (here, the subscripts A, f, and 0 denote air, acetylene, and the initial state, respectively). The detonation was initiated by an electrical detonator with an explosive mass of 0.5 g.

The entire process was photographed through the longitudinal windows of the detonation chamber on photographic film by a photochronograph with a falling drum [9]. In order to illuminate the wave structure and detonation products, a small acetylene jet was injected into the chamber beginning oppositely to the corresponding window. Using illuminated trajectories, we determined the axial component of the flow velocity $v = k \tan\alpha\, v_{pf}$. Here, $k = 37.8$ is the image-diminution factor, α is the inclination angle of a trajectory with respect the horizontal line, and $v_{pf} = 50$ m s^{-1} is the speed of photographic-film motion. Pressure-sensor signals from the gas receivers, collectors, and from the detonation chamber were registered by a computer system.

We have realized processes characterized by one rotating wave ($n = 1$). Instantaneous patterns of the pro-

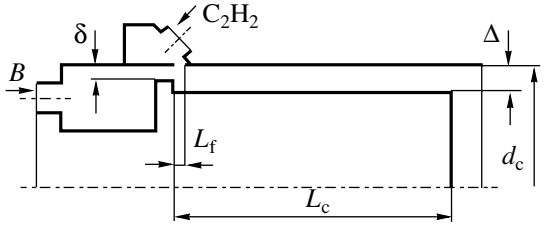

Fig. 1. Sketch of a cylindrical detonation chamber for investigating continuous spin detonation of fuel–air mixtures.

Lavrent'ev Institute of Hydrodynamics, Siberian Division, Russian Academy of Sciences, pr. Akademika Lavrent'eva 15, Novosibirsk, 630090 Russia

e-mail: bykovs@hydro.nsc.ru; zhdan@hydro.nsc.ru

1028-3358/05/5001-0056$26.00

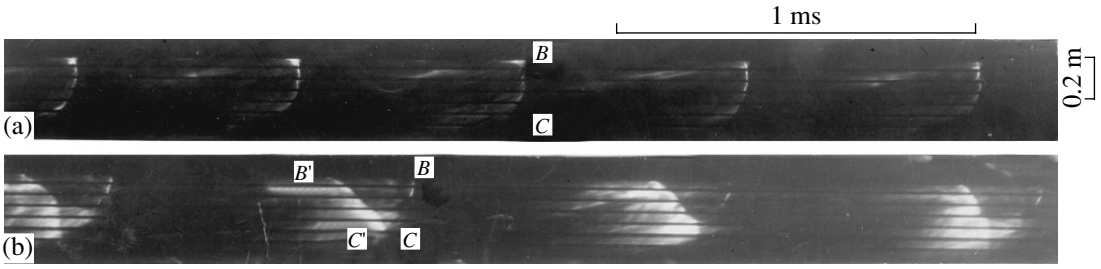

Fig. 2. Transverse detonation waves in an acetylene–air mixture: (a) $G_A = 2.96$ kg s^{-1}, $G_f = 0.3$ kg s^{-1}, $\Phi = 1.35$, $D = 1.5$ km s^{-1}; and (b) $G_A = 2.12$ kg s^{-1}, $G_f = 0.207$ kg s^{-1}, $P_c = 1.2 \times 10^5$ Pa, $\Phi = 1.3$, $D = 1.1$ km s^{-1}.

cess featuring a transverse detonation wave (δ = 0.1 cm) moving from left to right are presented in Fig. 2. The patterns were obtained by the velocity-compensation method [10]. The flow in the vicinity of a detonation wave corresponds to the flow in the coordinate system associated with the detonation wave. In each revolution over the chamber circumference, the transverse detonation wave passes the path of 4.5 cm by the longitudinal windows of the chamber (the distance between the windows is 1.5 cm). The absence of counter-flow transverse detonation waves was found. The detonation front *BC* (Fig. 2) is illuminated sufficiently well due to a purposefully targeted small acetylene jet. Downstream of the detonation front, the small jet is entrained by the flow beyond the wave in the tangential direction and escapes from the window region. Therefore, we observe a weak glow of both detonation products and other pressure shocks that accompany the detonation.

Two characteristic types of the transverse detonation wave have been observed. The first has a chemical-reaction (combustion) front adjoining the leading shock-wave front *BC* (type I, Fig. 2a). The second is the retarded pulsating combustion front *B'C'* (type II, Fig. 2b). As a rule, the latter structure corresponds to a lowered pressure in the chamber, to the case when the ratio between the components is close to the ultimate ratio ($\Phi = 0.7$), and to the case when the transverse detonation wave strongly affects the state of air in the collector ($\delta = 1.0$ cm). For waves of type II, in spite of the unsteadiness of the flow beyond the leading shock front, the average wave velocity is stable and has no deviations exceeding 1% for adjacent revolutions.

The size of the type-I transverse detonation wave at the average pressure in the chamber $P_c = (1–2.5) \times 10^5$ Pa attains the value $h \approx 23$ cm $\approx (25–60)a$, where a is the size of a self-oscillating cell of the multifront gas detonation [11] at a pressure P_c. The constant value of the quantity h is explained, apparently, by the readiness of the mixture to detonate, i.e., by the mixing processes of the components, which slightly depends on the value of P_c. The glow zone beyond the front *BC* of the type-I detonation wave attains about 1.0 cm (see Fig. 2a), i.e., about two cells each of size a, at $P_c = 2.2 \times 10^5$ Pa. For waves of type II, the size of the transverse detonation wave is larger than $h \approx 35$ cm $\approx (35–45)a$ and varies negligibly within the pressure range $P_c = (1–1.3) \times 10^5$ Pa. In the case of good mixing, the ratio $\frac{h}{a}$ for fuel–air mixtures turns out to be higher by three- to fivefold than for gas fuel–oxygen mixtures. The ratio of the transverse detonation wave size to the distance between the waves is $\frac{h}{l} = \frac{1}{4} - \frac{1}{3}$ ($l = \pi d_c$ for $n = 1$). For fuel–oxygen mixtures, the ratio is $\frac{h}{l} = \frac{1}{10} - \frac{1}{5}$ [5]. The difference in the relative width of the detonation front for the fuel–air mixtures is attributed to several causes. These are the absence (or undeveloped nature) of the combustion front from the product side, as well as the supersonic velocity of the mixture ahead of the transverse detonation wave front. The measured axial velocity of the mixture passing through the lower part of the front attains about 600 m s^{-1} and approaches the maximum possible velocity $v_{max} = \left(\frac{2}{\gamma - 1}\right)^{0.5} c_0$, where γ and c_0 are the adiabatic index and sonic velocity for air in the receiver, respectively.

For input pressures of air and acetylene $P_{A0} = 15 \times 10^5$ Pa and $P_{f0} = 10.9 \times 10^5$ Pa, respectively, and for the corresponding flow rates $G_{A0} = 2.12$ kg s^{-1} and $G_{f0} = 0.214$ kg s^{-1}, the basic parameters of the detonation regimes are presented in the table for varied values of the parameter δ and within the range of the current flow rates $G_A = (1.98–1.03)$ kg s^{-1}, $G_f = (0.187–0.1)$ kg s^{-1}, and for $\Phi = 1.26–1.29$.

As is seen from the table, stronger transverse detonation waves (possessing a higher detonation velocity) arise in the case of air inflow to the chamber through the slits with width $\delta = 0.2$ and 0.3 cm. The characteristics of the waves are virtually not violated even for subsonic air inflow. The air supply through narrow ($\delta = 0.1$ cm) and broad ($\delta = 1.0$ cm) slits, apparently, does not ensure a sufficient degree of mixing. The air inflow through the gap of width $\delta = 1.0$ cm is subsonic over the entire dura-

Table

δ, cm	D, km s^{-1}	P_m, 10^5 Pa	P_c, 10^5 Pa	$\frac{P_m}{P_c}$
0.1	1.1–1.27–1.23	6.67–3.4	1.2–1.0	5.66–3.4
0.2	1.48–1.43	3.6–1.82	1.27–1.0	2.83–1.82
0.3	1.35–1.27	2.7–1.34	1.3–1.0	2.03–1.34
1	0.89–0.7 Unstable	1.53–1.12	1.22–1.06	1.25–1.06

Note: P_m corresponds to pressure in the air collector.

tion of the process. The comparison of detonation velocities for this regime and for the regime corresponding to δ = 0.3 cm, for which the subsonic inflow also mainly dominates, directly indicates insufficient mixing of the components in the zone of the rotation of the transverse detonation wave front for δ = 1.0 cm.

The increase in the flow rate of the mixture components with respect to the data presented above proportionally elevated the pressure in the detonation chamber and extended the region of existence of waves of the first structure (Fig. 2a). In this case, the transverse detonation wave velocity, as a rule, also increased; its maximum corresponded to 1.58 km s^{-1}.

Thus, in the case of a separate supply of fuel–air mixture components into a ducted cylindrical combustion chamber, we managed to realize for the first time a controlled regime of continuous spin detonation accompanied by the appearance of transverse detonation waves.

ACKNOWLEDGMENTS

This work was supported by the Russian Foundation for Basic Research, project no. 02-01-00551, and by the Council of the President of the Russian Federation for Support of Young Russian Scientists and Leading Scientific Schools, project no. NSh-2073.2003.1.

REFERENCES

1. Ya. B. Zel'dovich, Zh. Tekh. Fiz. **10** (17), 145 (1940).
2. B. V. Voĭtsekhovskiĭ, Dokl. Akad. Nauk SSSR **129**, 1254 (1959) [Sov. Phys. Dokl. **4**, 1207 (1959)].
3. B. V. Voĭtsekhovskiĭ, V. V. Mitrofanov, and M. E. Topchiyan, *Detonation Wave Structure in Gases* (Izd. Sibirskogo Otd. AN SSSR, Novosibirsk, 1968).
4. F. A. Bykovskiĭ, D. Klopotov, and V. V. Mitrofanov, Dokl. Akad. Nauk SSSR **224**, 1038 (1975) [Sov. Phys. Dokl. **20**, 667 (1975)].
5. F. A. Bykovskiĭ and V. V. Mitrofanov, Fiz. Goren. Vzryva **16** (5), 107 (1980).
6. F. A. Bykovskiĭ and V. V. Mitrofanov, in *Control of Detonation Processes* (Elex-KM Publ., Moscow, 2000), pp. 209–211.
7. S. A. Zhdan, V. V. Mordashev, and V. V. Mitrofanov, Fiz. Goren. Vzryva **26** (2), 91 (1990).
8. F. A. Bykovskiĭ, V. V. Mitrofanov, and E. F. Vedernikov, Fiz. Goren. Vzryva **33** (3), 120 (1997).
9. F. A. Bykovskiĭ, Zh. Nauch. Prikl. Fotogr. Kinematograf., No. 2, 85 (1981).
10. B. V. Voĭtsekhovskiĭ and B. E. Kotov, Izv. Akad. Nauk SSSR, No. 4, 74 (1958).
11. A. A. Vasil'ev, V. V. Mitrofanov, and M. E. Topchiyan, Fiz. Goren. Vzryva **23** (5), 109 (1987).

Translated by G. Merzon

Doklady Physics, Vol. 50, No. 1, 2005, pp. 59–61. Translated from Doklady Akademii Nauk, Vol. 400, No. 3, 2005, pp. 341–343.

MECHANICS

Estimation of the Ultimate Intensity of Pulsed Dynamic Loads in Crack Mechanics

Academician N. F. Morozov*, Yu. V. Petrov, and V. I. Smirnov*****

Received October 14, 2004

As is shown in experiments on dynamic fracture, the defining factor of this process is the incubation time t_{inc} required for preparing a macroscopic break of a material. The conception of the incubation time was proposed in [1, 2], and the corresponding criterion was called there the minimum-time criterion.

In [3], a dynamic criterion of fracture was proposed for which the basic parameter is the structural time τ. Various methods for the interpretation of this characteristic were also presented that depended on the class of problems under consideration. In particular, it was shown that, under the conditions of the experiments in [1, 2], the structural time τ can be interpreted as the incubation time t_{inc}.

In this paper, we offer one more interpretation of the incubation (structural) time τ, which is based on the asymptotic solution to the dynamical problem of a semi-infinite crack in an elastic medium loaded by a wave pulse, whose time shape is the Dirac delta-function $\delta(t)$. This shape of a load is traditionally used in dynamical problems of elasticity theory. In our case, using the structural-time criterion, we can estimate a jump at the displacement-wave front, i.e., answer the question concerning the possibility of violating the integrity of a medium.

Let a semi-infinite crack be located in an unbounded elastic plane. A uniformly distributed load

$$\sigma_y = I\,\delta(t), \quad I = \frac{(\lambda + 2\mu)U}{c_1}, \tag{1}$$

acts at the crack faces ($x \le 0$, $y = \pm 0$). Here, λ and μ are Lamé constants, c_1 is the longitudinal-wave velocity, and U is the load amplitude having the dimension of length. Then, on the continuation of the crack, the asymptotic expression for the maximum tensile stress is valid [4]:

$$\sigma_y = \frac{K_I(t)}{\sqrt{2\pi x}} + O(1), \quad x \longrightarrow 0, y = 0, \tag{2}$$

where $K_I(t)$ is the stress-intensity factor

$$K_I(t) = \frac{I\Phi(c_1, c_2)}{2\sqrt{t}}, \quad \Phi(c_1, c_2) = \frac{4c_2\sqrt{c_1^2 - c_2^2}}{c_1\sqrt{\pi c_1}}, \tag{3}$$

and c_2 is the velocity of transverse waves.

We now estimate the threshold fracturing amplitude I of a force pulse. To this aim, we apply the structural-time criterion of [3] in the form

$$\max_t \int_{t-\tau}^{t} K_I(s)ds \le K_{Is}\tau, \tag{4}$$

where K_{Is} is the static fracture toughness.

We consider the threshold (i.e., minimal) fracturing pulse amplitude I_* as the least value of I for which the equality holds in relationship (4). After substituting the value of the stress-intensity factor $K_I(t)$ from formula (3) into criterial relationship (4), we arrive at the relation

$$I_* = \frac{K_{Is}\tau}{\sqrt{\tau}\Phi(c_1, c_2)}. \tag{5}$$

Criterion (4) makes it also possible to determine the time to fracture t_*. To do this, we do not need to calculate the maximum with respect to time in expression (4), and can take the lower integration limit (within the given problem) to be equal to zero. Upon integration, we arrive at

$$t_* = \left(\frac{K_{Is}\tau}{I\Phi(c_1, c_2)}\right)^2. \tag{6}$$

Next, instead of the product $K_{Is}\tau$, we substitute into Eq. (6) the value of this expression taken from Eq. (5).

St. Petersburg State University,
Bibliotechnaya pl. 2, Staryĭ Petergof, St. Petersburg, 198904 Russia

* *e-mail: bns@hq.math.lgu.spb.ru*

** *e-mail: yp@YP1004.spb.edu*

*** *e-mail: smirnov@VS13866.spb.edu*

1028-3358/05/5001-0059$26.00

Thus, we obtain the ultimate relation between the time to fracture t_* and the incubation time τ:

$$t_* = \left(\frac{I_*}{I}\right)^2 \tau. \quad (7)$$

Thus, in dynamical problems related to cracks, the incubation (structural) time has a simple explanation. Indeed, if the amplitude I of the applied load pulse equals the threshold amplitude I_* characterizing the given material, then the incubation time τ coincides with the time to fracture t_*.

A relationship similar to Eq. (7) can be obtained for an antiplane crack. In this case, the following relations are valid:

$$\sigma_{yz}\Big|_{\substack{y = \pm 0,\\ x \le 0}} = \mu U \delta(c_1 t); \quad (8)$$

$$\sigma_{yz} = \frac{K_0(t)}{\sqrt{2\pi x}} + O(1), \quad x \longrightarrow +0, y = 0, \quad (9)$$

$$K_0(t) = \frac{\sqrt{2}\mu U}{\sqrt{\pi c_1 t}}.$$

Now, the interrelation between the time to fracture t_* and the incubation time τ can be immediately presented in terms of the amplitude U, which has the sense of the displacement jump at the wave front. Performing the same transformations as in the case of a plane crack, we find

$$t_* = \left(\frac{U_*}{U}\right)^2 \tau. \quad (10)$$

Acting in a similar manner, we can show that, if instead of the asymptotic solution to the problem on an antiplane crack, we use the exact solution, then the exponent in equality (10) is equal not to two but to unity.

As was indicated above, the boundary condition for a crack is given in a manner such that the quantity U has the physical sense of the displacement jump at the wave front, namely,

$$w(y, t) = UH(c_1 t + y),$$

where w is the displacement of points of the medium in the corresponding (plane or antiplane) problem and H is the Heaviside step function. In this case, the stress on the crack faces is of form (1) and (8). Thus, it is evident that the numerical estimate of the value of the jump U allows us to answer the question concerning a possible violation of the integrity of the medium at the load-wave front.

Using the other form of criterion (4) proposed in [3], we find the ultimate intensity of the load amplitude U:

$$\max_t \int_{t - d/c_1}^{t} ds \frac{1}{d}\int_0^d \sigma_1(x, s)dx \le \sigma_s. \quad (11)$$

Here, σ_1 is the principal normal stress, σ_s is the static strength of the material, d is the characteristic structural fracture parameter that can be determined in terms of σ_s and the quasi-static value of the critical stress-intensity factor K_{Is}, namely, $d = \frac{2K_{Is}^2}{\pi\sigma_s^2}$. Here, as a particular case, we have taken $\tau = \frac{d}{c_1}$. In the general case, the parameters d and τ should be considered to be independent.

We analyze three possible variants of loading the medium: (i) the load of the form of Eqs. (1), (8) is applied to the crack faces; (ii) an elastic wave of the form of Eqs. (1), (8) propagates inside an uncracked medium; and (iii) a wave of the form of Eqs. (1), (8) impinges onto the crack (the wave front moves in the direction parallel to the plane of the crack location). For the problems under consideration in this study, the stresses σ_y and σ_{yz} are principal. Therefore, the threshold amplitude U_* can be determined by directly integrating the values of σ_y and σ_{yz} over x and t in accordance with Eq. (11). For the first variant of loading, while substituting into Eq. (11), we use the values of σ_y and σ_{yz} from Eqs. (1) and (8). For the second variant, we take them from Eqs. (2) and (9). The solution for the third variant is a superposition of the solutions corresponding to two first variants. The estimates of the threshold amplitude U_* for all three variants of loading are given in Table 1, in which E and ν correspond to the elasticity modulus and Poisson's ratio, respectively.

If we assume that, for a statistical-average material, the relationship $\sigma_s = \frac{E}{2\pi} \approx 0.16E$ is valid [5], then (depending on the Poisson's ratio) the threshold amplitude U_* of the jump, in the general case, can be directly expressed in terms of the structure parameter d. The results for all three variants are presented in Table 2.

As is seen from Table 2, for all methods of loading an antiplane crack, the ultimate amplitude of the displacement jump U_* at the wave front is always lower than the structural element d. In accordance with the structure–time approach to the fracture process, we assume that, at the given scale level, this process proceeds discretely and involves elementary cells with the side sizes multiples of the quantity d. Thus, we consider that, in the problem concerning an antiplane crack, the integrity of the medium is not violated at the wave front. Here, from the standpoint of the material strength, the most unfavorable loading variant is the

Table 1

Variant number	Case under consideration	Threshold jump amplitude U_*	
		plane crack	antiplane crack
1	A load is applied to the crack face	$\frac{\pi(1+\nu)\sigma_s d}{2E\sqrt{2(1-2\nu)}}$	$\frac{\pi(1+\nu)\sigma_s d}{E}$
2	A wave propagates in an uncracked medium	$\frac{(1+\nu)(1-2\nu)\sigma_s d}{(1-\nu)E}$	$\frac{2(1+\nu)\sigma_s d}{E}$
3	Diffraction on a crack (the wave front is parallel to the crack)	$\frac{\pi(1+\nu)(1-2\nu)\sigma_s d}{E[\pi(1-\nu)+\sqrt{2(1-2\nu)}]}$	$\frac{\pi}{\pi+2}\frac{2(1+\nu)\sigma_s d}{E}$

Table 2

Variant number	Case under consideration	Threshold jump amplitude U_*	
		plane crack	antiplane crack
1	A load is applied to the crack face	$(0.18-\infty)d$	$(0.50–0.75)d$
2	A wave propagates in an uncracked medium	$(0.16-0)d$	$(0.32–0.48)d$
3	Diffraction on a crack (the wave front is parallel to a crack)	$(0.11-0)d$	$(0.20–0.29)d$

Note: The lower and upper limits correspond to the minimum ($\nu = 0$) and maximum ($\nu = 0.5$) values of Poisson's ratio, respectively.

third one, since in this case, the threshold amplitude is the least.

For a plane crack, the principal difference is observed only for the first variant, when a load is applied to crack faces in a medium consisting of an incompressible material ($\nu = 0.5$). However, as was shown in [6], the asymptotic solution is inapplicable to these materials.

REFERENCES

1. J. F. Kalthoff and D. A. Shokcley, J. Appl. Phys. **48**, 986 (1977).
2. D. A. Shokcley, D. C. Erlich, J. F. Kalthoff, *et al.*, Eng. Fract. Mech. **23**, 311 (1986).
3. N. F. Morozov and Yu. V. Petrov, *Problems of Fracture Dynamics for Solids* (St. Petersburg Univ., St. Petersburg, 1997) [in Russian].
4. G. P. Cherepanov and L. V. Ershov, *Fracture Mechanics* (Mashinostr., Moscow, 1977) [in Russian].
5. N. F. Morozov, *Mathematical Problems of Crack Theory* (Nauka, Moscow, 1984) [in Russian].
6. Yu. V. Petrov and A. A. Utkin, *Asymptotic Behavior of Stresses at Crack Tips in Dynamical Problems of Elasticity Theory. Textbook* (Inst. Machine Science, RAS, St. Petersburg, 2001) [in Russian].

Translated by G. Merzon

Doklady Physics, Vol. 50, No. 1, 2005, pp. 7–11. Translated from Doklady Akademii Nauk, Vol. 400, No. 2, 2005, pp. 181–185.

PHYSICS

Study of Microstrip Models of Bandpass Filters Based on 1D Photonic Crystals

B. A. Belyaev*, A. S. Voloshin, and Academician V. F. Shabanov***

Received August 24, 2004

It is well known that, when electromagnetic oscillations propagate in waveguide structures that include alternating sections of lines with different characteristic impedance but with the same electric length, transparency windows (frequency bands where the damping of passed waves is minimal) are observed, and they are separated by bands of almost total reflection (stopbands) [1]. Such irregular structures are used to design UHF devices. In particular, these structures are utilized as a basis for constructing characteristic impedance transformers, phase shifters, and bandpass filters. The effect of the almost complete reflection of electromagnetic waves from periodic structures is used not only in the UHF band but also in optics for creating high-quality mirrors. The simplest mirror is a multilayer thin-film system of alternating dielectric layers with different refraction indices. In this case, the thickness of each layer in the structure is close to a quarter of the wavelength at the central frequency of the reflection band [2]. The film coatings of alternating dielectric layers with a thickness close to half the wavelength serve as bandpass filters, which are used, e.g., in switching devices of fiber optic communication lines [3]. In this case, a coating is a system of coupled half-wavelength resonators.

The current status of micro- and nanotechnologies, including graphoepitaxy [4], provides the production of not only 1D but also 2D and 3D structures, where the characteristic sizes of periodic irregularities are about the light wavelength. Such structures, called photonic crystals, also have transparency windows and gaps in the optical range of electromagnetic waves [5]. Owing to their unique properties and the possibility of effectively controlling the light propagation in photonic crystals, they are promising for developing various optoelectronic devices. However, the production of even 1D photonic crystals (multilayer structures including superlattices) is an expensive process requiring unique equipment. At the stage of development of a device based on photonic crystals, the process of optimizing the design can be significantly cheapened by replacing it with a bulk (nonfilm) analog operating in the UHF band. The most successful analog of a dielectric superlattice is a microstrip structure [6, 7] that is technologically simple. Moreover, it is closer to an actual layered structure than waveguide analogies, because the basic oscillation modes propagating in microstrip transmission lines are quasi-T-waves whose microwave-field structure is close to the structure of transverse waves propagating in superlattices.

The principle of designing microstrip models of 1D photonic crystals consisting of dielectric layers with different refractive indices is based on the strong dependence of the effective dielectric constant ε_{eff} of a microstrip transmission line on the strip-conductor width w and substrate thickness h. The propagation velocity and, correspondingly, the electromagnetic wavelength in the line are determined by ε_{eff}, which can be expressed in terms of the relative dielectric constant ε of the substrate and basic constructive parameters of the line [8] as

$$\varepsilon_{eff} = \frac{\varepsilon + 1}{2} + \frac{\varepsilon - 1}{2} P, \quad (1)$$

where

$$P = \begin{cases} \dfrac{1}{\sqrt{1 + \dfrac{12h}{w}}} & \text{for} \quad w \geq h, \\ \dfrac{1}{\sqrt{1 + \dfrac{12h}{w}}} + 0.04\left(1 - \dfrac{w}{h}\right)^2 & \text{for} \quad w \leq h. \end{cases}$$

It is worth noting that formula (1) is valid for the strip conductor of zero thickness and only in the quasi-static frequency band when the transverse sizes w and h of the microstrip line are much smaller than the wavelength of the electromagnetic wave propagating in it. According to formula (1), a decrease in w at a fixed substrate thick-

Kirenskiĭ Institute of Physics, Siberian Division, Russian Academy of Sciences, Akademgorodok, Krasnoyarsk, 660036 Russia

** e-mail: belyaev@iph.krasn.ru*

*** e-mail: alex_vlshn@main.krasn.ru*

1028-3358/05/5001-0007$26.00

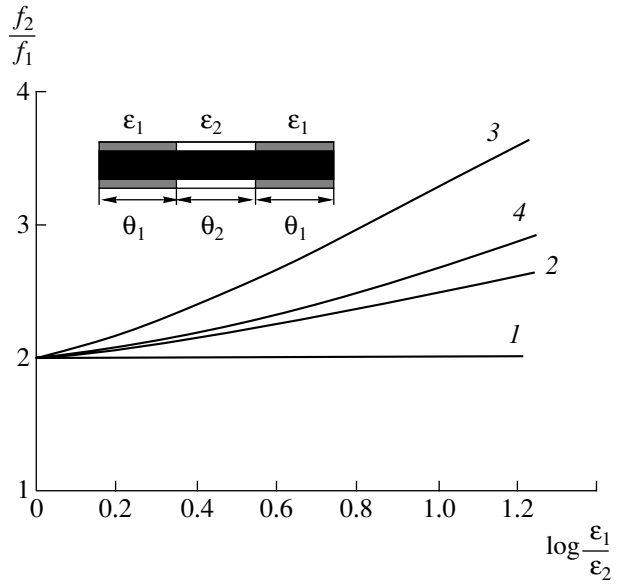

Fig. 1. Relative frequency of the second resonance of the microstrip structure vs. the ratio of the dielectric constants of the outer and middle sections of its hybrid substrate for q = (*1*) 0, (*2*) 0.1, (*3*) 0.33, and (*4*) 0.66.

ness leads to a monotonic decrease in the effective dielectric constant. Therefore, segments of regular microstrip lines that differ in their conductor widths can serve as a good UHF model of dielectric layers differing in refraction index in the multilayer structure [6, 7].

Studies of UHF models of devices based on photonic crystals make it possible not only to cheapen the development stage but also to considerably shorten the development time, as well as to obtain important recommendations for achieving the extreme characteristics of the construction under investigation. In particular, microstrip simulation [7] shows that a number of conditions are necessary for manufacturing a high-quality bandpass filter based on the superlattice. First, the necessary jump must be ensured between the characteristic impedances of outer layers of the superlattice and the characteristic impedances of the input and output, which is determined by a given passband of the device. Second, it is necessary to select the dielectric constants of the layers of the superlattice such that couplings between them are in balance, which must also correspond to the given passband of the filter. Third, the electric lengths of resonator layers should be selected such that their natural frequencies coincide with the central frequency of the passband.

We note that, in the microstrip models of superlattice-based filters [7], the central frequencies of all passbands are equidistant and the stopbands between them are much narrower than an octave. This property is caused by the fact that a regular half-wave microstrip resonator, as well as any dielectric layer in the superlattice, has the equidistant spectrum of natural frequencies. However, filters with wide stopbands are often required; i.e., the nearest spurious passband should be spaced by more than an octave. This problem is solved in this work, where we analyze constructions of microstrip models of filters based on 1D photonic crystals that have a nonequidistant spectrum of natural frequencies.

It is known that jumps in the width of the strip conductor or other irregularities in a microstrip resonator make its natural-frequency spectrum nonequidistant. Owing to this property, the frequencies of the first and second resonances of the microstrip resonator can be approached and removed from each other [9]. A similar approach can be used to design bandpass filters based on 1D photonic crystals in order to expand the high-frequency stopband of the device. To this end, it is necessary to create the corresponding jump of the characteristic impedance in the middle of each layer resonator. This jump can be obviously obtained using materials with different dielectric constants ε. In other words, each resonator in a filter of such a construction must consist of three alternating dielectric layers.

Figure 1 shows the microstrip model of the resonator and the ratio $\frac{f_2}{f_1}$ of the frequencies of its first two resonances as a function of the dielectric constant jump of the composite substrate, for which $\varepsilon_1 = 16$ and ε_2 varies from 16 to 1. The calculation was performed in the quasi-static approximation using the 1D model of the resonator [9]. The lines are plotted for several ratios $q = \frac{\theta_2}{2\theta_1 + \theta_2}$ of the electric length of the middle section to the total electric length. Investigations show that the difference between the frequencies f_1 and f_2 increases with the difference between the dielectric constants of the sections. However, for any ratio $\frac{\varepsilon_1}{\varepsilon_2}$, the increase in the second-resonance frequency with respect to the first-resonance frequency is maximal when the electric lengths of all three sections of the microstrip resonator are equal to each other. Thus, for a certain jump in the characteristic impedances of the regular sections of microstrip lines composing the irregular microstrip resonator, the frequencies of the first and second modes can be shifted by almost two octaves. Moreover, the resonance frequencies of almost any oscillation modes in such irregular resonators can be purposely changed by varying the number, positions, and values of jumps [10].

Figure 2 shows several models of microstrip constructions of bandpass filters based on 1D photonic crystals and their schemes. Their frequency responses calculated numerically in the quasi-static approximation are given in the same figure. For simplicity, each device contains only three resonators. They are tuned so that the central frequency of the first passband is equal to $f_0 = 3$ GHz, the relative width of this band as mea-

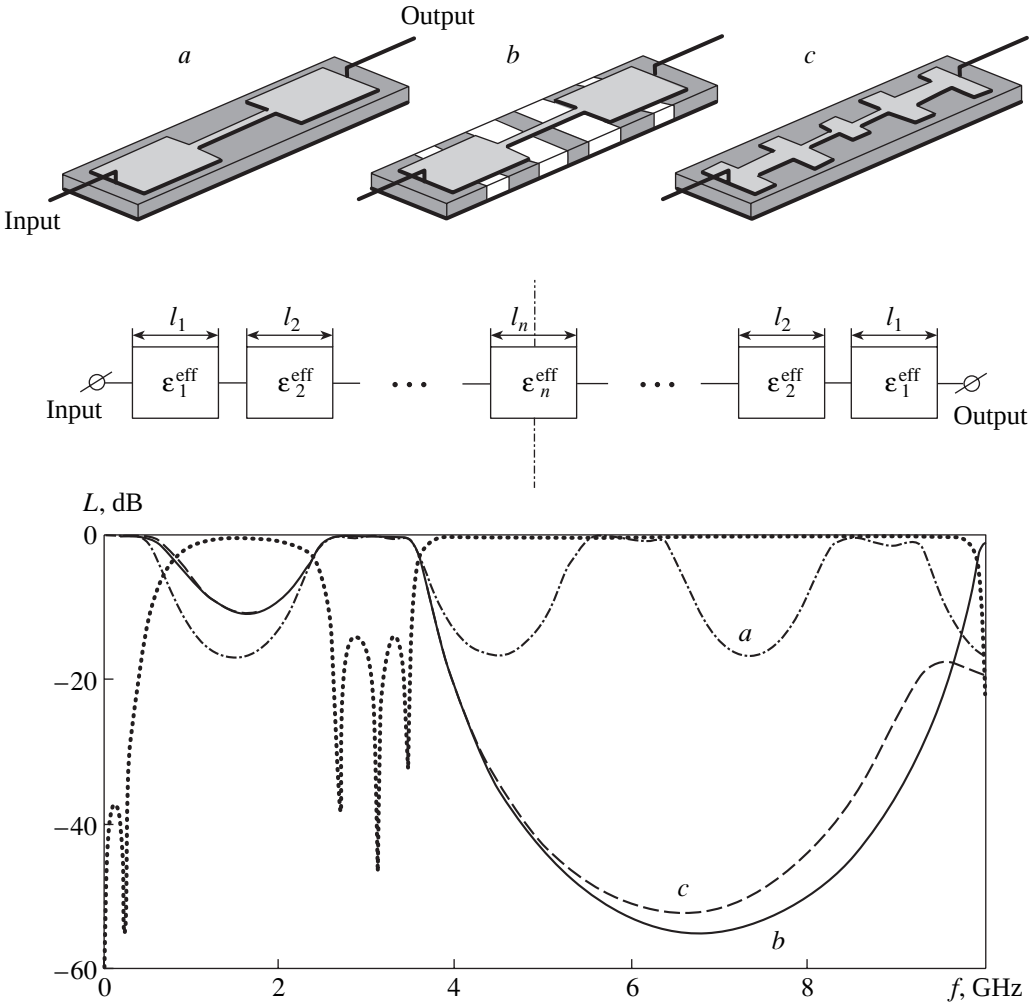

Fig. 2. Microstrip constructions of bandpass filters under investigation and their frequency responses. The dotted line is the frequency dependence of inverse losses for construction *b.*

sured at a level of –3 dB from the maximum-loss level is equal to $\frac{\Delta f_3}{f_0}$ = 40%, and the maxima of inverse losses in the passband are equal to –14 dB. Model *a* corresponds to a usual three-layer structure, where the layer with a low refraction index is sandwiched between two identical layers with a high refraction index [6, 7]. For this reason, the frequency response of this model involves equidistantly alternating passbands and stopbands. The filter is manufactured on a 1-mm-thick substrate with ε = 16. Note that the antinodes of the microwave electric field *E* and microwave magnetic field *H* are at the edges and centers of the outer resonators, respectively. In contrast, for the middle resonator, the antinodes of *H* and *E* are at the edges and center, respectively.

In model *b* shown in Fig. 2, all three resonators are irregular, because they are manufactured on composite substrates. In this case, the dielectric constant of the substrates is high (ε = 16) and low (ε = 1) in the antinodes of the electric and magnetic fields, respectively. As should be expected for such a construction, the microwave stopband is expanded by several times due to an increase in the frequency of the second (spurious) passband. Moreover, the stop level in the stopband increases significantly due to an increase in reflection losses. This means that this comparatively simple construction of the 1D photonic crystal can simultaneously serve as both a bandpass filter with an increased stopband and a good mirror with the reflection index close to unity in a wide frequency band. Note that the necessary jumps of the characteristic impedance in the irregular resonators of the microstrip model can be ensured by a stepwise change in the strip-conductor width for the structure manufactured on a common substrate (see Fig. 2, model *c*). In this case, however, the jump of the effective dielectric constants in wide and narrow sections of the microstrip structure is lower than that on a composite substrate. For this reason, the width of the stopband, as well as the stop level in it, decreases.

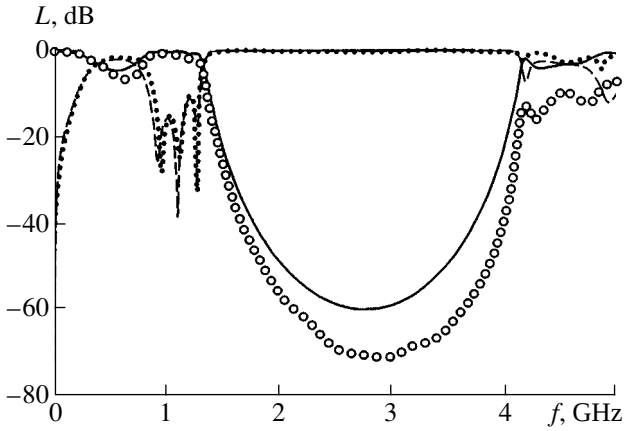

Fig. 3. Frequency dependences of inversion and return losses in the filter of construction *b* in Fig. 2. Lines are calculations and points are experimental data.

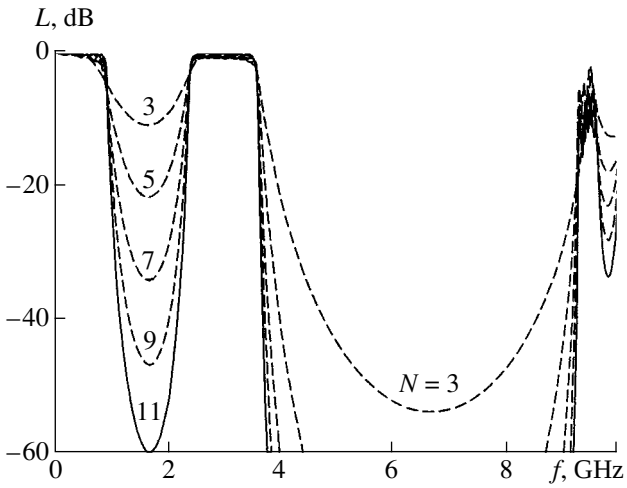

Fig. 4. Frequency responses for the various numbers of resonators in the microstrip model of the bandpass filter based on a 1D photonic crystal.

An experimental test of several microstrip constructions of filters manufactured by engraving a lacquer [11] showed good agreement with the numerical calculations. As an example, Fig. 3 shows (points) measurements of inversion and return losses for the filter of model *b* in comparison with (lines) the corresponding calculations. The hybrid substrate of the filter consisted of TBNS ceramic plates ($\varepsilon = 80$) and flan ($\varepsilon = 2.8$) with a thickness of 2 mm. The topological sizes of the conductors of the device were previously obtained by parametrically synthesizing the filter with a central frequency of $f_0 = 1$ GHz and a relative passband width of $\frac{\Delta f_3}{f_0} = 60\%$. However, the experiment was compared with theoretical calculations using the actual constructive parameters of the microstrip structure that were measured after its manufacture.

The parametric synthesis of the filter model based on the 1D photonic crystal, as well as the tuning of any multilink bandpass filter, requires the satisfaction of three conditions. First, the necessary coupling must be ensured between the outer resonators and the input and output transmission lines in accordance with a given passband of the device. Second, it is necessary to ensure balance between the couplings of all resonators (three in the case under consideration) with each other. Third, the resonance frequencies of the resonators must coincide with the central frequency of the passband. The coupling between the adjacent resonators is undoubtedly determined primarily by the difference between the characteristic impedances of the regular segments of the lines at the junction between the resonators. In the quasi-static frequency band, these characteristic impedances are calculated by the formulas [8]

$$Z = \begin{cases} \dfrac{120\pi(\varepsilon_{\text{eff}})^{-1/2}}{1.393 + \dfrac{w}{h} + 0.667\ln\left(\dfrac{w}{h} + 1.444\right)} & \text{for } w \geq h, \\ \dfrac{60}{\sqrt{\varepsilon_{\text{eff}}}}\ln\left(\dfrac{8h}{w} + \dfrac{w}{4h}\right) & \text{for } w \leq h. \end{cases} \quad (2)$$

The coupling between the outer resonators with the external tract is determined by the difference between the characteristic impedances of the input transmission lines, $Z_0 = 50\ \Omega$, and the corresponding segments of microstrip lines, which form the edge sections of the outer resonators in the model under consideration.

Investigations show that, with an increase in the number of irregular resonators in the microstrip model of the photonic-crystal-based filter, the gain slope increases and damping in the stopbands increases almost exponentially. This is corroborated in Fig. 4, where the frequency responses are shown for the filters containing 3–11 resonators on hybrid substrates (Fig. 2, model *b*). The passband of the filters is $\frac{\Delta f_3}{f_0} = 40\%$, and the hybrid substrates consist of two materials with dielectric constants $\varepsilon_1 = 16$ and $\varepsilon_2 = 1$. It is seen that each addition of two resonators to the construction under consideration is accompanied by an increase in damping in the low-frequency and high-frequency stopbands by more than 10 and 20 dB, respectively. We emphasize that damping in the stopband increases significantly with the narrowing of the passband of the device.

It is worth noting that the coupling between resonators in the microstrip structure is determined not only by jumps in the characteristic impedances but also by the loaded *Q* factor on which the amplitudes of microwave fields in microstrip resonator depend. As is known, this *Q* factor is higher for the inner resonators. As a result, to ensure the given coupling between inner

Parameters of microstrip segments for an 11-resonator filter with a relative passband width of 40%

Microstrip resonator no.	w, mm	l_1, mm	l_2, mm
1 (11)	3.36	2.86	9.92
2 (10)	0.28	11.63	3.75
3 (9)	4.11	3.11	10.92
4 (8)	0.18	11.53	3.76
5 (7)	4.40	3.08	11.51
6	0.16	11.51	3.76

resonators, the jump between the characteristic impedances of the outer sections of the corresponding regular segments of the lines must be larger than that for the outer resonators. This relation is illustrated by the constructive parameters presented in the table for 11-resonator filters whose frequency response is shown in Fig. 4.

Thus, we have proposed a construction of bandpass filters based on 1D photonic crystals, where each resonator consists of three alternating layers with different dielectric constants, which ensures a significant broadening of the high-frequency stopband. Good agreement between the quasi-static numerical analysis of microstrip models of such filters with the corresponding experiments enables one to obtain the constructive parameters of a device with given characteristics. Analysis shows that this construction, even with a few layers, can serve as not only a good bandpass filter but also as a good mirror with a high reflection index in a wide frequency band.

REFERENCES

1. G. Matthaei, L. Young, and M. T. Jones, *Microwave Filters, Impedance Matching Networks and Coupling Structures* (McGraw-Hill, New York, 1964; Svyaz', Moscow, 1971).
2. H. A. Macleod, *Thin-Film Optical Filters* (Adam Hilger, London, 1969).
3. M. Shirasaki, H. Nakajima, T. Obokata, and K. Asama, Appl. Opt. **21**, 4229 (1982).
4. E. A. Goodilin, E. S. Reddy, J. G. Noudem, *et al.*, J. Cryst. Growth **241**, 512 (2002).
5. E. Yablonovitch, Phys. Rev. Lett. **58**, 2059 (1987).
6. H. Kitahara, T. Kawaguchi, J. Miyashita, and T. W. Takeda, J. Phys. Soc. Jpn. **72** (4), 951 (2003).
7. B. A. Belyaev, A. S. Voloshin, and V. F. Shabanov, Dokl. Akad. Nauk **395** (6), 756 (2004).
8. V. I. Gvozdev and E. I. Nefedov, *3D Microwave Integrated Circuits* (Nauka, Moscow, 1985) [in Russian].
9. B. A. Belyaev, V. V. Tyurnev, and Yu. G. Shikhov, Élektron. Tekh. Ser. 1: SVCh Tekh. **2** (270), 20 (1997).
10. B. A. Belyaev, V. V. Tyurnev, V. A. Vasil'ev, and G. M. Ragzin, Preprint No. 448F, IF AN SSSR (Inst. of Physics, USSR Academy of Sciences, 1987).
11. B. A. Belyaev, A. V. Kazakov, A. A. Leksikov, and I. Ya. Makievskiĭ, Prib. Tekh. Éksp., No. 1, 167 (1998).

Translated by R. Tyapaev